

RETRIEVAL OF AEROSOL MICROPHYSICAL PROPERTIES FROM THE AERONET  
PHOTO-POLARIMETRIC MEASUREMENTS

by

Xiaoguang Xu

A DISSERTATION

Presented to the Faculty of  
The Graduate College at the University of Nebraska

In Partial Fulfilment of Requirements

For the Degree of Doctor of Philosophy

Major: Earth & Atmospheric Sciences  
(Meteorology/Climatology)

Under the Supervision of Professor Jun Wang

Lincoln, Nebraska

August, 2015

# RETRIEVAL OF AEROSOL MICROPHYSICAL PROPERTIES FROM THE AERONET PHOTO-POLARIMETRIC MEASUREMENTS

Xiaoguang Xu, Ph.D.

University of Nebraska, 2015

Adviser: Jun Wang

Atmospheric aerosols play an important role in earth climate change by scattering and absorbing solar and terrestrial radiation, and indirectly through altering the cloud formation, lifetime, and radiative properties. However, accurate quantification of these effects is in no small part hindered by our limited knowledge about the particle size distribution and refractive index, the aerosol microphysical properties essentially pertain to aerosol optical and cloud-forming properties. The focus of this thesis is the characterization of aerosol microphysical properties from ground-based polarimetric remote sensing.

The central research goal is to obtain accurate aerosol PSD and refractive index of both fine and coarse modes from the multi-spectral and multi-angular direct and diffuse solar radiation measured by the SunPhotometer of Aerosol Robotic Network (AERONET). We do so by (1) developing an inversion algorithm for the retrieval of aerosol refractive indices and particle size distribution from a combined use of direct and diffuse solar radiation measurements from AERONET, (2) conducting a sensitivity study and error budgeting exercise to examine the potential of adding polarization to the radiance-only inversion, and (3) performing ground-based retrievals using available AERONET polarimetric measurements.

The results from theoretical information and error analysis show a remarkable increase in information by adding additional polarization and/or radiances into the inversion: an overall increase of 2—5 of DFS comparing with radiance-only measurements. Correspondingly, smallest retrieval errors are found in the added-polarization scenario: 2.3% (2.9%) for the

fine-mode (coarse-mode) aerosol volume concentration, 1.3% (3.5%) for the effective radius, 7.2% (12%) for the effective variance, 0.005 (0.035) for the real part refractive index, and 0.019 (0.068) for the single scattering albedo. These errors represent a reduction from their counterparts in the radiance-only scenario of 79% (57%), 76% (49%), 69% (52%), 66% (46%), and 49% (20%), respectively. In real cases, we found that our retrievals are overall consistent with AERONET operational inversions, but can offer mode-resolved refractive index and SSA with acceptable accuracy for the aerosol composed by spherical particles. Along with the retrieval using both radiance and polarization, we also performed radiance-only retrieval to demonstrate the improvements by adding polarization in the inversion. Contrast analysis indicates that with polarization, retrieval error can be reduced by over 50% in PSD parameters, 10–30% in the refractive index, and 10–40% in SSA.

## **DEDICATION**

To the memory of my grandfather

**Zhaoxiang Xu**

(1933 - 2014)

## **ACKNOWLEDGMENTS**

Acknowledgment to be filled ...

## **GRANT INFORMATION**

The NASA Earth and Space Science Fellowship funded this project from September 2012 to August 2015. I am also grateful to the support from NASA's New Investigator Program and Radiation Science Program (to Dr. Jun Wang).

# Table of Contents

<b>Dedication</b>	<b>iv</b>
<b>Acknowledgments</b>	<b>v</b>
<b>Grant Information</b>	<b>vi</b>
<b>List of Figures</b>	<b>x</b>
<b>List of Tables</b>	<b>xiv</b>
<b>1 Introduction</b>	<b>1</b>
1.1 Background and Motivation . . . . .	1
1.1.1 Previous studies on aerosol microphysical retrievals . . . . .	2
1.1.2 The AERONET measurements . . . . .	3
1.1.3 Challenges and opportunities . . . . .	6
1.2 Research Goals and Thesis Outline . . . . .	10
<b>2 Model Developments</b>	<b>12</b>
2.1 Introduction . . . . .	12
2.2 The UNL-VRTM . . . . .	14
2.2.1 Molecular scattering and absorption . . . . .	16

2.2.2	Aerosol single scattering . . . . .	18
2.2.3	Surface representations . . . . .	20
2.2.4	Radiative transfer . . . . .	21
2.2.5	Capability of calculating Jacobians . . . . .	22
2.3	Model Benchmarking and Verifications . . . . .	26
<b>3</b>	<b>Inversion Theories and Algorithm</b>	<b>33</b>
3.1	Introduction . . . . .	33
3.2	Inversion Theories . . . . .	34
3.2.1	Maximum a posteriori solution of an inverse problem . . . . .	34
3.2.2	Information theory . . . . .	37
3.3	New Research Algorithm for AERONET Inversion . . . . .	39
3.3.1	Definition of state vector and observation vector . . . . .	41
3.3.2	Combine a priori and smoothness constraints . . . . .	42
3.3.3	Statistical optimized inversion . . . . .	45
3.3.4	Characterizing retrieval error . . . . .	47
3.3.5	Quality control of measurements . . . . .	48
<b>4</b>	<b>Information Content Analysis</b>	<b>50</b>
4.1	Introduction . . . . .	50
4.2	Experimental Design . . . . .	52
4.2.1	<i>a priori</i> characteristics . . . . .	52
4.2.2	Synthetic observations . . . . .	53
4.3	Results . . . . .	55
4.3.1	Error-normalized (EN) Jacobian matrix . . . . .	55
4.3.2	Information content and retrieval error . . . . .	60
4.3.2.1	Aerosol PSD . . . . .	62



4.3.2.2	Refractive indices . . . . .	64
4.3.2.3	Single scattering albedo . . . . .	67
4.4	Sensitivity of Retrieval Error to AOD and $fmf_v$ . . . . .	68
4.5	Summary . . . . .	74
<b>5</b>	<b>Case Demonstrations</b>	<b>77</b>
5.1	Introduction . . . . .	77
5.2	Selected Cases and the <i>a priori</i> Characterization . . . . .	77
5.3	Fitting Residuals . . . . .	80
5.4	Retrieved Aerosol Properties . . . . .	82
5.5	Improvement over Radiance-Only Retrievals . . . . .	86
5.6	Summary . . . . .	88
<b>6</b>	<b>Conclusions and Outlook</b>	<b>90</b>
6.1	Conclusions . . . . .	90
6.1.1	UNL-VRM and new AERONET inversion algorithm . . . . .	91
6.1.2	Potential information contained in AERONET polarization . . . . .	92
6.1.3	Application to real retrieval . . . . .	93
6.2	Outlook and Future Work . . . . .	93
<b>A</b>	<b>Abbreviations and Acronyms</b>	<b>95</b>
<b>B</b>	<b>Symbols</b>	<b>96</b>
<b>C</b>	<b>Derivations of Transformation Vector <math>\Pi</math></b>	<b>97</b>
<b>D</b>	<b>List of Publications Generated During PhD Study</b>	<b>103</b>
	<b>References</b>	<b>104</b>

# List of Figures

1.1	A photo of the CIMEL CE318 type SunPhotometer (a) and its observational modes: (b) direct-sun radiance scan, (b) sky-radiance scan on the solar almucantar, (c) solar principal-plane scan for sky radiance and polarization. Detail scan information are presented in Table 1.1 and text. . . . .	4
2.1	Flowchart of the UNL-VRM components. See text for detail. . . . .	15
2.2	Some benchmark simulations by the UNL-VRM: (a) Downward solar spectral irradiance at the TOA and the surface for solar zenith angle of $30^\circ$ . (b) Total-atmosphere gas absorption optical depth in the range $0.2\text{--}0.8\ \mu\text{m}$ . (c) Same as (b) but for $0.8\text{--}4\ \mu\text{m}$ . (d) Optical depth of $\text{SO}_2$ and $\text{NO}_2$ in polluted cases. Also shown in (b) and (c) are the optical depth computed from Santa Barbara DISORT Atmospheric Radiative Transfer (SBDART) model [Ricchiazzi <i>et al.</i> , 1998]. The mid-latitude summer atmospheric profile is assumed [McClatchey <i>et al.</i> , 1972]. (Figure adopted from Wang <i>et al.</i> [2014].) . . . . .	27
2.3	Degree of linear polarization ( $-Q/I$ ) of downward radiation for a pure Rayleigh atmosphere: (a) computed by UNL-VRM for the case analyzed in Figure 5.7 of Coulson [1988] and shown here as (b). (c)–(e) shows the comparisons of $I$ , $Q$ , and $U$ computed by Coulson <i>et al.</i> [1960] and those from UNL-VRM. In (a) and (b), $A_s$ represents the surface albedo value. In (c) and (d), the calculation is for $\tau = 1.0$ , surface albedo is 0.25, $\cos \theta_0 = 0.8$ , and for 8 different viewing angles. (Figure adopted from Wang <i>et al.</i> [2014].) . . . . .	28

2.4	Counterparts in Tables 3–10 of <i>Garcia and Siewert</i> [1989] for upwelling radiation on the top of the same atmospheric conditions of aerosol scattering. No gas absorption and Rayleigh scattering are considered. Note that compared here are $I$ and $Q$ values reported in <i>Garcia and Siewert</i> [1989] for 9 view angles (with cosine values from 0.1 to 0.9 at equal spacing of 0.1) and 3 relative azimuth angles ( $0$ , $\pi/2$ , and $\pi$ ), which yields a total of 27 data points. For $U$ and $V$ , their values are reported for the same 9 viewing angles but for one relative azimuth angle ( $\pi/2$ ) only. The calculation is performed at wavelength of 951 nm and $\tau$ of 1.0, and aerosol size distribution parameters $r_{\text{eff}} = 0.2$ , $v_{\text{eff}} = 0.07$ , refractive index $m_r = 1.44$ , and SSA of 0.99. (Figure adopted from <i>Wang et al.</i> [2014].)	29
2.5	Intercomparison of Jacobians ( $\partial \xi / \partial \ln x$ ) calculated with UNL-VRTM using the analytical method (y-axis) with those computed from UNL-VRTM using finite-difference estimates (x-axis). Here $\xi$ is one of the Stokes parameters: $I$ (top row), $Q$ (middle row), and $U$ (last row). $x$ is one of 7 parameters associated with fine-mode aerosols: mass concentration $m_A$ , $\tau_A$ , $m_r$ , $m_i$ , $r_g$ and $\sigma_g$ (of the lognormal PSD), and height ( $H$ ) of peak aerosol concentration in the vertical. Note, the calculation is done for an atmosphere containing both fine- and coarse-mode aerosols as described in <i>Hess et al.</i> [1998]. (Figure adopted from <i>Wang et al.</i> [2014].)	31
2.6	Same as in Fig. 5, but for coarse mode aerosols. (Figure adopted from <i>Wang et al.</i> [2014])	32
3.1	The concept of an inverse problem that optimizing an estimates from observations. (Courtesy: Daniel Jacobs)	35
3.2	General structure of the new research inversion algorithm for the retrieval of aerosol microphysical parameters from AERONET photo-polarimetric measurements.	41
4.1	Volume size distribution for the aerosol types adopted for the information analysis. Relevant aerosol parameters are summarized in the Tables 4.1 and 4.2.	53
4.2	(a) Simulated radiances in the solar almucantar plane as a function of azimuth angle. (b) Simulated degree of linear polarization (DOLP) in the solar principal plane as a function of view zenith angle. Simulations are for the well-mixed aerosol type with columnar AOD of 1.0 at 440 nm as shown in the Table 4.2. Solar zenith angle is $55^\circ$ and top abscissas show corresponding scattering angles.	56

4.3	Error-normalized Jacobians of almucantar radiances $I_{\text{alm}}$ (left column) and degree of linear polarization $\text{DOLP}_{\text{pp}}$ (right column) with respect to retrieved aerosol parameters in the <i>fine</i> mode: (a, f) $V_0$ , (b, g) $r_{\text{eff}}$ , (c, h) $v_{\text{eff}}$ , (d, i) $m_r$ , and (e, j) $m_i$ . Simulations use type-II aerosols with columnar AOD of 1.0 at 440 nm and solar zenith angle of $55^\circ$ . The top and bottom abscissas are respectively the scattering angle and SunPhotometer scanning geometries. . . . .	57
4.4	Same as Figure 4.3 but for parameters of aerosol in the <i>coarse</i> mode. . . . .	58
4.5	Degree of freedom for signal (DFS) as a function of solar zenith angle for retrieving all 22 parameters when using aerosol type of (a) fine-dominated, (b) well-mixed, and (c) coarse-dominated. Four differently colored-curves denote four observation scenarios defined in Table 1. Panel (d) shows the maximum scattering angles that can be reached by the almucantar and the principal-plane scans. . . . .	61
4.6	DFS components (left column) and retrieval uncertainty (right column) as a function solar zenith angle with different observation scenarios defined in Table 4.3. Quantities are averages for three aerosol types defined in Table 4.2, and error bars represent one fifth of standard deviation. Three rows from top to bottom are respectively for retrieving $V_0$ , $r_{\text{eff}}$ , and $v_{\text{eff}}$ . In each panel, shown in the left is for the fine mode and in the right is for the coarse mode. . . . .	63
4.7	Same as Figure 4.6 but for DFS components (a-b) and retrieval uncertainty (c-d) for retrieving real part refractive index $m_{\text{real}}$ in four wavelength bands. (a) and (c) are for the fine aerosol mode, while (b) and (d) for the coarse mode. . . . .	65
4.8	Same as Figure 4.7 but for retrieving imaginary part refractive index $m_i$ . . . . .	66
4.9	Contours of DFS as a function of $\text{fmf}_v$ and AOD in scenarios I1 (a) and P1 (b). (c) the difference of DFS between (a) and (b). Simulations are for solar zenith angle of $55^\circ$ . The top abscissa denotes Ångström exponent (AE). . . . .	69
4.10	Retrieval uncertainties as a function of $\text{fmf}_v$ (or AE) and AOD for each individual aerosol parameters in the <i>fine</i> mode: (a) $V_0$ , (b) $r_{\text{eff}}$ , (c) $v_{\text{eff}}$ , (d) $m_r$ , (e) $m_i$ , and (f) $\omega_A$ . Two sub-panels in each panel indicate observations in the scenarios I1 and P1, respectively. Simulations are for solar zenith angle of $55^\circ$ . The x- and y-axis are identical to those in Figure 4.9. Relative uncertainties are shown for $V_0$ , $r_{\text{eff}}$ and $v_{\text{eff}}$ , while absolute errors for $m_r$ , $m_i$ , and $\omega_A$ . Retrieval errors for $m_r$ , $m_i$ , and $\omega_A$ are averaged values over the four spectral bands. . . . .	70
4.11	Same as Figure 4.10, but for aerosol parameters in the <i>coarse</i> mode. . . . .	71

5.1	Climatology of aerosol properties over the Beijing_RADI site derived from AERONET daily inversion products during 2011–2013. The variables are shown as functions of the fine-mode-fraction in terms of the aerosol volume, or $\text{fmf}_v$ . Eight bins are applied for $\text{fmf}_v$ from 0 to 0.8 with an increment of 0.1. The six panels are: (a) Histogram of used data; (b) the Ångström exponents (AE) derived from from 870 to 1020 nm (red) and from 440 to 870 nm (green) wavelength pairs; (c) the effective radius for aerosols in the fine (red) and coarse (green) mode; (d) the effective variance in the fine (red) and coarse (green) mode (green); (e) the real part of the refractive index at 440, 675, 870, and 1020 nm; and (f) the imaginary part of the refractive index and aerosol SSA at the same wavelengths. . . . .	79
5.2	a) Measured almucantar normalized radiances. (b) Measured DOLP in the solar principal plane. (c) Fitting residuals for almucantar radiances by the P-type inversion (solid curves) and I-type inversion (crosses). (d) Same as panel (c), but for fitting the residuals of principal-plane DOLP. Four colors indicate different wavelengths: blue for 440 nm, green for 675 nm, red for 870 nm, and orange for 1020 nm. Gray areas in panels c–d indicate the measurement uncertainty. . . . .	81
5.3	Retrieved aerosol volume size distribution (PSD) and refractive index compared with Dubovik00&06 inversions (gray). P-type and I-type inversions are represented by green and red colors, respectively. In panels d–i, the retrievals are shown for aerosols in both fine (dotted) and coarse (dashed) modes, as well as bulk averages (solid). The PSD relevant quantities for panels a–c are summarized in Table 5.3. . . . .	84
5.4	Same as Figure 5.3, but for derived aerosol SSA and $\text{Asy}$ . . . . .	85

# List of Tables

1.1	Measurement sequences of the CIMEL CE318 SunPhotometer. . . . .	5
2.1	Elements of transformation vector for various aerosol single scattering parameters (composite of fine and coarse mode). . . . .	24
2.2	Elements of transformation vector for various microphysical parameters of fine and coarse mode aerosols <sup>a</sup> . . . . .	25
3.1	AERONET observation characteristics. . . . .	41
3.2	State vector elements and associated constraints for inversion. <sup>a</sup> . . . . .	43
4.1	The aerosol parameters defined for both fine and coarse aerosol modes <sup>a</sup> . . . . .	51
4.2	The aerosol scenarios adapted for numerical experiments <sup>a</sup> . . . . .	52
4.3	List of scenarios of AERONET observations used for information content analysis. . . . .	54
4.4	Error for retrieved and derived parameters among <i>a priori</i> , <i>a posteriori</i> , and Glory characterization <sup>a</sup> . . . . .	67
4.5	Required aerosol conditions ( $\tau_{A440}$ and AE) to achieve anticipated retrieval accuracy $< \varepsilon >$ for observations in scenario I1 and P1. . . . .	73
5.1	Main characteristics of case studies in this work. . . . .	78
5.2	Summary of measurement fitting errors. . . . .	82
5.3	PSD-related parameters retrieved by our P-type inversion, compared with values from the AERONET Dubovik00&06 inversion. . . . .	85
5.4	Errors on the retrieved and derived parameters from both types of inversion <sup>a</sup> . . . . .	87

## CHAPTER 1

### INTRODUCTION

#### 1.1 Background and Motivation

Atmospheric aerosols play a crucial role in the global climate change. They affect earth energy budget directly by scattering and absorbing solar and terrestrial radiation, and indirectly through altering the cloud formation, lifetime, and radiative properties [Haywood and Boucher, 2000; Ramanathan *et al.*, 2001]. However, quantification of these effects in the current climate models is fraught with uncertainties. The global average of aerosol effective radiative forcing were estimated to range from  $-0.1$  to  $-1.9 \text{ Wm}^{-2}$  with the best estimate of  $-0.9 \text{ Wm}^{-2}$  [Boucher *et al.*, 2013], indicating that the cooling effects of aerosol might counteract the warming effects of  $1.82 \pm 0.19 \text{ Wm}^{-2}$  caused by the increase of carbon dioxide since the industrial revolution [Myhre *et al.*, 2013]. The climate effects of aerosol particles depend on their geographical distribution, optical properties, and efficiency as cloud condensation nuclei and ice nuclei. Key quantities pertain to the aerosol optical and cloud-forming properties include particle size distribution (PSD), chemical composition, mixing state, and morphology [Boucher *et al.*, 2013]. While the daily aerosol optical depth (AOD) can be well measured from current satellite and ground-based remote sensing instrumentations [e.g., Holben *et al.*, 1998; Kaufman *et al.*, 2002], the accurate quantification of aerosol ERF is in no small part hindered by our limited knowledge about the aerosol PSD and refractive index (describing chemical composition and mixing state).

To fully understand the role of aerosol particles in the global climate change, further development in observations along with retrieval algorithms for these aerosol microphysical properties from different platforms are thus highly needed [*Mishchenko et al.*, 2004], and the focus of this two-part series study is the characterization of aerosol properties from ground-based passive remote sensing.

### 1.1.1 Previous studies on aerosol microphysical retrievals

There have been continuous efforts in determining aerosol microphysical properties from ground-based measurements of direct and/or diffuse solar radiation since *Ångström* [1929] first suggested an empirical relationship between the spectral dependency of extinction coefficients and the size of aerosol particles. Over thirty years later, *Curcio* [1961] inferred the aerosol PSD from the spectral particulate extinction coefficients in the visible and near-infrared regions. Soon with the effective numerical inversion technique developed by *Phillips* [1962] and *Twomey* [1963] specifically for error-involved optimization, a number of studies explored the use of either spectral attenuations or scattered radiances (in a small range of scattering angles) to determine the aerosol PSD [*Twomey and Howell*, 1967; *Yamamoto and Tanaka*, 1969; *Dave*, 1971; *Grassl*, 1971; *Herman et al.*, 1971; *King et al.*, 1978]. *Shaw* [1979] and *Nakajima et al.* [1983] were among the first studies that have combined optical scattering measurements with spectral extinctions to recover particle size spectrum. *Kaufman et al.* [1994] suggested useful information contained in the sky radiances of larger scattering angles to retrieve the aerosol scattering phase function and PSD. The first operational retrieval algorithm for aerosol microphysical properties was introduced by *Nakajima et al.* [1996], when the multi-band automatic sun- and sky-scanning radiometer was deployed in the AErosol RObotic NETwork, or the AERONET [*Holben et al.*, 1998]. All of above mentioned methods treated aerosol particles as homogeneous



spheres and with refractive index assumed a priori, even though the refractive index can highly impact the optical, especially the scattering characteristics [Hansen and Travis, 1974]. Tanaka *et al.* [1982, 1983] developed an inversion library method to estimate the complex refractive index and PSD simultaneously from measurements of scattered radiances polarized in the perpendicular and parallel directions. Another concept for determining refractive index from both direct and diffuse angular radiances was developed by Wendisch and Von Hoyningen-Huene [1994] and Yamasoe *et al.* [1998], which were based on the fact that sensitivities of scattered radiances to the PSD and those to the refractive index are dominated on different scattering-angular regions. The current AERONET operational inversion algorithm was developed by Dubovik and King [2000], which has heritage from algorithms developed by King *et al.* [1978] and Nakajima *et al.* [1983, 1996] but was implemented for simultaneous retrieval of particle size distribution and complex refractive index with sophisticated inclusion of multiple a priori constraints. Dubovik *et al.* [2002a, 2006] further implemented the spheroids in the particle shape consideration for desert dust in the retrieval, and added fractional volume of non-spherical particles to the inversion products.

### 1.1.2 The AERONET measurements

With over 400 locations around the world, most AERONET sites are equipped with an automatic sun and sky scanning spectral radiometer, or the CIMEL CE318 type SunPhotometer (Figure 1.1a), to routinely measure direct and diffuse solar radiation in various atmospheric window channels [Holben *et al.*, 1998]. As listed in Table 1.1 and illustrated in Figure 1.1, these measurements include direct sun radiances, sky radiance on both the solar almucantar and principal planes, as well as the optional polarization of sky light on the solar principal plane.

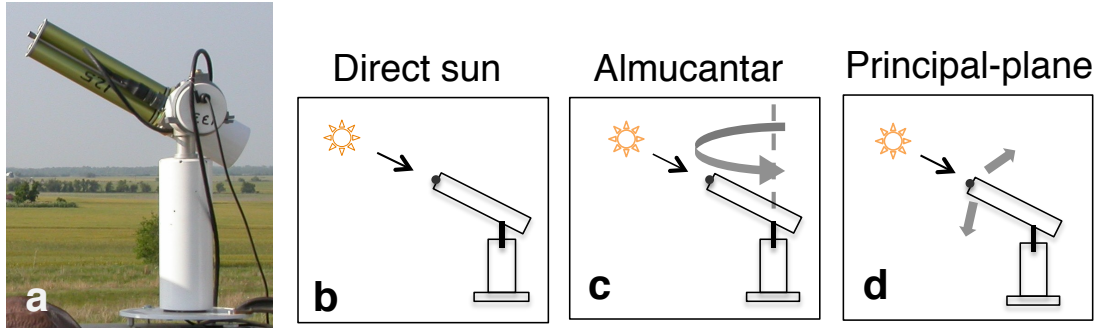


Figure 1.1: A photo of the CIMEL CE318 type SunPhotometer (a) and its observational modes: (b) direct-sun radiance scan, (b) sky-radiance scan on the solar almucantar, (c) solar principal-plane scan for sky radiance and polarization. Detail scan information are presented in Table 1.1 and text.

Direct sun radiances at various atmospheric window channels from the ultra-violet (UV) to near-infrared (NIR) are used to infer the spectral AODs with the Beer-Lambert-Bouguer Law [Holben *et al.*, 1998; Smirnov *et al.*, 2000]. Depending on site-specific instruments, AOT values are typically reported at 7 wavelengths centered at 340 nm, 380 nm, 440 nm, 500 nm, 675 nm, 870 nm, and 1020 nm. Their calibration errors are believed to as small as 0.01 for visible and NIR bands and 0.02 for UV bands.

Sky radiance measurements, which are performed at 440, 670, 870, and 1020-nm bands with full width spectrum at half maximum (FWHM) of 10 nm, are acquired from both solar almucantar and solar principal plane. An almucantar is a series of measurements taken at the viewing angle of the sun for 76 specified relative azimuthal angles (for detail see table 2 of citepholben98). To achieve an enough range of scattering angles, almucantar scans are usually made at an optical air mass of 1.7 or more (corresponding to solar zenith angle larger than about  $50^\circ$ ). The principal-plane sequence for each spectrum performs right after almucantar scans. It begins with a sun observation, moves  $6^\circ$  below the sunray, sweeps up through the sun, and ends at a scattering angle of  $150^\circ$  or viewing angle achieves horizon, collecting radiances from up to 42 viewing angles. Hereinafter, we will use  $I_{\text{alm}}$  and  $I_{\text{ppl}}$  to

Table 1.1: Measurement sequences of the CIMEL CE318 SunPhotometer.

	Spectra (nm)	Viewing Geometry (°)	Applications
Direct sun	340–1020 340–1640 <sup>a</sup>	Target to the sun	AOD, $P_w$ , AE
Almucantar ( $I_{alm}$ )	440, 675, 870, 1020 (340, 380, 500, 1640) <sup>a</sup>	Azimuth angles relative to Sun: 6, 5, 4.5, 4, 3.5, 3, 2.5, 2, -2, -2.5, -3, -3.5, -4, -4.5, -5, -6, -8, -10, -12, -14, -16, -18, -20, -25, -30, -35, -40, -45, -50, -60, -70, -80, -90, -100, -110, -120, -130, -140, -160, -180 (Duplicate above sequence for a complete counter clockwise rotation to -6)	PSD, $m_r$ , $m_i$ , SSA, phase function
Principal- plane ( $I_{ppl}$ )	Same as above	Scattering angle from Sun: -6, -5, -4.5, -4, -3.5, -3, -2.5, -2, 2, 2.5, 3, 3.5, 4, 4.5, 5, 6, 8, 10, 12, 14, 16, 18, 20, 25, 30, 35, 40, 45, 50, 60, 70, 80, 90, 100, 110, 120, 130, 140 (negative is below the Sun)	Same as above
Polarization ( $I_{pp}$ , DOLP <sub>pp</sub> )	870, (340, 380, 440, 500, 675, 870, 1020, 1640) <sup>a</sup>	Zenith angle on the solar principal plane: -85, -80, -75, -70, -65, -60, -55, -50, -45, -40, -35, -30, -25, -20, -15, -10, -5, 5, 10, 15, 20, 25, 30, 35, 40, 45, 50, 55, 60, 65, 70, 75, 80, 85 (negative is in the antisolar direction)	Not used yet

<sup>a</sup>Additional measurements taken by the newer-generation CIMEL-318DP SunPhotometer.

represent the sky radiances from the solar almucantar and solar principal plane, respectively.

These sky radiance data are used in the current AEROENT operational inversion algorithm [Dubovik and King, 2000; Dubovik et al., 2006] (hereafter Dubovik00&06) to derive: (1) the aerosol particle size distribution (PSD) in terms of the aerosol volume (in the atmospheric column) at 22 size bins, (2) the fractional volume of non-spherical particles, and (3) the complex refractive index assumed to be independent of particle size. From those microphysical parameters, the Dubovik00&06 algorithm computes the aerosol single scattering albedo (SSA) and the phase function. Uncertainties in the AERONET inversion products are 15–100% for the bin-based PSD parameters, 0.025–0.05 for real-part refractive index and 0.03 for SSA [Dubovik et al., 2000].

Light polarization measurements are performed optionally over many sites. They are measured by the SunPhotometer with three polarizers placed 60° between each axial direc-

tion. The total radiance is derived by

$$I_{\text{pp}} = \frac{2}{3} (I_1 + I_2 + I_3), \quad (1.1)$$

where  $I_1$ ,  $I_2$ , and  $I_3$  are radiance with these three polarizers, respectively. The degree of linear polarization (DOLP) of skylight is inferred by

$$\text{DOLP}_{\text{pp}} = \frac{2(I_1^2 + I_2^2 + I_3^2 - I_1 I_2 - I_2 I_3 - I_1 I_3)^{(1/2)}}{I_1 + I_2 + I_3}. \quad (1.2)$$

It should be noted that we prefer to use  $\text{DOLP}_{\text{pp}}$  instead of polarized radiance in our inversion, since as a relative quantity it is more accurate. Polarization measurements are made every hour (right after principal plane scans) at 870 nm in the principal plane at  $5^\circ$  increments between viewing zenith angle of  $-85^\circ$  and  $+85^\circ$ . These measurements are optional depending on the instrument version and configuration, and are currently available mostly over European and African stations. Recently, multi-spectral polarizations have also been taken with a newer-generation SunPhotometer (CIMEL CE318-DP) at some sites [[Li et al., 2009](#)] and the UAE<sup>2</sup> fields campaign [[Reid et al., 2008](#)]. Here we focus our study on using multi-spectral polarizations for the inversion of aerosol parameters.

### 1.1.3 Challenges and opportunities

While the AERONET AOD and other inversion products have been widely used to study the climatology of aerosol optical properties [[Dubovik et al., 2002b](#); [Levy et al., 2007a](#)] and for the development and validation of aerosol retrieval algorithms for satellite sensors such as the Moderate Resolution Imaging Spectrometer (MODIS) [[Kaufman et al., 1997](#); [Remer et al., 2005](#); [Levy et al., 2007b, 2010](#); [Wang et al., 2010](#)] and the Multi-angle Imaging SpectroRadiometer (MISR) [[Diner et al., 1998](#); [Kahn et al., 2010](#)], the AERONET

operational algorithm also faces: (i) challenges in evaluation of aerosol data either retrieved from newer-generation satellite sensors or simulated from chemistry transport models, and (ii) opportunities to improve the retrieval through the use of multi-spectral polarization measurements that are now available at a few sites and will be made available at more sites as part of the AERONET future research development (<http://aeronet.gsfc.nasa.gov>). These challenges and opportunities, as further described below, are also the motivation for us to develop a new research algorithm.

The first challenge is that newer-generation satellite sensors are expected to offer aerosol microphysical products with accuracy that is equivalent to, if not higher than, that of the current AERONET microphysical products. For instance, the Aerosol Polarimetry Sensor (APS) for the NASA Glory mission, through measuring the first three Stokes vector elements simultaneously from 250 viewing angles at nine spectral bands (410, 443, 556, 670, 865, 910, 1370, 1610, and 2200 nm), was designed to retrieve aerosol effective radius ( $r_{\text{eff}}$ ), effective variance ( $v_{\text{eff}}$ ), and spectral complex index of refraction for both fine and coarse modes [*Mishchenko et al.*, 2007]. While no actual product is available because of the failure of Glory launch, several case studies with the APS's prototype airborne sensor, RSP (the Remote Sensing Polarimeter), demonstrated feasibility of APS algorithm [*Chowdhary et al.*, 2002, 2005; *Mishchenko et al.*, 2004; *Waquet et al.*, 2009]. At least in the case of spherical particles, the accuracy of APS's bi-modal aerosol products was expected to be 10% for  $r_{\text{eff}}$ , 40% for  $v_{\text{eff}}$ , 0.02 for  $m_r$ , and 0.03 for the SSA ( $\omega_A$ ) [*Mishchenko et al.*, 2007]. Some of these accuracy expectations are unlikely to be matched by existing ground-based and in situ instruments, including those at the AERONET sites. Moreover, the current AERONET retrieval of the refractive index and the  $\omega_A$  are not recommended to use when the 440-nm AOD is lower than 0.4 [*Holben et al.*, 2006] due to expected limited accuracy identified in the detailed sensitivity study by [*Dubovik et al.*, 2000].

The second challenge is associated with the inconsistency in assumptions of PSD that

exists between current AERONET inversion products and satellite retrievals on the one hand, as well as the aerosol models used by climate models on the other hand. Specifically, the Dubovik00&06 algorithm retrieves the aerosol PSD on in 22 discrete size bins. In contrast, a continuous PSD function (e.g., lognormal) is usually assumed in satellite retrieval algorithms, such as those for APS/RSP [*Mishchenko et al., 2007; Waquet et al., 2009*] and the POLDER/PARASOL algorithm [*Hasekamp et al., 2011*]. Also, aerosol microphysical properties are usually calculated with continuous PSD assumptions in many chemistry transport models, such as GEOS-Chem [*Drury et al., 2010; Wang et al., 2010*] and the GOCART model [*Chin et al., 2002*]. Clearly, the actual aerosol PSD is never a perfect lognormal distribution, but neither it is discrete. At least from the scattering perspective, the aerosol PSD can be well characterized with an effective radius  $r_{\text{eff}}$  and an effective variance  $v_{\text{eff}}$ , while the specific function of the PSD is shown to be much less important [*Hansen and Travis, 1974*]. In other words, since the retrieval is based on the information content in the particle optical scattering, the most relevant size parameters, regardless of the PSD shape, should be  $r_{\text{eff}}$  and  $v_{\text{eff}}$ , at least for spherical particles.

The third challenge is that the assumption of a size-independent refractive index (and SSA) in Dubovik00&06 is not in line with the majority of counterpart satellite retrieval algorithms [e.g., *Mishchenko et al., 2007; Hasekamp et al., 2011; Martonchik et al., 2009*], which often uses different refractive indices for various individual aerosol modes. In many cases, tropospheric aerosol is a mixture of modes with substantially different refractive indices. For example, smoke from biomass burning can be mixed with mineral dust over western coastal North Africa [*Yang et al., 2013*]. Furthermore, the assumption of size-independent refractive index can lead to errors in the retrieval of the size distributions when the refractive indices for fine- and coarse-mode aerosols differ substantially [*Dubovik et al., 2000; Chowdhary et al., 2001*]. Thus, a mode-resolved parameterization of the refractive index in an aerosol retrieval algorithm not only can facilitate the validation of satellite

products and chemistry transport models, but also is expected to improve the accuracy of PSD and SSA retrievals for each mode. [Dubovik *et al.*, 2000] have tested the possibility of retrieving separated refractive indices of fine and coarse modes, however, they concluded that the retrieval of bi-modal refractive indices is essentially non-unique due to limited information in the AERONET radiance-only observations.

Therefore, this work aims to developing an algorithm to retrieve the aerosol microphysical properties of both fine and coarse aerosol modes, which embraces the future opportunities of deploying polarization measurements through AERONET, and ameliorates the aforementioned limitations in the Dubovik00&06 algorithm by incorporating both radiance and polarization data. Polarization measurements contain valuable information on aerosol microphysical properties [Mishchenko and Travis, 1997], as the polarization of the scattered light is highly sensitive to aerosol size and refractive index [Hansen and Travis, 1974; Mishchenko *et al.*, 2002]. We note, however, their conclusions were based on consideration of spherical aerosol particles and were primarily from a theoretical point of view. In contrast, the studies by Dubovik *et al.* [2006] and Deuzé *et al.* [1993, 2001] revealed serious limitation of polarimetric retrieval of the properties for coarse, especially non-spherical aerosols. Moreover, Dubovik *et al.* [2006] have shown that while the polarimetric observation of fine particles and large spheres are highly sensitive to real part of refractive index, even they have non-negligible sensitivity to particle shape. Therefore, adding polarization measurements to the inversion has great potential to improve the accuracy of AERONET microphysical retrievals, provided that the difficulty of representing aerosol particle shapes is recognized or adequately addressed. In these regards, most of the past efforts seem to suggest clear improvements in characterization of fine mode aerosol using polarimetric observations. For example, Li *et al.* [2009], based upon the Dubovik00&06 algorithm, demonstrated the possibility to reduce errors in the fine-mode size distribution, real part of the refractive index, and particle shape parameters.

## 1.2 Research Goals and Thesis Outline

As discussed above, this dissertation seeks to contribute an improved research algorithm retrieving aerosol microphysical properties from AERONET measurements of light radiance and polarization, with emphasis on elucidating the potentially important role of polarization measurements. It does so by pursuing the following three objectives:

1. *Develop ground-based inversion algorithms for the retrieval of aerosol refractive indices and particle size distribution from a combined use of direct and diffuse solar radiation measurements from AERONET.*

Retrieving aerosol information from remote sensing observation involves two types of development, i.e., the forward modeling and inverse modeling. In Chapter 2, I present a unified radiative transfer model—UNL-VRM—that we have developed specifically for inversion of aerosol properties from remote sensing measurements [Wang *et al.*, 2014]. The key feature of UNL-VRM is that it not only simulates the polarimetric radiation in the atmosphere but also, more importantly, can compute the analytical derivatives of these radiation fields with respect to aerosol microphysical parameters. In the subsequent chapter, I describe an inversion algorithm that is developed by integrating the UNL-VRM with a statistical optimization approach to retrieve 22 aerosol microphysical parameters from the AERONET measured multi-spectral and multi-angular light radiance and polarization.

2. *Conduct a sensitivity study and error budgeting exercise to characterize retrieval accuracy and error sources.*

In order to explore the potential of the AERONET polarization measurements for improving aerosol microphysical retrieval, our inversion testbed is used to examine the information content of these measurements with and without radiation in the Chapter



4. The analysis focuses on how the added polarization measurements impact on the retrieval accuracy the in aerosol particle size distribution, spectral refractive index, and single scattering albedo. We also investigate the how the added polarization measurements can reduce the retrieval error for these properties.
3. *Perform ground-based retrievals using available AERONET polarimetric measurements.*

In Chapter 5, I applied our new research algorithm to a suite of photo-polarimetric measurements taken from the new-generation SunPhotometer at the Beijing\_RADI AERONET station.

## CHAPTER 2

### MODEL DEVELOPMENTS

#### 2.1 Introduction

Retrieving aerosol information from remote sensing observation involves two type of development, i.e., the forward modeling and inverse modeling. Mathematically, the forward modeling constructs a complete physical system to predict the outcome of measurements. The inverse modeling uses the actual measurements to infer the values of the parameters that characterize the system. The focus of this chapter is the development of a forward model that can accurately simulate the multi-spectral and multi-angular polarimetric quantities measured by the AERONET SunPhotometer. I first present the general physics of light propagation within the atmosphere in the following text of this section. Then I describe the forward model (UNL-VRM) in section 2.2. Finally, I show the model benchmarking and verification are section 2.3.

The radiation fields—radiance and the state of polarization—measured by the AERONET SunPhotometer are the outcome of solar radiation interacting with various physical processes including the absorption and scattering by atmospheric molecules, aerosols and clouds, as well the reflection and absorption by underlying surface. The radiance and polarization of light at any wavelength can be represented by a Stokes column vector  $\mathbf{I}$  having four elements [*Hansen and Travis, 1974*]:

$$\mathbf{I} = [I, Q, U, V]^T, \quad (2.1)$$

where  $I$  is the total intensity (or radiance),  $Q$  and  $U$  describe the state of linear polarization,  $V$  describes the state of circular polarization, and  $T$  indicates a transposed matrix. It should be noted that all radiation fields and optical parameters used in this paper are functions of the light wavelength  $\lambda$ . For simplicity, however, we omit  $\lambda$  in all formulas. The degree of linear polarization (DOLP) is defined by

$$\text{DOLP} = \frac{\sqrt{Q^2 + U^2}}{I}. \quad (2.2)$$

In the solar principal plane,  $U$  is negligibly small and the above formula becomes  $\text{DOLP} = -Q/I$ . Let  $\mathbf{I}_0 = [I_0, 0, 0, 0]^T$  denote the Stokes vector for incident Solar radiation at the top of the atmosphere (TOA) from the direction  $(\theta_0, \phi_0)$ , where  $\theta_0$  and  $\phi_0$  are the incident solar zenith and azimuth angles, respectively. For a plane-parallel atmosphere bounded below by a reflective surface, the vector radiative transfer equation in the medium for the specific intensity column vector  $\mathbf{I}$  of light propagating in the viewing direction  $(\theta, \phi)$  can be written [[Hovenier et al., 2004](#); [Mishchenko et al., 2002](#)]:

$$\mu \frac{\partial \mathbf{I}(\tau, \mu, \phi)}{\partial \tau} = \mathbf{I}(\tau, \mu, \phi) - \mathbf{J}(\tau, \mu, \phi; \mu_0, \phi_0) \quad (2.3)$$

$$\begin{aligned} \mathbf{J}(\tau, \mu, \phi; \mu_0, \phi_0) = & \frac{\omega}{4\pi} \int_{-1}^1 \int_0^{2\pi} \mathbf{P}(\tau, \mu, \mu_0, \phi - \phi_0) \mathbf{I}(\tau, \mu_0, \phi_0) d\phi_0 d\mu_0 \\ & + \frac{\omega}{4\pi} \mathbf{P}(\tau, \mu, \mu_0, \phi - \phi_0) \mathbf{I}_0 \exp(-\tau/\mu_0) \end{aligned} \quad (2.4)$$

Here,  $\tau$  is the extinction optical depth measured from TOA,  $\mu$  and  $\mu_0$  are cosines of  $\theta$  and  $\theta_0$ , respectively,  $\omega$  is the SSA and  $\mathbf{P}$  is the phase matrix. The first term in equation (2.3) represents multiple scattering contributions, while the second indicates scattered light from the direct solar beam.

Parameters required to solve the above radiative transfer equation are  $\tau$ ,  $\omega$ , and  $\mathbf{P}(\Theta)$  for the atmosphere, and the reflectance matrix  $\mathbf{R}_s(\tau, \mu, \phi; \mu_0, \phi_0)$  of the underlying surface.

Considering a cloud-free atmosphere, the solar radiation is attenuated by molecular scattering, gaseous absorption, and aerosol scattering and absorption. For a given layer, we have

$$\tau = \tau_A + \tau_R + \tau_G \quad (2.5)$$

$$\omega = \frac{\tau_A \omega_A + \tau_R}{\tau} \quad (2.6)$$

$$\mathbf{P}(\Theta) = \mathbf{P}_A(\Theta) \frac{\tau_A \omega_A}{\tau_A \omega_A + \tau_R} + \mathbf{P}_R(\Theta) \frac{\tau_R}{\tau_A \omega_A + \tau_R} \quad (2.7)$$

where  $\tau_A$ ,  $\tau_R$ , and  $\tau_G$  are optical depth, respectively, by aerosol extinction, Rayleigh scattering of air density fluctuations, and gaseous absorption.  $\omega_A$  is the SSA of aerosol, and  $\mathbf{P}_A(\Theta)$  and  $\mathbf{P}_R(\Theta)$  are, respectively, the aerosol and Rayleigh phase matrices as functions of the scattering angle  $\Theta$ . Therefore, the forward modeling development thus requires the computation of single scattering properties for aerosols and air density fluctuations, rigorous treatment for absorption of trace gases, accurate representation of reflectance/polarization by surface, and the realistic simulation of polarimetric radiative transfer.

## 2.2 The UNL-VRTM

We have developed the UNified Linearized Vector Radiative Transfer Model, or UNL-VRTM, specifically for simulation, analysis, and inversion of the photo-polarimetric measurements. As shown in Figure 2.1, the UNL-VRTM comprises 6 modules; they are

1. A module computing Rayleigh scattering (section 2.2.1);
2. A module that deal with gaseous absorption (section 2.2.1);
3. A linearized Mie scattering code (section 2.2.2);
4. A linearized T-matrix electromagnetic scattering code (section 2.2.2);

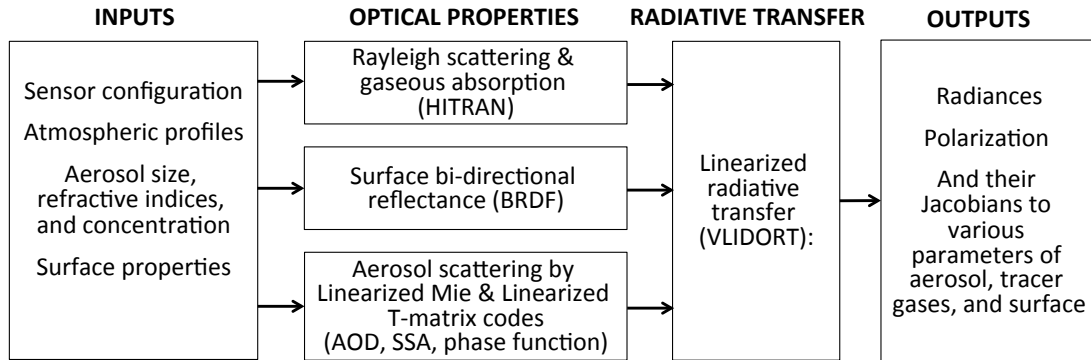


Figure 2.1: Flowchart of the UNL-VRTM components. See text for detail.

5. A surface model computing various bidirectional reflectance/polarization functions (BRDF/BPDF) (section 2.2.3);
6. A vector linearized radiative transfer model—VLIDORT (section 2.2.4).

These modules are integrated for the forward calculation of aerosol single scattering, gas absorption, and vector radiative transfer hereafter, and thus they together constitute the Unified Linearized Radiative Transfer Model, UNL-VRTM.

Inputs for the UNL-VRTM are profiles of atmospheric properties and constituents (temperature, pressure, aerosol mass concentration or layer AOD, water vapor amount and other trace gas volume mixing ratio profiles [McClatchey *et al.*, 1972]), the surface properties, as well as the aerosol parameters (such as PSD parameters and refractive index) themselves. Bearing in mind the lack of sensitivity in passive remote sensing for the retrieval of vertical profiles of aerosol properties, the UNL-VRTM as it stands now is only designed to deliver radiative calculations for a maximum of two sets of aerosol single scattering properties (e.g., aerosol PSD, refractive index, and particle shape), typically with one fine-mode and one coarse-mode aerosol. Other inputs for model include spectral and geometrical definitions that characterizing specification of an observing sensor.

Outputs of the model include the Stokes vector ( $\mathbf{I}$ ) at user-defined spectral wavelengths and desired atmospheric levels for both upwelling and downwelling radiation, from which the light radiance and degree of polarization can be derived. Outputs also include analytical Jacobians of  $\mathbf{I}$  with respect to all aerosol particle parameters (PSD, refractive index, vertical profile), Rayleigh scattering optical depth, optical depth of all trace gases, and parameters describing surface optical property. A detail description of the UNL-VRM's Jacobian capability is presented in section 2.2.5.

Although the UNL-VRM is used to simulate the AERONET measurements in this work, the module-based structure of UNL-VRM allows its application not limit to the AERONET inversion. It can be easily used to simulate observations from other remote sensing platforms, like satellite sensors. For example, we have employed it to explore the aerosol information content of observations from the future TEMPO/GEO-CAPE geostationary satellite sensors [Wang *et al.*, 2014], to investigate the potential application of hyperspectral radiances at O<sub>2</sub>A and O<sub>2</sub>B bands for retrieving aerosol vertical profile [Wang *et al.*, 2014; Ding *et al.*, 2014], to retrieve aerosol microphysical properties from GeoTASO measured UV-to-visible continuous radiance spectra [Hou *et al.*, 2014], and to perform AOD retrieval from GOSAT/TANSO-CAI's UV radiance [Han *et al.*, 2014].

Recently, we have made the UNL-VRM publicly accessible. We published the source code on <http://meteo.unl.edu/~xxu/unlvrtm.php>. A detail description and a dedicated User's Guide for the model is also available on the webpage.

### 2.2.1 Molecular scattering and absorption

The Rayleigh scattering optical depth at certain wavelength in any atmospheric layer ( $\tau_R$ ) is computed by

$$\tau_R = N_{\text{air}} \sigma_R \quad (2.8)$$

where  $N_{\text{air}}$  is air molecular number density of that layer ( $\text{molec cm}^{-2}$ ), and  $\sigma_{\text{R}}$  is the Rayleigh scattering cross-section ( $\text{cm}^2 \text{ molec}^{-1}$ ) computed following [Bodhaine et al. \[1999\]](#). The Rayleigh phase matrix,  $\mathbf{P}_{\text{R}}(\Theta)$ , depends upon molecular anisotropy through the depolarization factor, also computed from the same source. [Bodhaine et al. \[1999\]](#) computes the wavelength-dependent Rayleigh scattering cross-section as a function of mixing ratios for  $\text{N}_2$ ,  $\text{O}_2$ ,  $\text{H}_2\text{O}$ , and  $\text{CO}_2$ . The phase matrix for Rayleigh scattering follows [Hansen and Travis \[1974\]](#); we use the set of spherical-function expansion coefficients for the phase matrix as supplied for VLIDORT [[Spurr, 2006](#)].

Calculation of the absorption optical depth ( $\tau_{\text{G}}$ ) at any atmospheric layer for  $K$  different trace gases follows

$$\tau_{\text{G}} = \sum_{i=1}^K N_{\text{gas},i} \sigma_{\text{A},i}(T, P) \quad (2.9)$$

where  $N_{\text{gas},i}$  is the number density of  $i$ th gas within that layer, and  $\sigma_{\text{A},i}$  is the corresponding absorption cross-section, a function of temperature and pressure. Our model accounts for absorptions by a total number of 22 trace gases:  $\text{H}_2\text{O}$ ,  $\text{CO}_2$ ,  $\text{O}_3$ ,  $\text{N}_2\text{O}$ ,  $\text{CO}$ ,  $\text{CH}_4$ ,  $\text{O}_2$ ,  $\text{NO}$ ,  $\text{SO}_2$ ,  $\text{NO}_2$ ,  $\text{NH}_3$ ,  $\text{HNO}_3$ ,  $\text{OH}$ ,  $\text{HF}$ ,  $\text{KCl}$ ,  $\text{HBr}$ ,  $\text{HI}$ ,  $\text{ClO}$ ,  $\text{OCS}$ ,  $\text{H}_2\text{CO}$ ,  $\text{HOCl}$ , and  $\text{N}_2$ . The determination of  $\sigma_{\text{A}}$  utilizes a UV-to-visible cross-section library and the line-spectroscopic absorption parameters archived in the HITRAN database [[Orphal and Chance, 2003](#); [Rothman et al., 2009](#)]. The cross-section library compiles the extinction cross-section for  $\text{O}_3$ ,  $\text{NO}_2$ ,  $\text{SO}_2$ , and  $\text{O}_2\text{--O}_2$  in the UV and/or visible spectral regions. Meanwhile, line-spectroscopic absorption databased are used to simulate the pressure- and temperature-dependent extinction cross-section with line-by-line (LBL) approach [[Liou, 2002](#); [Rothman et al., 2009](#)] by accumulating each individual absorption line. Doppler broadening is calculated from the molecular mass and the temperature, and Doppler and Lorentz broadening are included in the Voigt calculation.

Particular to work, we only consider the most influential trace species for the AERONET

spectral bands:  $\text{H}_2\text{O}$  (vapor),  $\text{O}_3$ , and  $\text{NO}_2$ . In our algorithm (section 3), the columnar amounts of  $\text{O}_3$  and  $\text{NO}_2$  are dynamically adjusted with retrievals from the Ozone Monitoring Instrument (OMI) [Levelt *et al.*, 2006] on board the AURA satellite. We apply the columnar water vapor amount retrieved from the 940-nm radiances measured by the AERONET SunPhotometer Halthore *et al.* [1997].

### 2.2.2 Aerosol single scattering

Aerosol single scattering properties necessary to the radiative transfer calculation include aerosol optical depth ( $\tau_A$ ) ( $Q_{\text{ext}}$ ), SSA ( $\omega_A$ ), and scattering phase matrix ( $\mathbf{P}_A(\Theta)$ ). The calculation of these parameters is made with a Linearized Mie (LMIE) scattering electromagnetic code for spherical particles and a Linearized T-matrix (LTMATRIX) scattering code for non-spherical convex and axially symmetric particles [Spurr *et al.*, 2012]. The LMIE code originates from the Mie code of de Rooij and Stap [1984], and the LTMATRIX code originates from the T-Matrix code developed by Mishchenko *et al.* [1996]; Mishchenko and Travis [1998]; both include linearization capability developed by Spurr *et al.* [2012].

Common inputs for both codes are the complex refractive index ( $m_r + im_i$ ), and the particle size distribution (PSD) parameters for polydisperse scattering. The codes have several options to specify the PSD function: two-parameter gamma, two-parameter lognormal, three-parameter modified gamma, and four-parameter bi-lognormal. In addition, the linearized T-matrix code offers options to characterize the shape of non-spherical aerosols (spheroids, cylinders, or Chebyshev particles) [Spurr *et al.*, 2012]. For non-spherical particles, the specified size distribution is interpreted as the equivalent surface-area sphere in the linearized T-matrix calculation, regardless of the shape.

For AERONET inversion algorithm, we assume that the aerosol volume distribution follows a bi-modal lognormal function [in agreement with Schuster *et al.*, 2006; Waquet *et al.*,



2009]:

$$\frac{dV}{d\ln r} = \sum_{i=1}^2 \frac{V_0^i}{\sqrt{2\pi} \ln \sigma_g^i} \exp \left[ -\frac{(\ln r - \ln r_v^i)^2}{2 \ln^2 \sigma_g^i} \right] \quad (2.10)$$

where  $V_0$ ,  $r_v$ , and  $\sigma_g$  are the total volume concentration, geometric median radius, and standard deviation, respectively. The superscript  $i$  indicates the size mode, and later will be replaced by ‘f’ for fine mode and ‘c’ for coarse mode. We assume that particle size ranges from 0.01 to 10  $\mu\text{m}$  for the fine mode and from 0.05 to 20  $\mu\text{m}$  for the coarse mode, both covering  $> 99.9\%$  of the total volume of an idealistic size range  $(0, +\infty)$ . An advantage of the lognormal distribution is that standard deviations for the number, area, and volume PSD functions are identical, and therefore allowing that the median radii for these PSD functions can be converted from one to another [Seinfeld and Pandis, 2006]. The  $r_{\text{eff}}$  and  $v_{\text{eff}}$  are related to the geometric parameters through:

$$r_{\text{eff}} = r_v \exp \left( -\frac{1}{2} \ln^2 \sigma_g \right), \quad (2.11)$$

$$v_{\text{eff}} = \exp (\ln^2 \sigma_g) - 1. \quad (2.12)$$

The LMIE/LTMATRIX code computes the aerosol extinction efficiency factor  $Q_{\text{ext}}$ , single scattering albedo  $\omega_A$ , and phase matrix  $\mathbf{P}_A(\Theta)$ , as well as Jacobians of these quantities with respect to input parameters including  $r_{\text{eff}}$ ,  $v_{\text{eff}}$ ,  $m_r$ , and  $m_i$ . The phase matrix and its Jacobians are expressed in terms of the coefficients  $\mathbf{B}_A(\Theta)$  for each moment  $l$  in terms of the generalized spherical function expansions for each non-zero phase matrix element. Let  $\mathbf{A}$  denotes the vector of aerosol microphysical parameters,  $\mathbf{A} = [V_0, r_{\text{eff}}, v_{\text{eff}}, m_r, m_i]^T$ , and  $\mathbf{M}$  the vector of aerosol optical parameters,  $\mathbf{M} = [\tau_A, \omega_A, \mathbf{B}_A(\Theta)]^T$ , where  $\tau_A$  is related to  $Q_{\text{ext}}$  by  $\tau_A = \frac{3V_0 Q_{\text{ext}}}{4r_{\text{eff}}}$ . The LMIE/LTMATRIX code acts as an operator that maps vector  $\mathbf{A}$  to  $\mathbf{M}$ . The Jacobian matrix of  $\mathbf{M}$  with respect to  $\mathbf{A}$  calculated by means of the linearization feature of the code, and it can be expressed by  $\nabla_{\mathbf{A}} \mathbf{M}$ .

### 2.2.3 Surface representations

VLIDORT has a supplementary module for specification of the surface BRDF as a linear combination of (up to) three semi-empirical kernel functions; for details, see [Spurr \[2004\]](#). This supplementary module can also provide partial derivatives of the BRDF with respect to the kernel weighting factors or with respect to kernel parameters such as the wind speed for glitter reflectance. These kernel functions include Lambertian, Ross-Thick, and Li-Sparse functions [[Wanner et al., 1995](#); [Lucht et al., 2000](#)], a Bi-directional Polarization Distribution Function (BPDF) [[Maignan et al., 2009](#)], and an ocean surface model based on the Cox-Munk model [[Cox and Munk, 1954](#)]. In addition, VLIDORT has an option for using a surface-leaving radiation field, either as a fluorescence term or as a water-leaving term expressed as a function of chlorophyll absorption.

Although surface reflectance has in general a low influence on AERONET down-welling sky radiances and polarization, a state-of-the-art representation of the surface reflectivity potentially reduces model uncertainties, especially for measurements taken at low elevation angles that could be affected by surface diffusion. Here, we utilize the spectral BRDF parameters from the MODIS surface products that are operationally reported every 16 days at a 1-km resolution [[Lucht et al., 2000](#)]. Here we use time-matched MODIS BRDF products to reconstruct the bidirectional reflectance over AERONET stations. The MODIS BRDF product supplies three weighting parameters ( $f_{\text{iso}}$ ,  $f_{\text{vol}}$ , and  $f_{\text{geo}}$ ) for the first 7 MODIS bands, respectively, corresponding to three kernel types: isotropic, Ross-Thick ( $K_{\text{vol}}$ ), and Li-Sparse ( $K_{\text{geo}}$ ):

$$\rho_{\text{R}}(\mu, \phi; \mu_0, \phi_0) = f_{\text{iso}} + f_{\text{vol}}K_{\text{vol}}(\mu, \phi; \mu_0, \phi_0) + f_{\text{geo}}K_{\text{geo}}(\mu, \phi; \mu_0, \phi_0) \quad (2.13)$$

Expanded expressions for  $K_{\text{vol}}$  and  $K_{\text{geo}}$  appear in [Wanner et al. \[1995\]](#); [Lucht et al. \[2000\]](#).

Studies have shown that the BPDF for land surfaces is generally rather small and is “spectrally neutral” [Nadal and Breon, 1999; Maignan *et al.*, 2004, 2009; Waquet *et al.*, 2007; Litvinov *et al.*, 2011]. Most empirical BPDF models are based on Fresnel coefficients of light reflectance from the surface. Here we have incorporated the one-parameter model developed by Maignan *et al.* [2009], which was derived from analyses of several years of POLDER/PARASOL measurements. This model describes the polarized reflectance at any viewing geometry  $(\mu, \phi)$  from the given incident geometry  $(\mu_0, \phi_0)$  as:

$$\rho_P(\mu, \phi; \mu_0, \phi_0) = \frac{C_0 \exp(-\tan \theta_h) \exp(-NDVI)}{\mu_0 + \mu} \mathbf{F}_P(\theta_h, n_v) \quad (2.14)$$

where  $C_0$  is a constant parameter chosen for a certain surface type,  $\theta_h$  is half of the phase angle of reflectance,  $n_v$  is the refractive index of vegetation (1.5 is used), and  $\mathbf{F}_P$  is the Fresnel reflection matrix. We chose a spectrally-independent value for  $C_0$  based on the recommendations by Maignan *et al.* [2009] for relevant surface types.

The combination of the BRDF and BPDF for land surface follows the discussion by Dubovik *et al.* [2011]. The surface reflectance matrix  $\mathbf{R}_s(\mu, \phi; \mu_0, \phi_0)$  is represented as a sum of diffuse unpolarized reflectance and specular reflectance; the former is modeled using the MODIS BRDF in equation (2.13), and the latter using the BPDF formula in equation (2.14).

## 2.2.4 Radiative transfer

The radiative transfer equation (2.3) is solved with the Vector Linearized Discrete Ordinate Radiative Transfer (VLIDORT) model, which is a core part of the UNL-VRM. VLIDORT, developed by Spurr [2006], is a linearized pseudo-spherical vector discrete ordinate radiative transfer model for multiple scattering of diffuse radiation in a stratified multi-layer atmosphere. It computes four elements of the Stokes vector  $\mathbf{I}$  for downwelling and upwelling

radiation at any desired atmospheric level. The VLIDORT includes the pseudo-spherical approximation to calculate solar beam attenuation in a curved medium. It also uses the delta-M approximation for dealing with sharply peaked forward scattering. Specifically for the AERONET inversion, we consider 16 discrete ordinate streams in the radiative transfer calculation and retain 180 terms in the spherical-function expansion of the scattering matrix to ensure accurate calculation of diffuse radiation.

Along with the Stokes vector  $\mathbf{I}$ , VLIDORT also computes the Jacobian matrix of  $\mathbf{I}$  with respect to aerosol optical vector  $\mathbf{M}$ ,  $\nabla_{\mathbf{M}}\mathbf{I}$ . Therefore, the combination of the VLIDORT and the LMIE/LTMATRIX codes allows for a direct calculation of the Jacobian matrix of the Stokes vector with respect to aerosol microphysics,  $\mathbf{A}$ , by

$$\nabla_{\mathbf{A}}\mathbf{I} = \nabla_{\mathbf{M}}\mathbf{I} \cdot \nabla_{\mathbf{A}}\mathbf{M} \quad (2.15)$$

Essentially, the above equation can yield the derivatives of the radiance  $I$  and DOLP with respect to any aerosol microphysical parameter, i.e.,  $\nabla_{\mathbf{A}}I$  and  $\nabla_{\mathbf{A}}\text{DOLP}$ . While obtaining  $\nabla_{\mathbf{A}}I$  is straightforward,  $\nabla_{\mathbf{A}}\text{DOLP}$  can be derived from equation (2.2) following:

$$\nabla_{\mathbf{A}}\text{DOLP} = -\frac{\text{DOLP}\nabla_{\mathbf{A}}}{I} + \frac{Q\nabla_{\mathbf{A}}Q + U\nabla_{\mathbf{A}}U}{I\sqrt{Q^2 + U^2}} \quad (2.16)$$

### 2.2.5 Capability of calculating Jacobians

This section analytically derives the Jacobian of  $\mathbf{I}$  with respect to various aerosol related parameters, including  $\tau_{\mathbf{A}}$ ,  $\omega_{\mathbf{A}}$ ,  $\mathbf{B}_{\mathbf{A}}$ , refractive index, PSD parameters, and aerosol vertical profile. Computation of the Stokes vector in VLIDORT requires input of an optical property set  $[\tau, \omega, \langle \mathbf{B}^j \rangle_{j=0,J}]$  for each atmospheric layer, where  $\langle \rangle_{j=0,J}$  denotes the vector that consists of elements having the similar expression as that inside  $\langle \rangle$  but for  $j = 0, J$ . For each atmospheric layer  $L$ , the optical property inputs are assumed constant and are given

by equations (2.5)–(2.6), as well as equation (2.7) with  $\mathbf{P}(\Theta)$  replaced by  $\mathbf{B}^j$ . It should be noted that all parameters in these equations are for each layer, but we ignore  $L$  for convenience.

Since VLIDORT generates Jacobians with respect to layer-integrated single scattering properties in each atmospheric layer as well as column-integrated single scattering property as a whole, and LMIE and LTMATRIX offer the sensitivity of aerosol scattering properties to microphysical aerosol physical parameters, an integrated use of VLIDORT and LTMATRIX/LMIE can, in principle, provide the Jacobians of Stokes parameters with respect to both aerosol single scattering properties as well as aerosol microphysical parameters (as expressed by equations (2.15)–(2.16)). Practically, the VLIDORT calculation of Jacobians of any Stokes parameter  $\xi$  with respect to any aerosol parameter  $x$  proceeds according to

$$\begin{aligned} x \frac{\partial \xi}{\partial x} &= x \left[ \frac{\partial \xi}{\partial \tau}, \frac{\partial \xi}{\partial \omega}, \left\langle \frac{\partial \xi}{\partial \mathbf{B}^j} \right\rangle_{j=1,J} \right] \left[ \frac{\partial \tau}{\partial x}, \frac{\partial \omega}{\partial x}, \left\langle \frac{\partial \mathbf{B}^j}{\partial x} \right\rangle_{j=1,J} \right]^T \\ &= \left[ \tau \frac{\partial \xi}{\partial \tau}, \omega \frac{\partial \xi}{\partial \omega}, \left\langle \mathbf{B}^j \frac{\partial \xi}{\partial \mathbf{B}^j} \right\rangle_{j=1,J} \right] \left[ \phi_x, \varphi_x, \langle \Psi_x^j \rangle_{j=1,J} \right]^T. \end{aligned} \quad (2.17)$$

The first square bracket on the right-hand side of equation (2.17) contains quantities computed internally by VLIDORT, while the second so-called “transformation vector” must be supplied by users and is defined as:

$$\phi_x = \frac{x}{\tau} \frac{\partial \tau}{\partial x}; \quad \varphi_x = \frac{x}{\omega} \frac{\partial \omega}{\partial x}; \quad \Psi_x^j = \frac{x}{\mathbf{B}^j} \frac{\partial \mathbf{B}^j}{\partial x}. \quad (2.18)$$

As we are interested in aerosol parameters, this transformation vector can be further expanded as

$$\left[ \phi_x, \varphi_x, \langle \Psi_x^j \rangle_{j=1,J} \right]^T = \Pi \left[ \phi'_x, \varphi'_x, \langle \Psi'^j_x \rangle_{j=1,J} \right]^T, \quad (2.19)$$

Table 2.1: Elements of transformation vector for various aerosol single scattering parameters (composite of fine and coarse mode).

$x$	$\phi_x$	$\varphi_x$	$\Psi_x^j$
$\tau_A$	$\frac{\tau_A}{\tau}$	$\frac{\tau_A}{\tau} \left( \frac{\omega_A}{\omega} - 1 \right)$	$\begin{cases} \frac{\omega_A \tau_A}{\omega \tau} \left( \frac{\mathbf{B}_A^j}{\mathbf{B}^j} - 1 \right) & \text{for } j < 3 \\ \frac{\tau_R}{\omega \tau} & \text{for } j \geq 3 \end{cases}$
$\omega_A$	0	$\frac{\tau_A \omega_A}{\tau \tau_A \omega_A + \tau_R}$	Same as above
$B_A^j$	0	0	$\begin{cases} \frac{\omega_A \tau_A \mathbf{B}_A^j}{\omega_A \tau_A \mathbf{B}_A^j + \tau_R \mathbf{B}_R^j} & \text{for } m = j < 3 \\ 1 & \text{for } m = j \geq 3 \\ 0 & \text{for } m \neq j \end{cases}$

where

$$\phi'_x = x \frac{\partial \tau_A}{\partial x}, \quad \varphi'_x = x \frac{\partial \delta_A}{\partial x}, \quad \text{and } \Psi_x'^j = x \frac{\partial \mathbf{B}_A^j}{\partial x}, \quad (2.20)$$

and  $\mathbf{\Pi}$  is a matrix expressed by

$$\mathbf{\Pi} = \begin{bmatrix} \frac{1}{\tau} & \mathbf{0} & \mathbf{0} \\ -\frac{1}{\tau} & \frac{1}{\delta_A + \tau_R} & \mathbf{0} \\ \mathbf{0} & \left\langle \frac{\mathbf{B}_A^j - \mathbf{B}_R^j}{\mathbf{B}^j (\delta_A + \tau_R)} \right\rangle_{j=1,J} & \left\langle \frac{\delta_A}{\mathbf{B}^j (\delta_A + \tau_R)} \right\rangle_{j=1,J} \end{bmatrix}. \quad (2.21)$$

Here,  $\delta_A$  is the scattering optical depth of aerosols. The detailed derivations of the matrix  $\mathbf{\Pi}$  are presented in Appendix C. Hence, the transformation vector for calculating Stokes profile Jacobians with respect to  $\tau_A$ ,  $\omega_A$ ,  $\mathbf{B}_A^j$  can be obtained by combining equations (2.19) and (2.21), and the components of this vector are listed in Table 2.1.

In an atmosphere where both fine (superscript “f”) and coarse (superscript “c”) aerosol particles co-exist, the ensemble aerosol optical properties may be derived by assuming external mixing:

$$\begin{cases} \tau_A &= \tau_A^f + \tau_A^c \\ \delta_A &= \delta_A^f + \delta_A^c \\ \mathbf{B}_A^j &= \frac{\delta_A^f + \delta_A^c}{\delta_A^f \mathbf{B}_A^{f,j} + \delta_A^c \mathbf{B}_A^{c,j}} \end{cases} \quad (2.22)$$

Table 2.2: Elements of transformation vector for various microphysical parameters of fine and coarse mode aerosols<sup>a</sup>.

$x$	$\phi'_{x^f}$	$\phi'_{x^f}$	$\Psi'^j_{x^f}$
$\tau_A^f$	$\tau_A^f$	$\delta_A^f$	$\frac{\delta_A^f}{\tau_A^f}(\mathbf{B}_A^{fj} - \mathbf{B}_A^j)$
$\omega_A$	0	$\delta_A^f$	$\frac{\delta_A^f}{\tau_A^f}(\mathbf{B}_A^{fj} - \mathbf{B}_A^j)$
$V_0^f$	$\frac{3V_0^f Q_{\text{ext}}^f}{4r_{\text{eff}}^f}$	$\frac{3V_0^f Q_{\text{sca}}^f}{4r_{\text{eff}}^f}$	$\frac{\delta_A^f}{\tau_A^f}(\mathbf{B}_A^{fj} - \mathbf{B}_A^j)$
$m_{\text{r}}^f, m_{\text{i}}^f$	$\tau_A^f \frac{x^f}{Q_{\text{ext}}^f} \frac{\partial Q_{\text{ext}}^f}{\partial x^f}$	$\delta_A^f \frac{x^f}{Q_{\text{sca}}^f} \frac{\partial Q_{\text{sca}}^f}{\partial x^f}$	$\frac{\phi'_{x^f}}{\delta_A^f}(\mathbf{B}_A^{fj} - \mathbf{B}_A^j) + x^f \frac{\partial \mathbf{B}_A^{fj}}{\partial x^f}$
$r_{\text{g}}^f, \sigma_{\text{g}}^f, \epsilon^f$	$\tau_A^f \left( \frac{x^f}{Q_{\text{ext}}^f} \frac{\partial Q_{\text{ext}}^f}{\partial x^f} - \frac{x^f}{r_{\text{eff}}^f} \frac{\partial r_{\text{eff}}^f}{\partial x^f} \right)$	$\delta_A^f \left( \frac{x^f}{Q_{\text{sca}}^f} \frac{\partial Q_{\text{sca}}^f}{\partial x^f} - \frac{x^f}{r_{\text{eff}}^f} \frac{\partial r_{\text{eff}}^f}{\partial x^f} \right)$	$\frac{\phi'_{x^f}}{\delta_A^f}(\mathbf{B}_A^{fj} - \mathbf{B}_A^j) + x^f \frac{\partial \mathbf{B}_A^{fj}}{\partial x^f}$
$H^f$	$H^f \frac{\partial \tau_A^f}{\partial H^f}$	$\phi'_{x^f} \omega_A^f$	$\frac{\delta_A^f}{\tau_A^f}(\mathbf{B}_A^{fj} - \mathbf{B}_A^j)$

<sup>a</sup> Expressions are shown only for fine-mode parameters; expressions for coarse-mode parameters are the same but with superscripts replaced by 'c'

We can generate the transformation vectors (as listed in Table 2.2) for any of the following parameters:  $\tau_A^f$ ,  $\omega_A^f$ ,  $V_0^f$ ,  $m_{\text{r}}^f$ ,  $m_{\text{i}}^f$ ,  $r_{\text{g}}^f$ ,  $\sigma_{\text{g}}^f$ ,  $\epsilon^f$ ,  $H^f$ , and  $\tau_A^c$ ,  $\omega_A^c$ ,  $V_0^c$ ,  $m_{\text{r}}^c$ ,  $m_{\text{i}}^c$ ,  $r_{\text{g}}^c$ ,  $\sigma_{\text{g}}^c$ ,  $\epsilon^c$ , and  $H^c$ . Here,  $r_{\text{g}}$ ,  $\sigma_{\text{g}}$ , and  $H$  denote the median and standard deviation of the particle radius (e.g., two parameters in the log-normal aerosol number distribution), and the scale height of aerosol extinction, respectively.  $V_0$  is the aerosol volume concentration and  $\epsilon$  the shape factor of the non-spherical particle. Details of the algebra for deriving the transformation vectors may be found in Appendix C. Note that the shape of the aerosol extinction vertical profile in the testbed is assumed to be constant or exponentially decreasing with height or quasi-Gaussian (Appendix C). The analytical formulas for  $\phi'_{x^f}$ ,  $\phi'_{x^c}$ , and  $\Psi'^j_{x^f}$  for coarse mode aerosol parameters are the same as their counterparts for fine-mode aerosols; we need only replace superscript “s” with “c” in Table 3 entries. Jacobians with respect to the fine mode fraction, either in terms of AOD ( $\text{fmf}_{\tau}$ ) or in terms of the volume concentration ( $\text{fmf}_v$ ), can be derived from the corresponding Jacobians with respect to modal AOD and volume,

respectively:

$$\text{fmf}_\tau \frac{\partial \xi}{\partial \text{fmf}_\tau} = \tau_A^f \frac{\partial \xi}{\partial \tau_A^f} - \frac{\text{fmf}_\tau}{1 - \text{fmf}_\tau} \tau_A^c \frac{\partial \xi}{\partial \tau_A^c} \quad (2.23)$$

$$\text{fmf}_v \frac{\partial \xi}{\partial \text{fmf}_v} = V_0^f \frac{\partial \xi}{\partial V_0^f} - \frac{\text{fmf}_v}{1 - \text{fmf}_v} V_0^c \frac{\partial \xi}{\partial V_0^c} \quad (2.24)$$

Details of these necessary VLIDORT inputs are presented in Appendix C, and a comprehensive verification of these Jacobian calculation are presnted in following section 2.3.

## 2.3 Model Benchmarking and Verifications

Figure 2.2a shows the downward solar spectral irradiance at the top-of-atmosphere and at the surface for a solar zenith angle of  $30^\circ$ . Spectral regions dominated by gas absorption can be clearly identified, including the  $\text{O}_3$  Hartley-Huggins bands in the UV, the  $\text{O}_2\text{B}$  band ( $0.69 \mu\text{m}$ ) and  $\text{O}_2\text{A}$  band ( $0.76 \mu\text{m}$ ), as well as a number of water vapor bands. The spectroscopic calculations shown in Figure 2.2 were performed at a resolution of  $0.01 \text{ nm}$ . In general this resolution is high enough to pick up fine structure in gas absorptions. In the UV below  $300 \text{ nm}$ , and in parts of the  $\text{O}_2\text{A}$  and  $\text{O}_2\text{B}$  bands, whole-atmosphere gas absorption optical depths can reach 50 or more, and the downward irradiance is nearly zero at the ground (Figure 2.2b). The inset in Figure 2.2b shows a close-up view of the fine structure in absorption optical depth for the  $\text{O}_2\text{A}$  band, with dual peaks centered at  $0.761 \mu\text{m}$  and  $0.764 \mu\text{m}$ , and a deep, narrow valley around  $0.762 \mu\text{m}$ . Similarly, the continuum of water vapor absorption from the near-infrared to about  $4 \mu\text{m}$  is also well simulated (Figure 2.2c). Also of note is the non-negligible absorption of  $\text{SO}_2$  and  $\text{NO}_2$  in UV and blue wavelength regions respectively (Figure 2.2d). In urban regions, high  $\text{SO}_2$  and  $\text{NO}_2$  can together contribute optical depths of around  $0.03\text{--}0.07$  (Figure 2.2d). Hence, in order to take advantage of low surface reflectance in the UV and the use of deep-blue wavelengths for



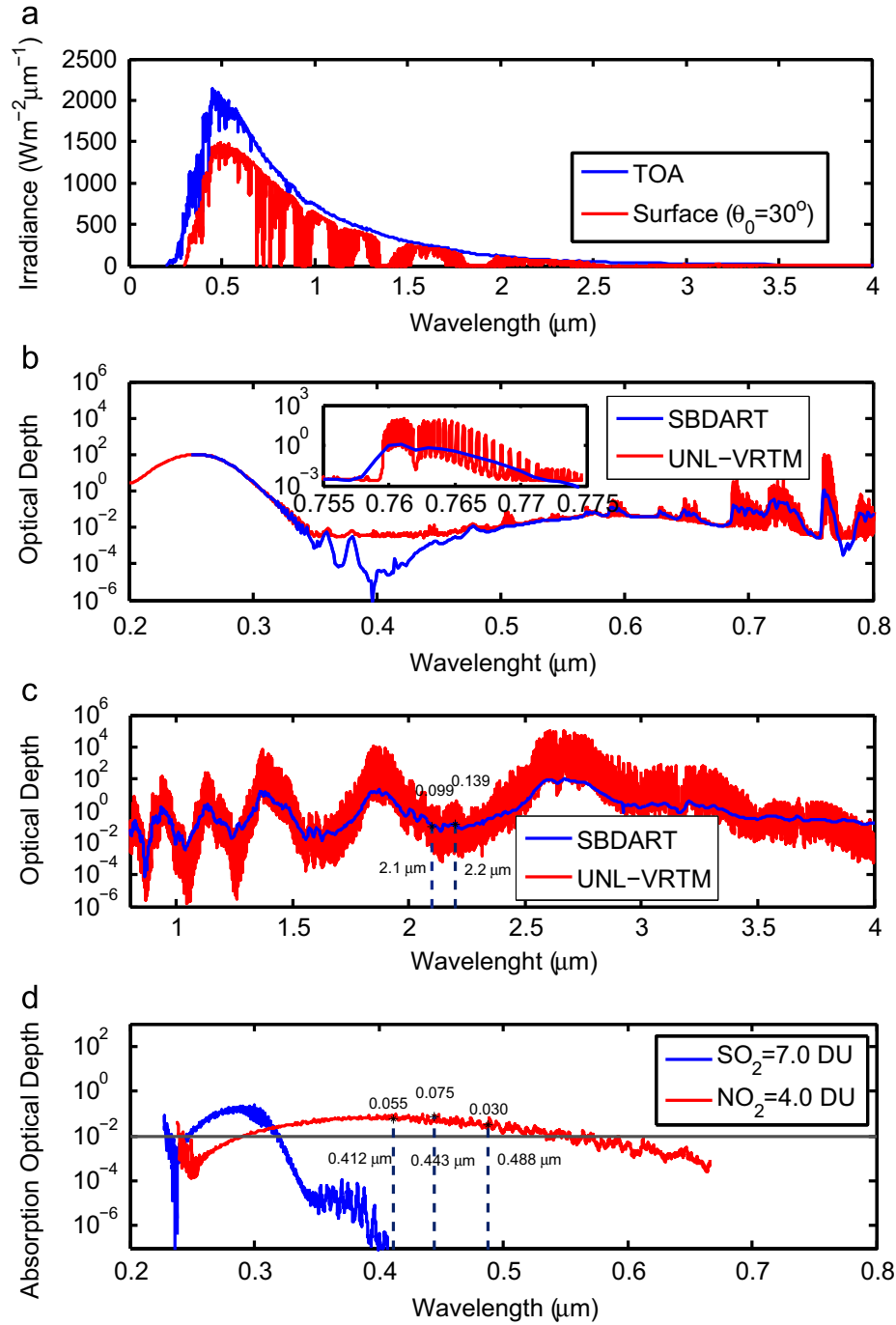


Figure 2.2: Some benchmark simulations by the UNL-VRM: (a) Downward solar spectral irradiance at the TOA and the surface for solar zenith angle of  $30^\circ$ . (b) Total-atmosphere gas absorption optical depth in the range 0.2–0.8  $\mu\text{m}$ . (c) Same as (b) but for 0.8–4  $\mu\text{m}$ . (d) Optical depth of  $\text{SO}_2$  and  $\text{NO}_2$  in polluted cases. Also shown in (b) and (c) are the optical depth computed from Santa Barbara DISORT Atmospheric Radiative Transfer (SBDART) model [Ricchiazzi *et al.*, 1998]. The mid-latitude summer atmospheric profile is assumed [McClatchey *et al.*, 1972]. (Figure adopted from Wang *et al.* [2014].)

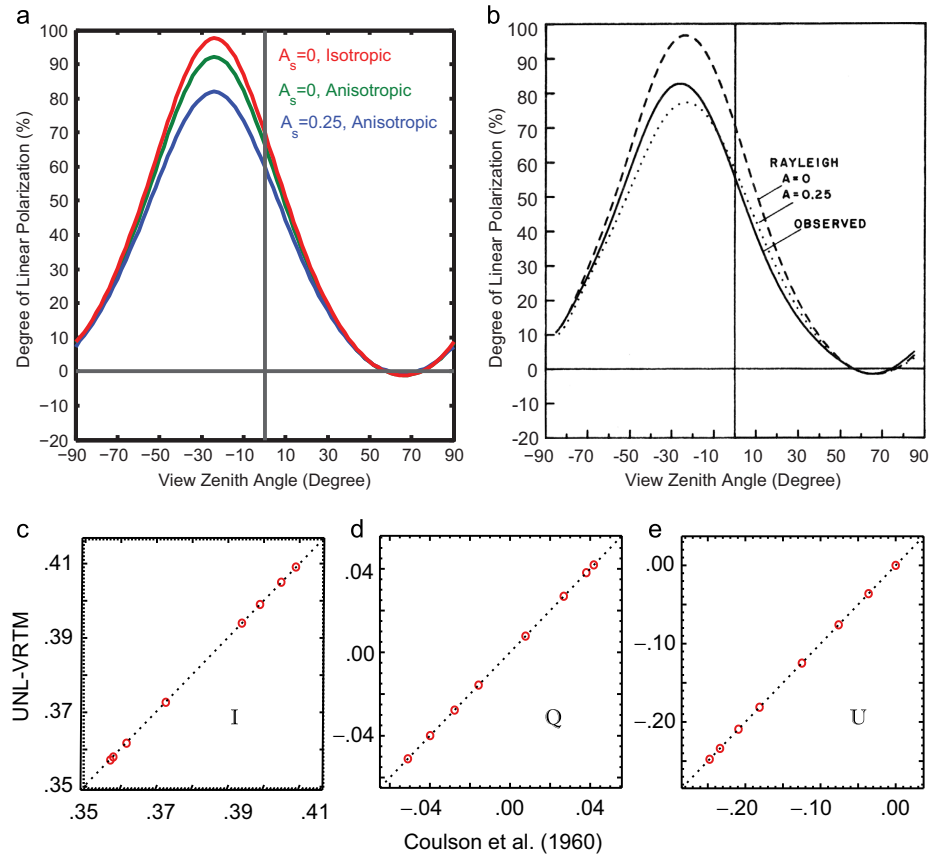


Figure 2.3: Degree of linear polarization ( $-Q/I$ ) of downward radiation for a pure Rayleigh atmosphere: (a) computed by UNL-VRM for the case analyzed in Figure 5.7 of [Coulson \[1988\]](#) and shown here as (b). (c)–(e) shows the comparisons of  $I$ ,  $Q$ , and  $U$  computed by [Coulson et al. \[1960\]](#) and those from UNL-VRM. In (a) and (b),  $A_s$  represents the surface albedo value. In (c) and (d), the calculation is for  $\tau = 1.0$ , surface albedo is 0.25,  $\cos \theta_0 = 0.8$ , and for 8 different viewing angles. (Figure adopted from [Wang et al. \[2014\]](#).)

the retrieval of AOD in urban regions, it is critical to treat absorption by  $\text{SO}_2$  and  $\text{NO}_2$ . In contrast, calculations performed at moderate spectral resolution (such as those from Santa Barbara Discrete-Ordinate Atmospheric Radiative Transfer, or SBDART [[Ricchiuzzi et al., 1998](#)], shown as the blue lines in Figure 2.2b and c) do not resolve fine-structure details, sometimes missing the absorption lines for  $\text{SO}_2$  or  $\text{NO}_2$ , and in general producing significant underestimation of optical depths in the  $\text{O}_2\text{A}$  band.

Figure 2.3 shows the calculation of the degree of linear polarization (DOLP) of downward

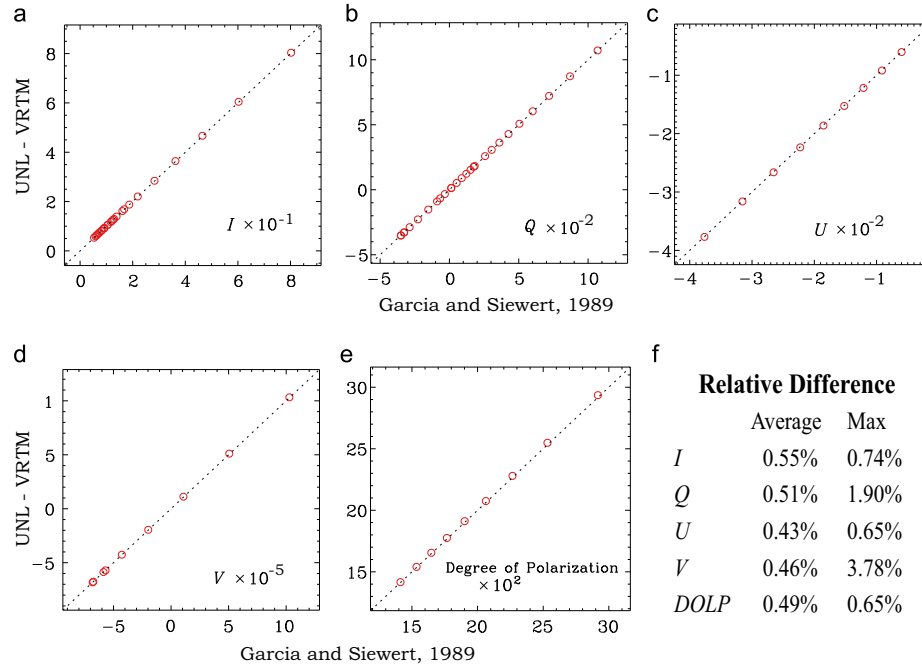


Figure 2.4: Counterparts in Tables 3–10 of *Garcia and Siewert* [1989] for upwelling radiation on the top of the same atmospheric conditions of aerosol scattering. No gas absorption and Rayleigh scattering are considered. Note that compared here are  $I$  and  $Q$  values reported in *Garcia and Siewert* [1989] for 9 view angles (with cosine values from 0.1 to 0.9 at equal spacing of 0.1) and 3 relative azimuth angles ( $0$ ,  $\pi/2$ , and  $\pi$ ), which yields a total of 27 data points. For  $U$  and  $V$ , their values are reported for the same 9 viewing angles but for one relative azimuth angle ( $\pi/2$ ) only. The calculation is performed at wavelength of 951 nm and  $\tau$  of 1.0, and aerosol size distribution parameters  $r_{\text{eff}} = 0.2$ ,  $v_{\text{eff}} = 0.07$ , refractive index  $m_r = 1.44$ , and SSA of 0.99. (Figure adopted from *Wang et al.* [2014].)

radiation in a pure Rayleigh scattering atmosphere. The solid blue line in Figure 2.3a (dotted line in Figure 2.3b) reproduces the theoretical results shown in Figure 5.7 of *Coulson* [1988], which was used to interpret the DOLP measured at Mauna Loa Observatory on February 19, 1977. Furthermore, Figure 2.3a shows that the anisotropy in Rayleigh scattering reduces the peak DOLP by 5% (e.g., the difference between the green and red lines) at  $0.7 \mu\text{m}$ . Surface reflection and its concomitant increase of atmosphere scattering will decrease the DOLP of downward radiation. An increase of surface reflectance from 0 to 0.25 decreases the peak DOLP by 10%.

Quantitatively, the Stokes-vector  $I$ ,  $Q$ , and  $U$  components computed with UNL-VRM differ from their counterparts found in the tables by *Coulson et al.* [1960] by average (relative) deviations of  $1.9 \times 10^{-4}$  (0.05%),  $2 \times 10^{-5}$  (0.14%), and  $4 \times 10^{-5}$  (0.03%), respectively (Figure 2.3c–e). These differences are similar to the values  $2.1 \times 10^{-4}$ ,  $9 \times 10^{-5}$ , and  $4 \times 10^{-5}$  identified by *Evans and Stephens* [1991]. More recently, Rayleigh-atmosphere benchmark results have been re-computed by *Vijay and Hovenier* [2012] to a much higher degree of accuracy; this work also included benchmarking of the VLIDORT model.

Figure 2.4 shows benchmark calculations of four Stokes parameters for radiative transfer in an aerosol-only atmosphere. *Garcia and Siewert* [1989] documented their results for unpolarized incident radiation at 951 nm and  $\cos\Theta_0$  of 0.2, for an atmosphere with a Lambertian reflectance of 0.1. The aerosols in that atmosphere were assumed to satisfy a gamma-function size distribution with  $r_{\text{eff}}$  of  $0.2 \mu\text{m}$  and  $v_{\text{eff}}$  of 0.07, and a refractive index yielding an aerosol single scattering albedo of 0.99. Compared to their results, the Stokes parameters computed by UNL-VRM show relative differences of less than 0.6%, with maximum relative differences (at certain viewing geometries) of up to 2% for  $Q$  and 3.8% for  $V$ . The DOLP computed from the UNL-VRM (with 15 streams for the hemisphere) and documented by *Garcia and Siewert* [1989] (with 3 streams) differ on average by 0.5%, with a maximum relative difference of 0.65%.

The simultaneous calculation of analytic Jacobians of the four Stokes parameters with respect to the aerosol optical depth, size parameters, refractive indices, and aerosol-loading peak height for both fine and coarse model aerosols may be validated against Jacobians calculated using the finite difference method (Figures 2.5 and 2.6). Overall, results from the two methods are highly correlated as seen in the scatter plots shown in these figures. Relative differences in all comparisons are less than 0.5%, and in many cases the differences are less than 0.05%.

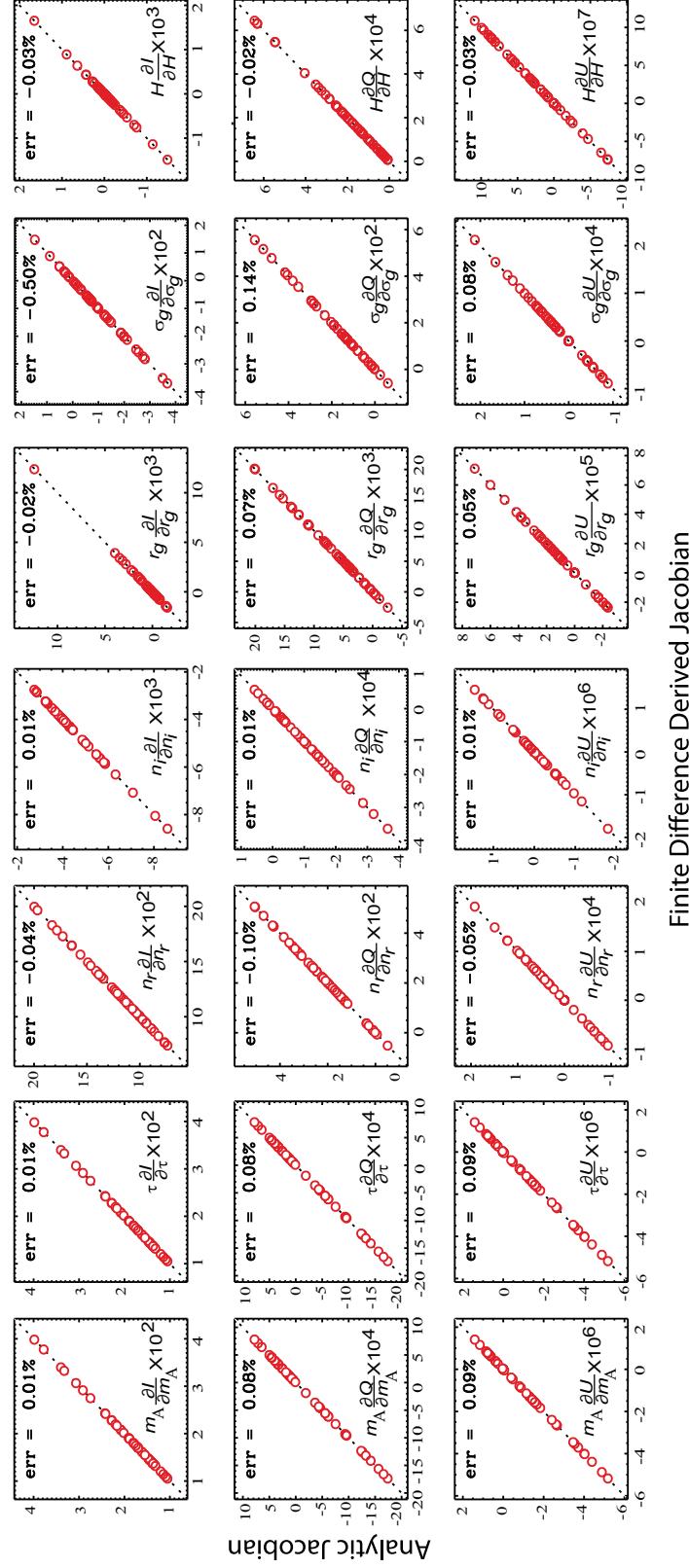


Figure 2.5: Intercomparison of Jacobians ( $\partial \xi / \partial \ln x$ ) calculated with UNL-VRM using the analytical method (y-axis) with those computed from UNL-VRM using finite-difference estimates (x-axis). Here  $\xi$  is one of the Stokes parameters:  $I$  (top row),  $Q$  (middle row), and  $U$  (last row).  $x$  is one of 7 parameters associated with fine-mode aerosols: mass concentration  $m_A$ ,  $\tau_A$ ,  $m_r$ ,  $m_i$ ,  $r_g$  and  $\sigma_g$  (of the lognormal PSD), and height ( $H$ ) of peak aerosol concentration in the vertical. Note, the calculation is done for an atmosphere containing both fine- and coarse-mode aerosols as described in [Hess et al. \[1998\]](#). (Figure adopted from [Wang et al. \[2014\]](#).)

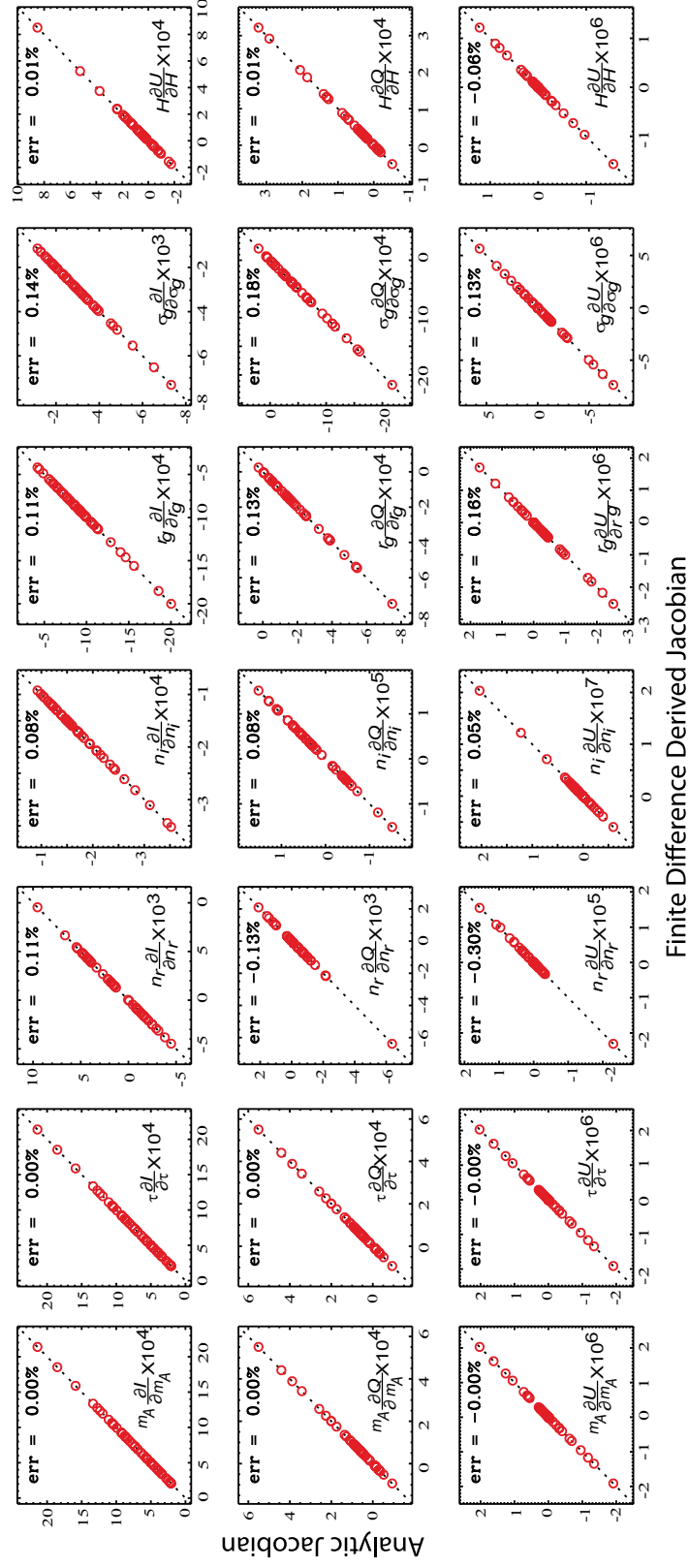


Figure 2.6: Same as in Fig. 5, but for coarse mode aerosols. (Figure adopted from Wang *et al.* [2014])

## CHAPTER 3

### INVERSION THEORIES AND ALGORITHM

#### 3.1 Introduction

The inverse problem of this work seeks the solution of a number of microphysical parameters from observations of different categories. We thus need to develop an retrieval algorithm that uses statistically optimized multi-variable fitting, in which the solution is sought not only rely on the preassumed classes of potential solutions, but also in a continuous space of solutions under statistically formulated criteria optimizing the error distribution of the retrieval parameters. In this chapter, I first present the general theory of inverse problem (section 3.2), covering the Bayesian-based inversion (section 3.2.1) and information content analysis (3.2.2). After that in section 3.3, I describe the key aspects of designed inversion algorithm: the definition of the state vector (section 3.3.1) and considered constraining its *a priori* and smoothness feature (section 3.3.2), how the state vector is sought statistically (section 3.3.3), how the retrieval error is characterized (section 3.3.4), and quality control of measurements (section 3.3.5).

## 3.2 Inversion Theories

### 3.2.1 Maximum a posteriori solution of an inverse problem

Let  $\mathbf{x}$  denote a state vector that contains  $n$  parameters to be retrieved (such as PSD parameters and complex indices of refraction), and  $\mathbf{y}$  an observation vector with  $m$  elements of measurements (such as multi-band radiances from different viewing angles). Furthermore, let  $\mathbf{F}$  indicate a forward model (such as the radiative transfer model) that describes the physics on how  $\mathbf{y}$  and  $\mathbf{x}$  are related. Then, we have

$$\mathbf{y} = \mathbf{F}(\mathbf{x}, \mathbf{b}) + \boldsymbol{\varepsilon}_y \quad (3.1)$$

where the vector  $\mathbf{b}$  consists of forward model parameters (such as the surface reflectance) that are not included in  $\mathbf{x}$  but quantitatively influence the measurement to our known, the  $\boldsymbol{\varepsilon}_y$  term is the error that results from inaccurate modeling and measurement processes. In this study, we use the best-estimated  $\hat{\mathbf{b}}$  in the forward model and consider its contributions to the total measurement accuracy. Linearize the forward model at  $\mathbf{b} = \hat{\mathbf{b}}$ :

$$\mathbf{y} = \mathbf{F}(\mathbf{x}, \hat{\mathbf{b}}) + \hat{\mathbf{K}}_b + \boldsymbol{\varepsilon}_y \quad (3.2)$$

where  $\hat{\mathbf{K}}_b$  is the weighting function (or Jacobian matrix) of forward model to model parameters  $\mathbf{b}$  at  $\hat{\mathbf{b}}$ ,  $\left. \frac{\partial \mathbf{F}}{\partial \mathbf{b}} \right|_{\mathbf{b}=\hat{\mathbf{b}}}$ . If we treat the forward model as linear in the vicinity of the true state of  $\mathbf{x}$ , the forward model can be rewritten as:

$$\mathbf{y} = \mathbf{K}\mathbf{x} + \boldsymbol{\varepsilon} \quad (3.3)$$



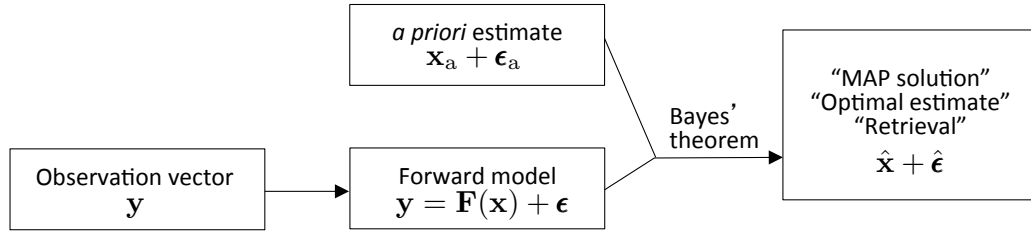


Figure 3.1: The concept of an inverse problem that optimizing an estimates from observations. (Courtesy: Daniel Jacobs)

Where  $\boldsymbol{\epsilon}$  represents the error that sums the errors from forward modeling and measurement processes. We only consider the errors propagated from errors in  $\mathbf{b}$ , but omit any other source in the forward modeling. Thus,  $\boldsymbol{\epsilon} = \boldsymbol{\epsilon}_y + \hat{\mathbf{K}}_b \boldsymbol{\epsilon}_b$ , where  $\boldsymbol{\epsilon}_b = \mathbf{b} - \hat{\mathbf{b}}$  indicates error of  $\hat{\mathbf{b}}$ .  $\mathbf{K}$  is the  $m \times n$  Jacobian matrix comprising derivatives of the forward model with respect to each retrieved parameter,  $\frac{\partial \mathbf{F}}{\partial \mathbf{x}}$ .

The inverse problem is to solve  $\mathbf{x}$  from the measurement  $\mathbf{y}$  by inverting the forward model  $\mathbf{F}$ . In many situations, the forward model is a complex process with large number of internal uncertainties. As a result, the inverse problem tends to be an ill-posed problem. In this regard, the *a priori* constraints are usually considered. *A priori* represents the knowledge of the state before the measurement is made. And the true state occurs nearby the *a priori*:

$$\mathbf{x} = \mathbf{x}_a + \boldsymbol{\epsilon}_a. \quad (3.4)$$

where  $\mathbf{x}_a$  is the *a priori estimate* and  $\boldsymbol{\epsilon}_a$  indicates *a priori* error.

Then, the inverse problem becomes to solve the equation set (as illustrated in Figure 3.1):

$$\begin{cases} \mathbf{y} = \mathbf{K}\mathbf{x} + \boldsymbol{\epsilon} \\ \mathbf{x} = \mathbf{x}_a + \boldsymbol{\epsilon}_a. \end{cases} \quad (3.5)$$

Provided that errors of measurements and the *a priori* are characterized by a Gaussian

probability distribution function (PDF) and the forward model is linear in the vicinity of the true state, the maximum a posteriori (MAP) solution of the state vector, also called the retrieval or the a posteriori, can be derived with the Bayes's Theorem [Rodgers, 2000]:

$$\hat{\mathbf{x}} = \mathbf{x}_a + (\mathbf{K}^T \mathbf{S}_y^{-1} \mathbf{K} + \mathbf{S}_a^{-1})^{-1} \mathbf{K}^T \mathbf{S}_y^{-1} (\mathbf{y} - \mathbf{K} \mathbf{x}_a) \quad (3.6)$$

Here,  $\mathbf{S}_a$  is the error covariance matrix of *a priori*,  $\mathbf{x}_a$ ;  $\mathbf{S}_y$  is the error covariance matrix of the measurements;  $T$  denote matrix transpose operation.

The "retrieval",  $\hat{\mathbf{x}}$ , in above equation (3.6) is corresponding to the maximum posterior PDF and the minimum of a cost function defined by

$$J = (\mathbf{y} - \mathbf{K} \mathbf{x})^T \mathbf{S}_y^{-1} (\mathbf{y} - \mathbf{K} \mathbf{x}) + (\mathbf{x} - \mathbf{x}_a)^T \mathbf{S}_a^{-1} (\mathbf{x} - \mathbf{x}_a). \quad (3.7)$$

$J$  is indeed the negative exponent term of the posterior PDF, which also follows a Gaussian shape with the expected value of  $\hat{\mathbf{x}}$  and the error covariance matrix  $\hat{\mathbf{S}}$  given by

$$\hat{\mathbf{S}}^{-1} = \mathbf{K}^T \mathbf{S}_y^{-1} \mathbf{K} + \mathbf{S}_a^{-1}. \quad (3.8)$$

$\hat{\mathbf{S}}$  describes the statistical uncertainties in retrieved  $\hat{\mathbf{x}}$  due to measurement noise, forward modeling uncertainty, and smoothing error [Rodgers, 2000]. The square roots of its diagonals are the one-sigma uncertainties of each retrieved parameters given the observation uncertainties, forward model uncertainties, and prior knowledge of the state. With  $\hat{\mathbf{S}}$ , we can also estimate the uncertainty for any parameter (for example, the aerosol single scattering albedo in this study) that can be fully determined by parameters (for example, aerosol refractive index and PSD parameters) in  $\mathbf{x}$  but is not directly retrieved. If one parameter is a

function defined by  $\zeta = \text{zetax}$ , then the uncertainty in derived  $\zeta$  is [Rodgers, 2000]:

$$\hat{\epsilon}_{\zeta} = \sqrt{\sum_{i=1}^n \sum_{j=1}^n \frac{\partial \zeta}{\partial x_i} \frac{\partial \zeta}{\partial x_j}}. \quad (3.9)$$

### 3.2.2 Information theory

The Jacobian matrix  $\mathbf{K}$  usually serves as gradients in the sensitivity analysis and can be a useful indicator of information. For a linear system in the absence of measurement error, the rank of  $\mathbf{K}$  indicates independent pieces of information that can be determined from the measurements. In practice, error inevitably presents in measurements and thus can impact the effective rank. To identify the effective sensitivity of individual measurement to each retrieved parameter, we define the error-normalized (EN) Jacobian matrix by

$$\tilde{\mathbf{K}} = \mathbf{S}_y^{-\frac{1}{2}} \mathbf{K} \mathbf{S}_a^{\frac{1}{2}} \quad (3.10)$$

$\tilde{\mathbf{K}}$  is also called the ‘pre-whitening’ by Rodgers [2000]. The superiority of the matrix  $\tilde{\mathbf{K}}$  over the matrix  $\mathbf{K}$  is that it compares the observation error covariance ( $\mathbf{S}_y^{\frac{1}{2}}$ ) with the natural variability of the observation vector as expressed by its prior covariance ( $\mathbf{K} \mathbf{S}_a^{\frac{1}{2}}$ ). Any component whose natural variability is smaller than the observation error is not measurable. Therefore, an element  $\tilde{\mathbf{K}}_{i,j}$  less than unity indicates that the measurement component  $y_i$  contains null useful information for determining parameter  $x_j$ . In contrast, when  $\tilde{\mathbf{K}}_{i,j} > 1$ , the larger of its value, the more useful information retained in  $y_i$  for determining  $x_j$ . Therefore, the  $\tilde{\mathbf{K}}$  matrix provides not only sensitivity of individual measurements to each retrieved parameter, but also a capacity-metric for those observations to infer retrieved parameters.

The averaging kernel matrix has been widely used to quantify the information gained by making a measurement [e.g., Rodgers, 1998; Hasekamp and Landgraf, 2005a; Frankenberg

*et al.*, 2012; Sanghavi *et al.*, 2012]. It provides the sensitivity of the retrieval to the true state and is defined by

$$\mathbf{A} = \frac{\partial \hat{\mathbf{x}}}{\partial \mathbf{x}}. \quad (3.11)$$

Replace  $y$  in equation (3.6) with equation (3.3) at  $\mathbf{x} = \mathbf{x}_a$ ,

$$\hat{\mathbf{x}} = \mathbf{x}_a + (\mathbf{K}^T \mathbf{S}_y^{-1} \mathbf{K} + \mathbf{S}_a^{-1})^{-1} \mathbf{K}^T \mathbf{S}_y^{-1} [\mathbf{K}(\mathbf{x} - \mathbf{x}_a) + \boldsymbol{\varepsilon}] \quad (3.12)$$

Then we have

$$\mathbf{A} = \frac{\partial \hat{\mathbf{x}}}{\partial \mathbf{x}} = (\mathbf{K}^T \mathbf{S}_y^{-1} \mathbf{K} + \mathbf{S}_a^{-1})^{-1} \mathbf{K}^T \mathbf{S}_y^{-1} \mathbf{K} \quad (3.13)$$

Matrix  $\mathbf{A}$  quantifies the ability of the retrieval to infer  $\hat{\mathbf{x}}$  given the relationship between  $\mathbf{y}$  and  $\mathbf{x}$  (i.e.,  $\mathbf{K}$ ) and given the observation noise and a priori characterization. Thus, an identity matrix of  $\mathbf{A}$  represents a perfect retrieval, while a null matrix of  $\mathbf{A}$  indicates that none of the information can be gained from the observation. The trace of  $\mathbf{A}$  is the degree of freedom for signal, i.e.,  $\text{DFS} = \text{Trace}(\mathbf{A})$ , which represents independent pieces of information that the observation can provide. The diagonal elements of averaging kernel matrix  $\mathbf{A}$ , or the DFS components, indicate the partial sensitivity of each individual retrieved parameters with respect to their corresponding truth:

$$\mathbf{A}_{i,i} = \frac{\partial \hat{x}_i}{\partial x_i} \quad (3.14)$$

Clearly,  $\mathbf{A}_{i,i} = 1$  indicates that the observation is capable of fully characterizing the truth of  $x_i$ ; while  $\mathbf{A}_{i,i} = 0$  indicates the observation contains zero information on  $x_i$  and  $x_i$  is not measurable. From the formulation of  $\hat{\mathbf{S}}$  and  $\mathbf{A}$ , we can conclude that only the error covariance and Jacobian matrix, but not the retrieval, are important for the purpose of understanding information content.

Other quantities used for information analysis of a measurement include the Shannon information content (SIC) [Shannon, 1948] and the Fisher information matrix. SIC, a widely used quantity [e.g., Rodgers, 1998; Knobelspiesse *et al.*, 2012], is defined as the reduction in entropy after the measurement

$$H = \frac{1}{2} \ln |\mathbf{S}_a| - \frac{1}{2} \ln |\hat{\mathbf{S}}| = -\frac{1}{2} \ln |\hat{\mathbf{S}} \mathbf{S}_a^{-1}| = -\frac{1}{2} \ln |\mathbf{I}_n - \mathbf{A}| \quad (3.15)$$

where  $\mathbf{I}_n$  is an identity matrix of order  $n$ . Clearly, SIC is highly related to the DFS for the information analysis. In the Gaussian linear case, the Fisher information matrix is equal to the inverse of *a posteriori* error covariance matrix,  $\hat{\mathbf{S}}^{-1}$ . The retrieval indeed corresponds to the maximum of *a posteriori* PDF and the minimum of retrieval error. It is thus straightforward that higher level of the Fisher information is subject to a smaller retrieval error. Due to their close relationship with the DFS and  $\hat{\mathbf{S}}$ , we will not present the SIC and Fisher information analysis in this study.

### 3.3 New Research Algorithm for AERONET Inversion

Figure 3.2 gives an overview of the retrieval algorithm specifically designed for the analysis and inversion of photo-polarimetric remote sensing observations, such as those from AERONET. The algorithm builds upon the UNified and Linearized Vector Radiative Transfer Model (UNL-VRTM), which consists of seven component modules for the forward simulation of observations (section 2.2). The forward modeling includes the linearized vector radiative transfer model (VLIDORT) developed by Spurr [2006], a linearized Mie code and a linearized T-Matrix code calculating aerosol single scattering properties [Spurr *et al.*, 2012], a module calculating Rayleigh scattering and a module for gas absorption, plus a surface model computing bidirectional reflectance/polarization distribution function

(BRDF/BPDF) [Spurr, 2004]. The required input parameters for the algorithm are the relevant atmospheric profiles (of pressure, temperature, and gaseous mixing ratio), aerosol loading in terms of AOD or aerosol columnar volume, aerosol vertical profiles, aerosol microphysical and chemical parameters (size distribution and complex refractive index), and surface reflection parameters. The users can specify up to two modes of the aerosol population. Each mode is characterized by the total particle number (or volume), the vertical profile, size distribution, and refractive index. The aerosol-related modules—Mie, T-matrix, and VLIDORT—are analytically linearized and fully coupled. Thus, the forward model not only simulates radiance and/or polarization for a given spectrum, but also simultaneously computes the Jacobians of these radiation fields with respect to input aerosol microphysical parameters. Our inversion-oriented UNL-VRTM supplies these Jacobians together with observation error characterizations and *a priori* constraints to the statistical optimization procedure for the retrieval. Objective information content (section 3.2.2) and error analysis (section 3.2.1) are also included in the procedure along with the inversion. Although our algorithm is tailored to measurements from the AERONET SunPhotometer, its modularized framework enables the simulation and inversion of observations from various platforms, including satellite sensors.

Development of the inversion component in our algorithm was built upon our experience with optimization of aerosol emissions using the adjoint chemistry transport model (CTM) [Wang *et al.*, 2012; Xu *et al.*, 2013]. In essence, the optimization method is consistent with the adjoint modeling that constrains aerosol emissions from measurements through inverting a CTM, although different physical processes are involved for inversion of AERONET observation. Both inversions seek the optimal solutions for a state vector that minimizes the differences between the model simulation and observation. In addition, our algorithm inherits the inversion strategy from the Dubovik00&06 algorithm, in particular with regard to the smoothness constraint on the spectral dependence of the complex refractive index.

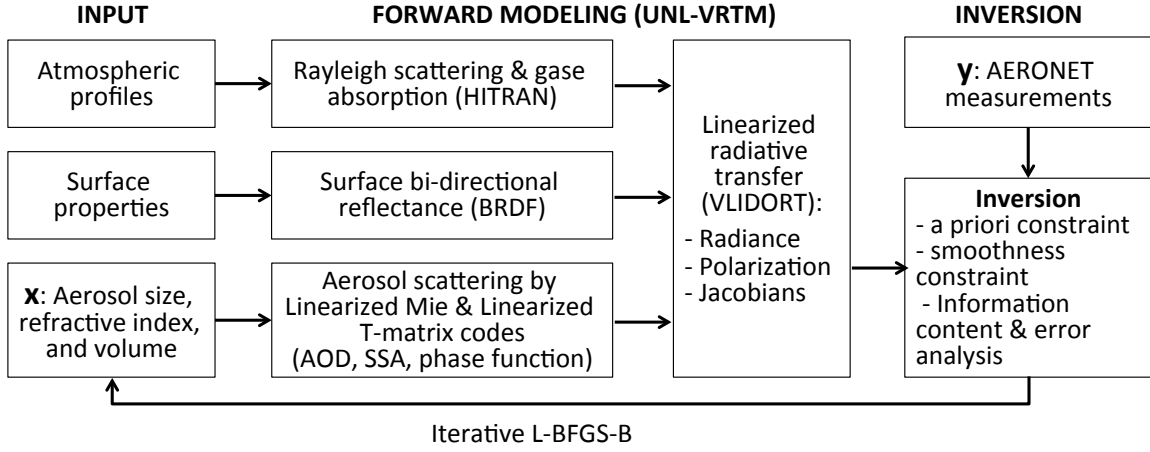


Figure 3.2: General structure of the new research inversion algorithm for the retrieval of aerosol microphysical parameters from AERONET photo-polarimetric measurements.

Table 3.1: AERONET observation characteristics.

Symbol	Parameter	Instrumental uncertainty	Other uncertainties
$y_1$	Direct sun AOD	0.01–0.02	$\sim 0.02$ spatial/temporal variation
$y_2$	Sky radiance in solar almucantar	5%	Surface BRDF and BPDF
$y_3$	Sky radiance in principal plane	5%	Surface BRDF and BPDF
$y_4$	DOLP in principal plane	0.01	Surface BRDF and BPDF

### 3.3.1 Definition of state vector and observation vector

For this study, the observation vector  $y$  comprises components from different sources. As listed in Table 3.1 (and Table 1.1 for specific measurements by the SunPhotometer), there are four categories of observations, i.e., the direct sun AOD, the sky radiance around the solar aureole, the sky radiance in the solar principal plane, and the DOLP in the solar principal plane, with all measurements performed at 440, 675, 870, and 1020 nm. Also indicated in Table 3.1 are the calibration errors and other measurement uncertainties that make of the term  $\epsilon$ .

The state vector  $x$  contains 11 pairs of parameters characterizing aerosol properties in the fine and the coarse modes, respectively, the columnar volume concentration  $V_0$ , the effective

radius  $r_{\text{eff}}$ , the effective variance  $v_{\text{eff}}$ , and the complex refractive index  $m_r - m_i i$  at 440, 675, 870, and 1020 nm (Table 3.2).  $r_{\text{eff}}$  and  $v_{\text{eff}}$  are two commonly used size parameters in the aerosol radiative quantification, because different types of size distribution function having same values of  $r_{\text{eff}}$  and  $v_{\text{eff}}$  possess similar scattering and absorption properties [Hansen and Travis, 1974]. In line with many studies [Schuster *et al.*, 2006; Hasekamp and Landgraf, 2005a, 2007; Mishchenko *et al.*, 2007; Waquet *et al.*, 2009], we assume the aerosol PSD follows a bi-modal lognormal function expressed in equation (2.10). All parameters include both the fine and coarse modes and account for a total of 22 elements ( $n = 22$ ).

### 3.3.2 Combine a priori and smoothness constraints

*A priori* information describes our knowledge of the state vector before measurements are applied, and an *a priori* constraint is commonly used to achieve a well-defined stable and physically reasonable solution to an ill-posed problem. Usually, a priori knowledge comprises both a mean state  $\mathbf{x}_a$  and its error  $\boldsymbol{\epsilon}_a$  (equation (3.4)). One of the satisfactory sources for the *a priori* knowledge is a climatology based on historical measurements. For a given AERONET site, we use the available inversion products that have been obtained with the Dubovik00&06 algorithm, for which the *a priori* can be well characterized by the mean values and standard deviations of each component in the state vector. At the same time, the *a priori* can also be determined from other sources if historical AERONET retrieval is not available. For example, we could extract aerosol microphysical climatology from chemistry transport model simulations [e.g., Wang *et al.*, 2010] or from measurements of in situ and/or even satellite sensors.

Among those retrieved parameters, the aerosol volumes— $V_0^f$  and  $V_0^c$ —are the most variable or uncertain quantities. A reasonable initial guess for these quantities could speed up the iterative inversion. Here, we “look up” their initial values from the AOD measurements at



Table 3.2: State vector elements and associated constraints for inversion.<sup>a</sup>

Symbol	Parameter	<i>a priori</i> constraint?	Smoothness constraint?
$V_0^f, V_0^c$	Columnar volume ( $\mu\text{m}^3\mu\text{m}^{-2}$ )	✓	
$r_{\text{eff}}^f, r_{\text{eff}}^c$	Effective radiance ( $\mu\text{m}$ )	✓	
$v_{\text{eff}}^f, v_{\text{eff}}^c$	Effective variance	✓	
$\mathbf{m}_r^f, \mathbf{m}_r^c$	Real part refractive index	✓	✓
$\mathbf{m}_i^f, \mathbf{m}_i^c$	Imaginary part refractive index	✓	✓

<sup>a</sup>The superscripts, 'c' and 'f', respectively denote fine and coarse aerosol modes. Refractive indices are for spectral wavelengths of 440, 675, 870, and 1020 nm.

two spectral wavelengths. Given the *a priori* information on the aerosol PSD and refractive indices, the aerosol extinction efficiency  $Q_{\text{ext}}$  can be obtained for each fine and coarse mode with the Mie code. And the AOD is related to the  $V_0^f$  and  $V_0^c$  via equation:

$$\tau_A = \tau_A^f + \tau_A^c = \frac{3V_0^f Q_{\text{ext}}^f}{4r_{\text{eff}}^f} + \frac{3V_0^c Q_{\text{ext}}^c}{4r_{\text{eff}}^c}. \quad (3.16)$$

Clearly, applying the above equation to the AODs at any two spectral wavelengths, we can easily solve  $V_0^f$  and  $V_0^c$ .

For some parameters, the *a priori* estimates may be poorly known, but these parameters behave smoothly with no sharp oscillations. For example, the aerosol refractive index usually does not vary rapidly over the visible to near-infrared spectral range. In this regard, a smoothness constraint could be a preferable addition. The technique of constraining a smooth solution was pioneered by [Phillips \[1962\]](#); [Twomey \[1963\]](#), and has been successfully used to retrieve coherent aerosol size distributions [[Dubovik and King, 2000](#)] and atmospheric vertical profiles [[Twomey, 1977](#)]. The principle of the smoothness constraint is to restrain the degree of non-linearity of a certain physical parameter by limiting the values of its dth derivatives:

$$\mathbf{G}_d + \boldsymbol{\varepsilon}_\Delta = \mathbf{0} \quad (3.17)$$

where  $\mathbf{G}_d$  is a differential matrix composed of coefficients for calculating the  $d$ th derivatives of  $\mathbf{x}$  with respect to the dependent variable, and the vector  $\boldsymbol{\epsilon}_\Delta$  indicates uncertainties in these derivatives.

In particular, for constraining the dependence of the spectral refractive index with wavelength, the matrix  $\mathbf{G}_d$  calculates the  $d$ th difference of the refractive index at four wavelengths (440, 675, 870, and 1020 nm). As discussed by [Dubovik and King \[2000\]](#), we assume a linear relationship between the logarithm of the refractive index and the logarithm of the wavelength:  $m_r \sim \lambda^{-\alpha}$ , and  $m_i \sim \lambda^{-\beta}$ . Further, the matrix  $\mathbf{G}_1$  for the first difference (of either  $m_r$  or  $m_i$  of one mode) can be expressed as:

$$\begin{aligned} \mathbf{G}_1 &= \begin{bmatrix} 1/\Delta\lambda_1 & 0 & 0 \\ 0 & 1/\Delta\lambda_2 & 0 \\ 0 & 0 & 1/\Delta\lambda_3 \end{bmatrix} \begin{bmatrix} -1 & 1 & 0 & 0 \\ 0 & -1 & 1 & 0 \\ 0 & 0 & -1 & 1 \end{bmatrix} \\ &= \begin{bmatrix} -1/\Delta\lambda_1 & 1/\Delta\lambda_1 & 0 & 0 \\ 0 & -1/\Delta\lambda_2 & 1/\Delta\lambda_2 & 0 \\ 0 & 0 & -1/\Delta\lambda_3 & 1/\Delta\lambda_3 \end{bmatrix} \end{aligned} \quad (3.18)$$

Here,  $\Delta\lambda_1$ ,  $\Delta\lambda_2$ , and  $\Delta\lambda_3$  are the denominators for the first-order differences in the logarithm, e.g.,  $\Delta\lambda_1 = \ln \frac{675}{440}$ . As to  $\boldsymbol{\epsilon}_\Delta$ , we assume errors in first differences of the refractive index following [Dubovik and King \[2000\]](#), i.e., 0.2 for  $m_r$  and 1.5 for  $m_i$ .

Similar to the approach suggested by [Dubovik and King \[2000\]](#), we use multiple *a priori* constraints in the retrieval. Specifically, we combine the *a priori* constraint of equation (3.4) and the smoothness constraint of equation (3.17); our inverse problem is equivalent to

solving the following set of three equations (in contrast to (3.5) that has two equations):

$$\begin{cases} \mathbf{y} = \mathbf{F}(\mathbf{x}) + \boldsymbol{\varepsilon} \\ \mathbf{x} = \mathbf{x}_a + \boldsymbol{\varepsilon}_a \\ \mathbf{0} = \mathbf{G}_d + \boldsymbol{\varepsilon}_\Delta. \end{cases} \quad (3.19)$$

### 3.3.3 Statistical optimized inversion

Under the assumption of Gaussian-distributed errors, the optimized solution of equation (3.19) according to the MAP method corresponds to the state vector that minimizes the quadratic cost function consisting of multiple terms [Dubovik and King, 2000; Dubovik, 2004]:

$$J(\mathbf{x}) = \boldsymbol{\gamma}_y [\mathbf{y} - \mathbf{F}(\mathbf{x})]^T \mathbf{S}_y^{-1} [\mathbf{y} - \mathbf{F}(\mathbf{x})] + \boldsymbol{\gamma}_a (\mathbf{x} - \mathbf{x}_a)^T \mathbf{S}_a^{-1} (\mathbf{x} - \mathbf{x}_a) + \boldsymbol{\gamma}_\Delta \mathbf{x}^T \boldsymbol{\Omega} \mathbf{x}. \quad (3.20)$$

where  $\boldsymbol{\Omega}$  is a smoothing matrix related to  $\mathbf{G}_d$  and the error covariance matrix  $\mathbf{S}_\Delta$  (of the  $d$ th derivatives of  $\mathbf{x}$ ) by  $\boldsymbol{\Omega} = \mathbf{G}_d^T \mathbf{S}_\Delta^{-1} \mathbf{G}_d$ . The vectors  $\boldsymbol{\gamma}_y$ ,  $\boldsymbol{\gamma}_a$ , and  $\boldsymbol{\gamma}_\Delta$  are regularization parameters. In principle, the minimization of three-term cost function given by the equation (3.20) is conceptually analogous to the minimization of bi-component cost functions (3.7) generally considered in the Bayesian approach [Rodgers, 2000]. These three terms on the right-hand side of equation (3.20) represent, respectively, (1) the total squared fitting error incurred owing to departures of the model predictions from the observations, (2) the penalty error incurred owing to departures of the estimates from the a priori, and (3) the penalty error incurred owing to departures from the defined smoothness feature. Overall, the minimization of  $J(\mathbf{x})$  achieves the objective of improving the agreement between the model and the measurements while ensuring that the solution remains within a reasonable

range and degree of smoothness.

The regularization parameters in the calculation of  $J(\mathbf{x})$  act as weights to balance the fitting error and the penalty errors. Clearly, a good assignment of  $\boldsymbol{\gamma}$  is of crucial importance for the statistical optimal solution. High values of  $\boldsymbol{\gamma}_a$  and  $\boldsymbol{\gamma}_\Delta$  can lead to over-smoothing of the solution with little improvement to the fitting residuals, while low values minimize the error term at the cost of greatly increasing the parameter penalty terms. Optimal values of  $\boldsymbol{\gamma}$  for two-term cost functions can be identified at the corner near the origin of the so-called L-curve [Hansen, 1998]. However, such approach is not appropriate to the multi-term cost function. In this study, we assume equal weights for observational constraint term and combined *a priori* constrain terms in the cost function:

$$\boldsymbol{\gamma}_a = \frac{1}{2}n^{-1}\mathbf{e}, \quad \boldsymbol{\gamma}_\Delta = \frac{1}{2}(n_\Delta - d)^{-1}\mathbf{e}, \quad \boldsymbol{\gamma}_y = \left\langle \frac{1}{4m_k} \right\rangle_{k=1,4} \quad (3.21)$$

Here,  $d$  is the order of difference,  $\mathbf{e}$  is a vector consisting of  $n$  elements of 1, and  $n_\Delta$  is the number of state elements that are supplied with smoothness constraints. Values for  $\boldsymbol{\gamma}_y$  are chosen to control the fitting residuals for observations of four different categories as listed in Table 3.1. Each group comprises the number of  $m_k$  observations for  $k$  from 1 to 4. The corresponding elements of  $\boldsymbol{\gamma}_y$  for the  $k$ th group are  $\frac{1}{4m_k}$ , which means the observation quadratic term is normalized by the observation count of each group.

In principle, solving this inverse problem is tantamount to a pure mathematical minimization procedure. The minimization of  $J(\mathbf{x})$  equation (3.20) is performed with an iterative quasi-Newton optimization approach using the L-BFGS-B algorithm [Byrd et al., 1995; Zhu et al., 1994], which offers bounded minimization to ensure the solution stays within a physically reasonable range. The L-BFGS-B algorithm requires knowledge of  $\mathbf{x}_a$  and  $J(\mathbf{x})$ , as well as the gradient of  $J(\mathbf{x})$  with respect to  $\mathbf{x}$ , or  $\nabla_{\mathbf{x}}J$ . By linearizing the forward model

$F(\mathbf{x})$ , we can determine  $\nabla_{\mathbf{x}}J$  by

$$\nabla_{\mathbf{x}}J(\mathbf{x}) = \boldsymbol{\gamma}_y \mathbf{K}^T \mathbf{S}_y^{-1} [\mathbf{y} - \mathbf{F}(\mathbf{x})] + \boldsymbol{\gamma}_a \mathbf{S}_a^{-1} (\mathbf{x} - \mathbf{x}_a) + \boldsymbol{\gamma}_\Delta \boldsymbol{\Omega} \mathbf{x}. \quad (3.22)$$

Here, the Jacobian matrix  $\mathbf{K}$  is computed analytically by the UNL-VRTM (section 2.2) through equations (2.15) and (2.16). At each iteration, improved estimates of the state vector are implemented and the forward simulation is recalculated. The convergence criterion to determine the optimal solution is the smallness of the reduction of  $J(\mathbf{x})$  and the norm of  $\nabla_{\mathbf{x}}J(\mathbf{x})$ . The iteration stops when the reduction of  $J(\mathbf{x})$  is less than 1% within 10 continuous iterations. Then, the optimal solutions are identified corresponding to the smallest norm of  $\nabla_{\mathbf{x}}J(\mathbf{x})$  from these 10 last iterations. In addition, to ensure a physically reasonable solution, we also perform retrieval error analysis, and impose a practical quality control on real measurements.

### 3.3.4 Characterizing retrieval error

The retrieval without error characterization is of significantly lesser value. Once the retrieval is achieved, the retrieval error can be characterized by the *a posteriori* state, and the error analysis can be performed in terms of a linearization of the problem around the solution  $\hat{\mathbf{x}}$ . We estimate the retrieval error on each state vector element using the error covariance matrix of the *a posteriori* state:

$$\hat{\mathbf{S}}^{-1} = \hat{\mathbf{K}}^T \mathbf{S}_y^{-1} \hat{\mathbf{K}} + \mathbf{S}_a^{-1} + \boldsymbol{\Omega}. \quad (3.23)$$

where  $\hat{\mathbf{K}}$  is the Jacobian matrix of the forward model  $\mathbf{F}(\mathbf{x})$  at the solution  $\hat{\mathbf{x}}$ . It should be noted that the above three-term *a posteriori* formularized according to the three-term cost function defined in the equation (3.20). Simply, the retrieval error for each element can be

estimated by:

$$\hat{\epsilon}_i = \hat{\mathbf{S}}_{i,i}^{\frac{1}{2}} \quad (3.24)$$

With  $\hat{\mathbf{S}}$  applied to equation (3.9), we can also estimate the uncertainty in parameters (such as  $\omega_A$  and asymmetry factor in this study) that can be fully determined by the parameters in  $\mathbf{x}$  but are not themselves directly retrieved.

### 3.3.5 Quality control of measurements

We apply a suite of quality criteria to ensure (a) a cloud-free condition, (b) that aerosol particles are quasi-homogeneously distributed in the horizontal plane within the scanning region, and (c) the measurements are densely populated and cover a wide range of scattering angles so that they provide sufficient information to retrieve all parameters falling within specified uncertainty levels. More specifically, these criteria are as follows: (i) the number of AOD observations  $\geq 2$  within a  $\pm 25$ -minute centered at the period of a full scan sequence; (ii) sky radiance observations are excluded when the scattering angle is less than  $3.2^\circ$  and DOLP observations are excluded when the scattering angle is smaller than  $5^\circ$ ; (iii) a symmetry check for the almucantar radiances: the difference is less than 5% for the azimuthal angle of  $180^\circ$  and less than 10% elsewhere; and (iv) principal-plane observations are discarded when their second derivatives with respect to the scattering angle are beyond smoothing threshold. Although most of these criteria follow [Holben et al. \[2006\]](#), we also check the smoothness of the principal-plane radiances and DOLP to identify scans that are contaminated by cloud. We apply the threshold on the second derivative of radiance (or DOLP) with respect to scattering angle in order to restrain local oscillations of radiance (or DOLP) caused by clouds or heterogeneous aerosol plumes. Thus, applying such a threshold can effectively remove sharp kinks and ensure continuous quantities in the principal-plane scanning sequences. Indeed, this smoothness check share the same principle to the smoothness constraint presented in

the section [3.3.2](#).

## CHAPTER 4

### INFORMATION CONTENT ANALYSIS

#### 4.1 Introduction

The AERONET collects not only the multi-spectral and multi-angular radiance observations, but also the state of light polarization from various viewing angles over many sites (section 1.1.2). Unfortunately, the potential of AERONET polarization measurements in retrieving aerosol microphysical parameters has not been fully exploited. Polarization measurements contain valuable information about aerosol microphysical properties [*Mishchenko and Travis, 1997; Cairns et al., 1997*], as the polarization of light is highly sensitive to the aerosol size and refractive index [*Hansen and Travis, 1974*]. Several studies have emphasized the usefulness of the polarimetric observations taken by the ground-based instruments [*Cairns et al., 1997; Boesche et al., 2006; Emde et al., 2010; Zeng et al., 2008*]. *Vermeulen et al. [2000]* presented a two-step method to retrieve aerosol microphysical properties from polarized radiances: first, the single scattering albedo and the natural and polarized phase functions were retrieved from transmission and almucantar radiances and polarization in the principal plane; second, the aerosol PSD and refractive index were then derived. With the current AERONET inversion algorithm, *Dubovik et al. [2006]* conducted a case study using polarization data in a UAE<sup>2</sup> (Unified Aerosol Experiment-United Arab Emirates) field campaign [*Reid et al., 2008*]. *Li et al. [2009]* extended the inversion algorithm of *Dubovik et al. [2006]* to include multi-spectral polarization and demonstrated improved retrievals in



real part aerosol refractive index for fine particles and the fraction of spherical particles.

However, questions regarding the use of AERONET polarimetric observations for retrieving aerosol microphysical parameters remain unresolved: (1) Practically, do the existing AERONET photo-polarimetric measurements have any potential to improve the retrieval of aerosol information content that we now routinely obtain from radiance measurement only? and (2) Hypothetically, how can future upgrades of AERONET photo-polarimetric measurements and inversion algorithm maximize the retrieval information content of aerosols? Answering these two questions is not only relevant to the future AERONET instrumentation design, but also for the ground-based passive polarimetric remote sensing of aerosols in general.

In this chapter, we seek to answer above questions from a theoretical perspective (section 3.2.2) by investigating the available information contained in the AERONET measurements with and without the inclusion of polarization data. This investigation is to provide the a theoretical foundation to support actual algorithm development for using polarimetric data for aerosol retrievals. The structure of this chapter is as follows. In section 4.2, we describe the experimental design on the aerosol models, error characteristics of *a priori* and AERONET measurements. Section 4.3 presents the results of information content and error analysis. In section 4.4, we investigate the sensitivity of retrieval uncertainties in aerosol parameters with respect to the aerosol loading and fine/coarse aerosol characteristics.

Table 4.1: The aerosol parameters defined for both fine and coarse aerosol modes<sup>a</sup>.

Mode	$r_{\text{eff}}(\mu\text{m})$	$v_{\text{eff}}$	$\mathbf{m}_r$	$\mathbf{m}_i$	$\omega_A$
Fine	0.21 (80%)	.25 (80%)	1.44, 1.44, 1.43, 1.42 (.15)	.009, .011, .012, .011 (.01)	.95, .93, .92, .91
Coarse	1.90 (80%)	.41 (80%)	1.56, 1.55, 1.54, 1.54 (.15)	.004, .003, .003, .002 (.005)	.84, .91, .93, .96

<sup>a</sup>The complex refractive index  $\mathbf{m}_r - \mathbf{m}_i i$ , and single scattering albedo  $\omega_A$  are reported at 440, 675, 870, and 1020 nm. Bracketed values are assumed a priori error in relative for  $r_{\text{eff}}$  and  $v_{\text{eff}}$  and in absolute for  $\mathbf{m}_r$ ,  $\mathbf{m}_i$ , and  $\omega_A$ .

Finally, we summarize in section 4.5 the general findings of this study and implications for practical algorithm development.

## 4.2 Experimental Design

### 4.2.1 *a priori* characteristics

The state vector  $\mathbf{x}$  comprises 22 (11 pairs) retrieved parameters, namely, the columnar volume concentration  $V_0$ , the effective radius  $r_{\text{eff}}$ , the effective variance  $v_{\text{eff}}$ , and the complex refractive index  $m_r + m_i i$  at 440, 675, 870, and 1020 nm (section 3.3.1). These 11 pairs of parameters characterizing aerosol properties in the both fine and coarse aerosol modes; each mode follows a lognormal PSD function. Table 4.1 displays aerosol size parameters, refractive indices, and single scattering albedo for each size mode adopted for error and information analysis; also showed in brackets are their associated *a priori* uncertainties. The fine-mode particles are corresponding to water-soluble aerosols obtained from OPAC database [Hess *et al.*, 1998] with updates by Drury *et al.* [2010], while the coarse-mode is preassembly for large spherical particles with refractive index from Patterson *et al.* [1977]; Wagner *et al.* [2012].

In order to include various atmospheric conditions, we simulate three types of aerosols—each with different relative percentage between the coarse and fine modes—(I) fine particles

Table 4.2: The aerosol scenarios adapted for numerical experiments<sup>a</sup>.

Aerosol type	$V_0$	$\text{fmf}_v$	$\tau_A$	$\text{fmf}_\tau$	AE	$\omega_A$
Fine-dominated	.15	.8	1.0, .58, .36, .25	.97, .95, .92, .88	1.5	.95, .93, .92, .91
Well-mixed	.22	.5	1.0, .61, .41, .32	.90, .83, .74, .65	1.3	.94, .93, .92, .93
Coarse-dominated	.43	.2	1.0, .71, .57, .50	.69, .55, .42, .32	.82	.91, .92, .92, .94

<sup>a</sup>Values for  $\tau_A$ ,  $\omega_A$ , and  $\text{fmf}_\tau$  are listed respectively for spectral wavelength of 440, 675, 870, and 1020 nm. The AE is reported between 440 and 870 nm.  $V_0$  is in the unit of  $\mu\text{m}^3 \mu\text{m}^{-2}$

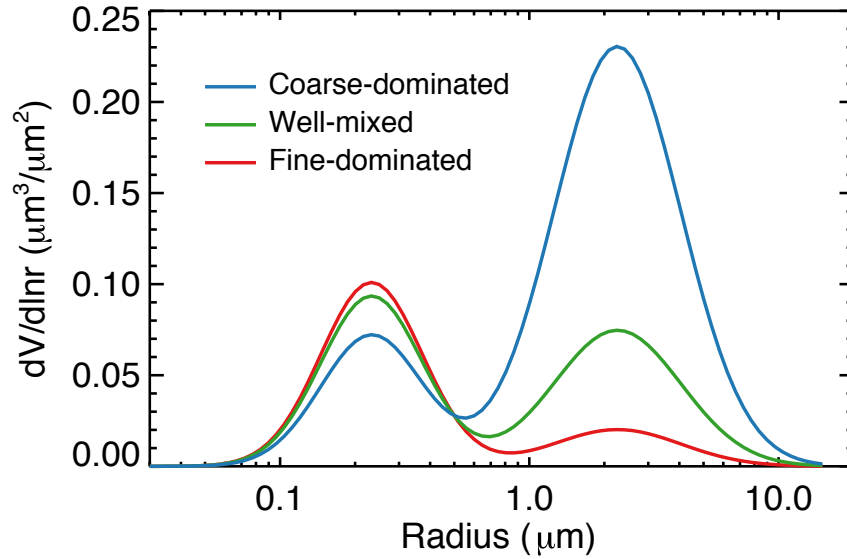


Figure 4.1: Volume size distribution for the aerosol types adopted for the information analysis. Relevant aerosol parameters are summarized in the Tables 4.1 and 4.2.

dominated, (II) well mixed, and (III) coarse particles dominated. As listed in Table 4.2 and illustrated in Figure 4.1, fine-mode fractions in terms of volume ( $\text{fmf}_v$ ) are defined as 0.8, 0.5, and 0.2 for these three types, respectively. Aerosol volumes are scaled as necessary to maintain a normalized AOD at 440 nm corresponding to a moderate hazy condition ( $\tau_{440} = 1.0$ ). The spectral aerosol optical depths  $\tau_A$ , single scattering albedo  $\omega_A$ , and the Ångström exponent (AE) are calculated and also shown in Table 4.2.

#### 4.2.2 Synthetic observations

As described in section 1.1.2 and Table 1.1, The SunPhotometer equipped at AERONET sites routinely measures direct and diffuse (sky) solar radiances and optionally the mono-band light polarization [Holben *et al.*, 1998]. Recently, multi-spectral polarizations have also been taken with a newer-generation SunPhotometer (CIMEL CE318-DP) at some sites [Li *et al.*, 2009] and the UAE<sup>2</sup> fields campaign Reid *et al.* [2008]. Here we focus our study on using multi-spectral polarizations for the inversion of aerosol parameters.

Table 4.3: List of scenarios of AERONET observations used for information content analysis.

Scenario	Observations included <sup>a</sup>	Remark
I1	$\tau_A$ , and $I_{alm}$	Observations used in Dubovik00&06 algorithm
I2	$\tau_A$ , $I_{alm}$ , and $I_{pp}$	Scenario I1 plus principal-plane radiances
P1	$\tau_A$ , $I_{alm}$ , $I_{pp}$ and $DOLP_{pp}$	Scenario I2 plus principal-plane polarization
P2	$\tau_A$ , $I_{alm}$ , and $DOLP_{alm}$	Scenario I1 plus almucantar polarization

<sup>a</sup>Variables are for four spectral wavelengths, i.e., 440, 675, 870, and 1020 nm.

In order to investigate the merit of synergizing various observations in the inversion, we define four different scenarios of observation vectors, i.e., I1, I2, P1, and P2 as summarized in the Table 1. The observation vector in scenario I1 comprises direct sun AODs and solar almucantar radiances ( $I_{alm}$ ) at 440, 675, 870, and 1020 nm. Scenario I2 includes measurements in scenario A and the total radiances ( $I_{pp}$ ) at the same four wavelengths observed in the solar principal-plane. Observations in scenario P1 are defined to further include  $DOLP_{pp}$  at those four wavelengths. Lastly, scenario P2 observations comprise basic measurements in scenario I1 plus almucantar polarization ( $DOLP_{alm}$ ) at same wavelengths. The  $DOLP_{alm}$  is not routinely measured by any current SunPhotometer, but we include it for a comparative analysis. Measurements defined in scenario I1 represent observations used by the current AERONET operational inversion and thus serves as a control experiment. From scenario I2, we can investigate the synergy of radiances in both the solar almucantar and solar principal-plane. Scans in the solar principal-plane can achieve larger scattering angles and thus may contain additional scattering information. And with scenarios P1 and P2 we will be able to evaluate the potential of adding polarization in the inversion.

We exclude  $I_{ppl}$  (Table 1.1) in our analysis because sky radiance in the solar principal plane can be also obtained during the polarization scan ( $I_{pp}$ ).  $I_{ppl}$  and  $I_{pp}$  are different in the viewing-angle sequences, but they generally share a similar range of scattering angles. Thus, one is redundant for the other. We also exclude analysis for monochromatic polarization (at 870 nm) current measured on many AERONET sites, because single-band polarization

measurements contain much less information than multi-band ones and newer generation SunPhotometers with multi-band polarization capacity will be deployed at more AERONET sites.

## 4.3 Results

Following the approach stated in section 3.2, we have simulated the AERONET photopolarimetric measurements under various solar zenith angles from  $40^\circ$  to  $75^\circ$  for the three defined aerosol types (Table 4.2). The simulated radiances ( $I_{\text{alm}}$ ) on the solar almucantar plane and the degree of linear polarization ( $\text{DOLP}_{\text{pp}}$ ) on the solar principal plane are illustrated in Figure 4.2 for aerosols of type II with solar zenith angle of  $55^\circ$ . These simulations for other aerosol types and other solar zenith angles are of similar pattern. According to Figure 4.2a,  $I_{\text{alm}}$  decreases as the scattering angle increases, resulting from forward-dominated scattering phase function of aerosol particles. The maximum  $\text{DOLP}_{\text{pp}}$  takes place at the scattering angle of  $90^\circ$  as a result of composite effect of Rayleigh and aerosol scattering, while the smaller  $\text{DOLP}_{\text{pp}}$  values dominates at the small scattering angles because of the predominance of diffracted light (Figure 4.2b). With the synthetic data and relevant error characterizations, we have computed the EN Jacobian matrix, DFS, and a posteriori error to evaluate the capacity of AERONET measurements in inferring aerosol microphysical properties. Our analysis mainly focuses on the comparison of those quantities between measurements with and without including polarization, so that we can understand the importance of adding polarization for the retrieval.

### 4.3.1 Error-normalized (EN) Jacobian matrix

We compare the EN Jacobians for the  $I_{\text{alm}}$  and  $\text{DOLP}_{\text{pp}}$  in both Figure 4.3 and Figure 4.4 to disclose the importance of  $\text{DOLP}_{\text{pp}}$  measurements to the retrieval. Distinct patterns of

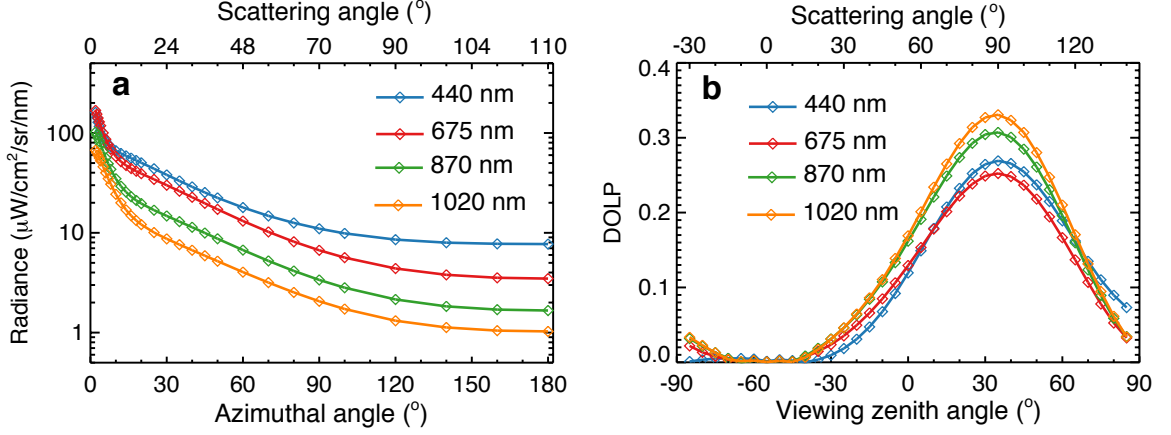


Figure 4.2: (a) Simulated radiances in the solar almucantar plane as a function of azimuth angle. (b) Simulated degree of linear polarization (DOLP) in the solar principal plane as a function of view zenith angle. Simulations are for the well-mixed aerosol type with columnar AOD of 1.0 at 440 nm as shown in the Table 4.2. Solar zenith angle is  $55^\circ$  and top abscissas show corresponding scattering angles.

EN Jacobians can be found between the  $\text{DOLP}_{\text{pp}}$  and  $I_{\text{alm}}$  over the scattering angle. As shown in Figures 4.3a and 4.4a, the radiance at scattering angles less than  $\sim 10^\circ$  decreases with increasing fine-mode aerosol loading (e.g. negative  $\partial I_{\text{alm}}/\partial V_0$ ) and increases with increasing coarse-mode aerosol loading (e.g. positive  $\partial I_{\text{alm}}/\partial V_0$ ), whereas the sensitivity of the  $I_{\text{alm}}$  to  $V_0$  at larger scattering angles is larger positive in the fine mode and less positive in the coarse mode. It is because large particles scatter more radiation than small particles at near-forward scattering angles [van de Hulst, 1981]. In contrast, the  $\text{DOLP}_{\text{pp}}$  presents profound sensitivity to the  $V_0$  of aerosol in both modes at the scattering angles between  $45^\circ$  and  $135^\circ$  (Figures 4.3f and 4.4f).

Furthermore, the EN Jacobians of  $I_{\text{alm}}$  and  $\text{DOLP}_{\text{pp}}$  can also be synergized in terms of their variations on the spectral wavelength. For example, the EN Jacobians for  $I_{\text{alm}}$  with respect to the fine-mode  $V_0$  express lowest at 440 nm (blue curve in Figure 4.3a), but those for  $\text{DOLP}_{\text{pp}}$  at 440 nm (blue curve in Figure 4.3f) are largest ones among these four spectral bands. Indeed, variations of these sensitivities with wavelength are mainly determined by

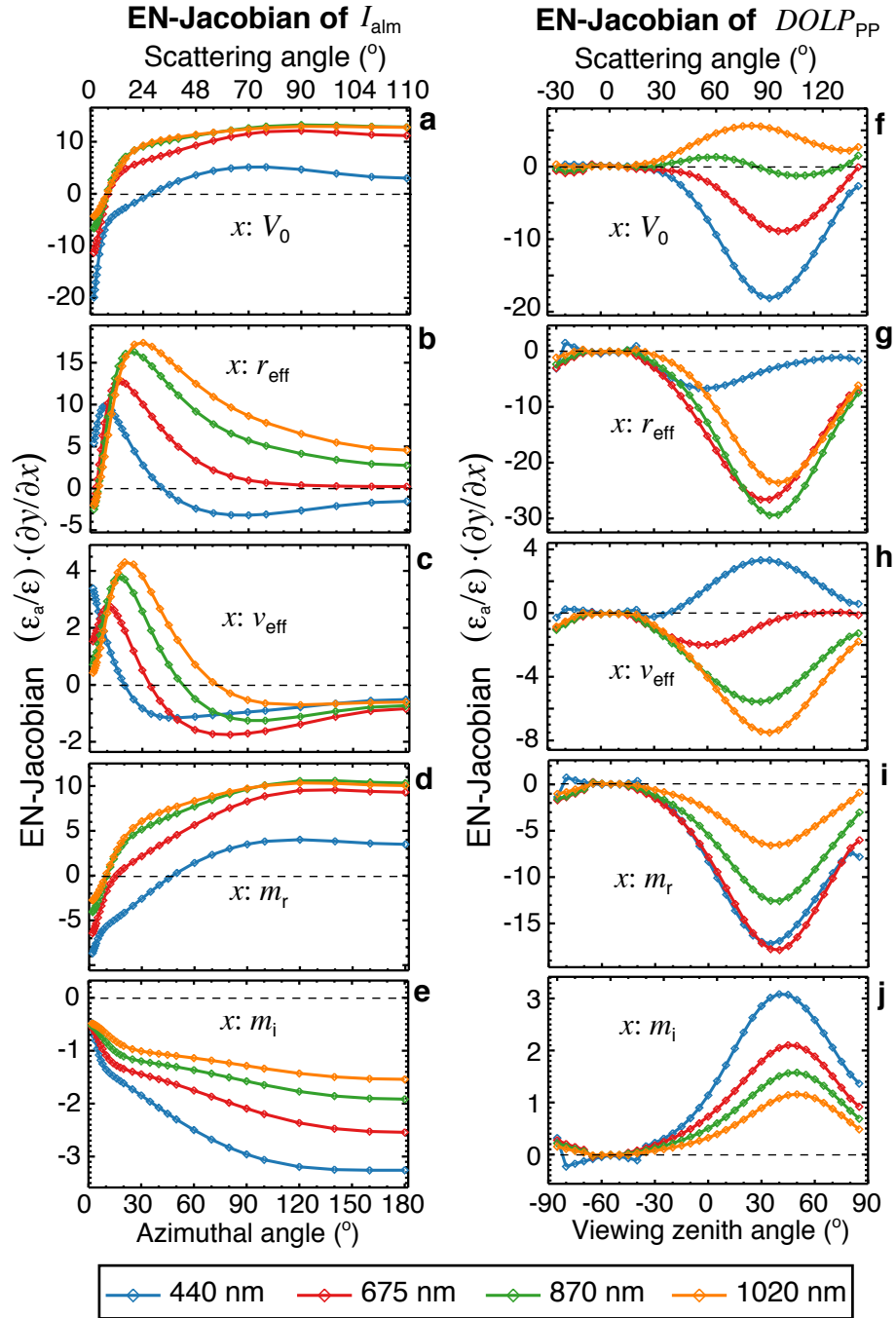


Figure 4.3: Error-normalized Jacobians of almucantar radiances  $I_{\text{alm}}$  (left column) and degree of linear polarization  $DOLP_{\text{pp}}$  (right column) with respect to retrieved aerosol parameters in the *fine* mode: (a, f)  $V_0$ , (b, g)  $r_{\text{eff}}$ , (c, h)  $v_{\text{eff}}$ , (d, i)  $m_r$ , and (e, j)  $m_i$ . Simulations use type-II aerosols with columnar AOD of 1.0 at 440 nm and solar zenith angle of  $55^\circ$ . The top and bottom abscissas are respectively the scattering angle and SunPhotometer scanning geometries.

Figure 4.4: Same as Figure 4.3 but for parameters of aerosol in the *coarse* mode.



the change of size parameter  $\eta$ , which defined as the ratio of the particle size to the applied spectral wavelength,  $\eta = 2\pi r_{\text{eff}}/\lambda$ . The  $\text{DOLP}_{\text{pp}}$  in scattering angles near  $90^\circ$  approaches unity under pure Rayleigh scattering regime where  $\eta \ll 1$ . When the  $\eta$  increases, the value of  $\partial \text{DOLP}_{\text{pp}}/\partial V_0$  decreases and transits into negative at  $\eta \sim 2$ , reaches negative maxima at  $\eta \sim 10$ , then increases and slowly transits back to positive when  $\eta$  is as large as  $\sim 40$  [Hansen and Travis, 1974]. The magnitude of the  $\eta$  at these four bands ranges from 3.0 to 1.3 for the fine-mode particles and from 27 to 11 for the coarse-mode particles. Therefore we can understand that: (i) the sensitivity of  $\text{DOLP}_{\text{pp}}$  to the fine-mode  $V_0$  is positive at 1020 nm due to the small size parameter  $\eta = 1.3$  (orange curve in Figure 4.3f); (ii) this sensitivity gets weaker at 675 nm to 870 nm and transits to negative at 440 nm as  $\eta$  increases (Figure 4.3f); and (iii) this sensitivity for aerosol in the coarse mode is more negative for longer wavelengths that are corresponding to smaller values of  $\eta$ .

We also note that sensitivity of the  $I_{\text{alm}}$  to PSD parameters dominates for scattering angles less than  $\sim 40^\circ$  (Figures 4.3b-c and 4.4b-c), while its sensitivity to  $m_r$  and  $m_i$  prevails at larger scattering angles (Figures 4.3d-e and 4.4d-e). In the near-forward scattering angular regions, the dominant scattering effect is the diffraction of light, which essentially depends on the size of particles and is independent of the index of refraction [van de Hulst, 1981; Hansen and Travis, 1974]. The  $\text{DOLP}_{\text{pp}}$ , in contrast, is sensitive to both the aerosol size and the refractive index at scattering angles from  $45^\circ$  to  $135^\circ$  (right columns of the Figures 4.3 and 4.4). Variations of the sensitivity among spectral bands can be explained by the wavelength-dependent size parameters as discussed in the above paragraph.

Overall, the  $\text{DOLP}_{\text{pp}}$  EN Jacobians have similar or larger magnitudes to these of  $I_{\text{alm}}$ , indicating that the  $\text{DOLP}_{\text{pp}}$  measurements possess equal or larger information for the inversion of these aerosol properties. Adding such complementary  $\text{DOLP}_{\text{pp}}$  measurements to the current radiance-only inversion can potentially increase the retrieval accuracy. The magnitude of EN Jacobian elements varies among retrieved parameters, which leads to the

variability of retrieval accuracy. The EN Jacobians with respect to the  $V_0$  and  $r_{\text{eff}}$  of both modes and the fine-mode  $v_{\text{eff}}$  and refractive index are larger than those of other parameters. Correspondingly, these parameters are expected to achieve higher accuracy in the retrieval. While the maxima in EN Jacobians of  $I_{\text{alm}}$  with respect to the coarse-mode refractive index at 870 and 1020 nm slightly excess unity (Figure 4.4d-e), larger counterparts for  $\text{DOLP}_{\text{pp}}$  (Figure 4.4i-j) will likely result in improved retrievals. In contrast, magnitudes of EN Jacobian for both  $I_{\text{alm}}$  and  $\text{DOLP}_{\text{pp}}$  with respect to coarse-mode refractive index at 440 and 675 nm are smaller than unity across the whole angular range. Adding polarization may not improve the retrieval for coarse-mode refractive index at those shorter wavelengths in such aerosol scenario. However, the consideration of spectral dependence of refractive index by using the smoothness constraints will potentially resolve this problem [Dubovik, 2004].

### 4.3.2 Information content and retrieval error

We calculated the averaging kernel matrix  $\mathbf{A}$ , DFS, and *a posteriori* error for retrieved parameters from these four scenarios of observation defined in Table 4.3. Figures 4.5a-c illustrate how the DFS varies with the solar zenith angles for three defined aerosol types. The DFS in the scenario I2 (red curves) ranges from 14 to 15 for the fine-dominated aerosol model, and from 17 to 19 for other two aerosol models, about 2–3 degrees higher than those using AODs and  $I_{\text{alm}}$  measurements in the scenario I1 (black curves), indicating that sky radiances in the principal plane ( $I_{\text{pp}}$ ) contain additional information. The scenario P1 (green curves), which comprises solar almucantar sky radiances and principal-plane polarimetric radiances at four wavelengths, further increases DFS by 1–2. Observations in the scenario P2 (blue curves)—radiance and polarization in the almucantar plane—yields DFS values slightly below those in the scenarios I2 and P1. Therefore, from Figure 4.5 we conclude that adding measurements in the solar principal plane into the inversion significantly increases the

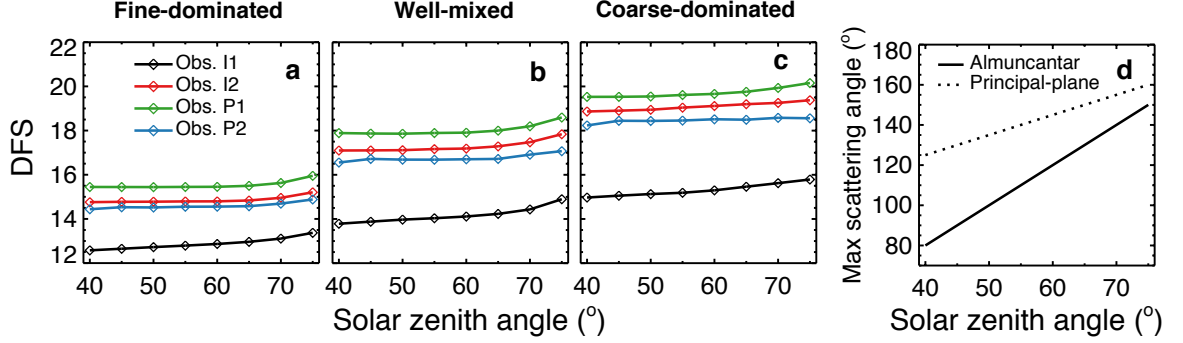


Figure 4.5: Degree of freedom for signal (DFS) as a function of solar zenith angle for retrieving all 22 parameters when using aerosol type of (a) fine-dominated, (b) well-mixed, and (c) coarse-dominated. Four differently colored-curves denote four observation scenarios defined in Table 1. Panel (d) shows the maximum scattering angles that can be reached by the almucantar and the principal-plane scans.

information content for aerosol properties, especially when combining the  $I_{pp}$  and  $DOLP_{pp}$ . We also note that the DFS increases with solar zenith angle for all cases. Observations in larger solar zenith angle enable a wider range of scattering angles (Figure 4.5d), and thus contain more information on the aerosol scattering phase function and in turn on the aerosol microphysical parameters.

We illustrate the DFS components  $A_{i,i}$  in Figure 4.6 for the  $V_0$ ,  $r_{eff}$  and  $v_{eff}$ , and in Figure 4.7 and 4.8 for the  $m_r$  and  $m_i$ , respectively. Also shown in those figures are the a posteriori errors, which are the diagonal elements of  $\hat{\mathbf{S}}^{\frac{1}{2}}$ . It should be noted that errors for  $V_0$ ,  $r_{eff}$ , and  $v_{eff}$  are in terms of relative uncertainties (%), while errors in the  $m_r$  and  $m_i$  are absolute quantities. Curves of four different colors in each panel indicate these defined four observation scenarios and are averages for the three aerosol types. Error bars represent one fifth of the standard deviations among the three aerosol types (the use of the one-fifth scale is only for plotting purpose). These error bars thus depict the variability of the DFS component and retrieval error over the fine-mode fraction ( $fmf_v$ ). Mean retrieval uncertainties averaged over various solar zenith angles are summarized in Table 4.4. We discuss these results for each retrieved parameter in detail as following.

#### 4.3.2.1 Aerosol PSD

Among the 22 elements in the state vector, the  $V_0$ ,  $r_{\text{eff}}$  and  $v_{\text{eff}}$  describe the aerosol PSD. According to Figure 4.6a-c, observations in the scenario P1 (green curves) always yield the highest DFS components for inferring PSD parameters in both the fine and coarse modes, followed by observations from the scenarios I2 (red) and P2 (blue), and lastly the scenario I1 (black). As a consequence, the *a posteriori* errors are found smallest for the scenario P1 and largest for the scenario I1 (Figure 4.6d-e). Retrieval errors in the scenario I1 (black curves) are 5–15% for  $V_0$ , 5–9% for  $r_{\text{eff}}$ , and 20–30% for  $v_{\text{eff}}$ , which vary with solar zenith angles. In contrast, retrieval errors in the scenario P1 (green curves) are reduced to  $\sim 2.5\%$  (3%), 1% (3.5%), and 7% (20%) for the fine (coarse) mode. From observations in the scenarios P2 and I2, one can retrieve  $V_0$ ,  $r_{\text{eff}}$ , and  $v_{\text{eff}}$  of errors lying between the scenarios I1 and P1, though slightly larger in the scenario P2. In addition, higher DFS components and smaller retrieval errors are found for the fine-mode parameters than those for the coarse mode, because radiances and polarization are in particular more sensitive to aerosol parameters in the fine mode as shown in the contrast between the Figures 4.3 and 4.4

We also note that, in the scenario I1, DFS components for the coarse-mode parameters decrease with increasing solar zenith angle, while no obvious trend can be found for the fine-mode parameters. This can be explained by the low sensitivity of the  $I_{\text{alm}}$  to the coarse-mode  $V_0$ ,  $r_{\text{eff}}$ , and  $v_{\text{eff}}$  at large scattering angles as showed in Figure 4.4a-c. Higher sensitivities occur at scattering angles below  $\sim 30^\circ$ ; the increase in SZA results in a smaller number of measurements in the near-forward scattering angular regions, and thus leads to larger retrieval errors. However, these trends turn to be weaker or negligible in other observation scenarios, especially the scenario P1. We can understand this from two aspects. First, observations from principal plane can add additional measurements near the forward scattering region. Second and most importantly, the added polarization measurements in

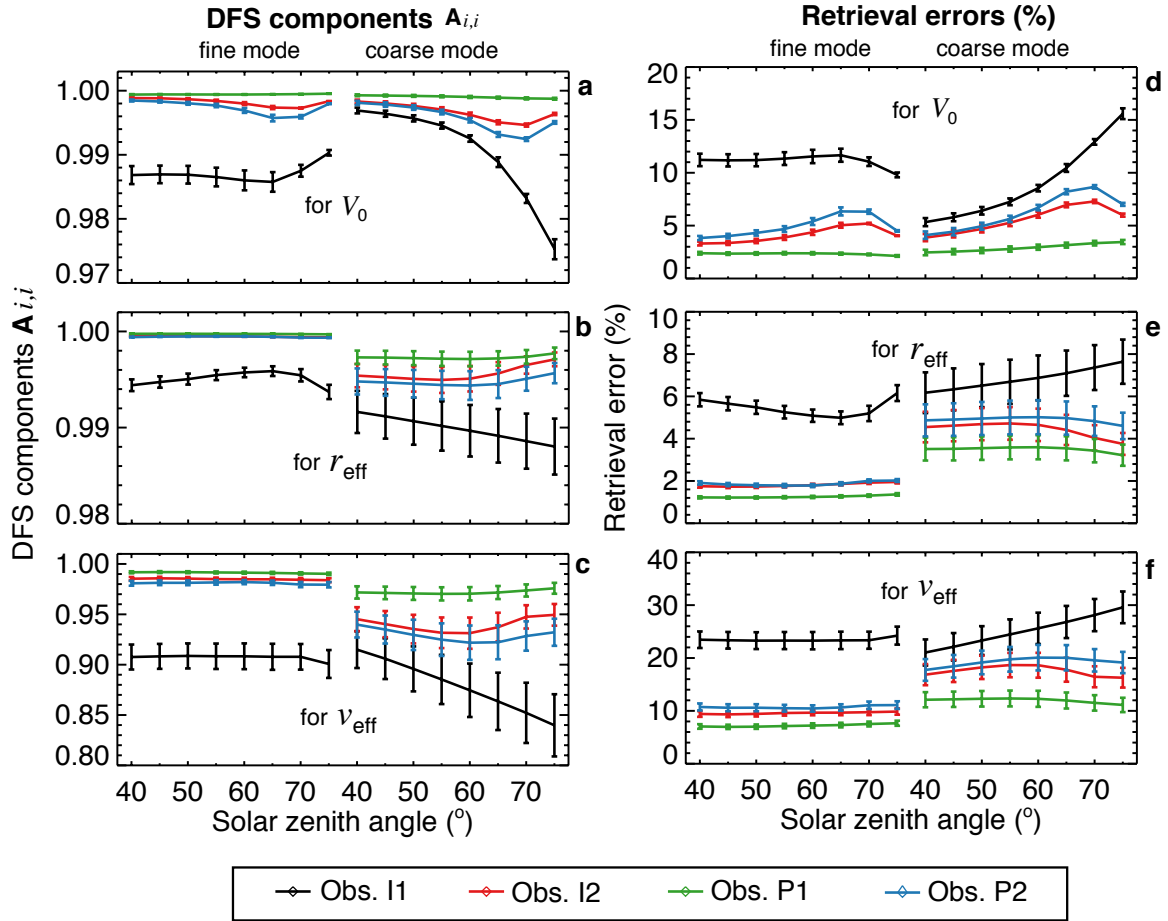


Figure 4.6: DFS components (left column) and retrieval uncertainty (right column) as a function solar zenith angle with different observation scenarios defined in Table 4.3. Quantities are averages for three aerosol types defined in Table 4.2, and error bars represent one fifth of standard deviation. Three rows from top to bottom are respectively for retrieving  $V_0$ ,  $r_{\text{eff}}$ , and  $v_{\text{eff}}$ . In each panel, shown in the left is for the fine mode and in the right is for the coarse mode.

the scenarios P1 and P2 contain additional information that is independent of the scattering angle limitation as discussed in the section 4.3.1.

Overall, the increase in DFS components by adding polarization measurements is less than 0.1 for retrieving  $V_0$ ,  $r_{\text{eff}}$ , and  $v_{\text{eff}}$ , because radiances alone contain abundant information. The retrieval accuracy in aerosol PSD from observations of all scenarios exceeds the requirements for better quantifying aerosol climate radiative forcing identified

by *Mishchenko et al.* [2004]. Even so, the addition of multi-band  $\text{DOLP}_{\text{pp}}$  measurements to the inversion can still yield up to  $\sim 70\%$  retrieval error reduction in the fine-mode and up to  $\sim 50\%$  reduction in the coarse-mode aerosol PSD parameters.

#### 4.3.2.2 Refractive indices

As shown in Figure 4.7a-b, different magnitudes prevail in the DFS components for the  $m_r$  between fine and coarse modes and among different observation scenarios. For example, DFS components for aerosols in the fine mode overreach 0.8 at all four wavelengths in the scenario I1; while the counterparts in the coarse mode approach 0.5 at 1020 nm and are less than 0.2 for the other three wavelengths. This is due to the weaker sensitivity of almucantar radiances to the coarse-mode  $m_r$  (as in Figure 4.4d) comparing to that for aerosol in the fine mode (as in Figure 4.3d). In general, adding the  $\text{DOLP}_{\text{alm}}$ ,  $I_{\text{pp}}$ , or both the  $I_{\text{pp}}$  and  $\text{DOLP}_{\text{pp}}$  in the inversion increases the DFS components for  $m_r$  of aerosols in both the fine and the coarse modes. Particularly, DFS components achieve the most significant rise in the scenario P1 by climbing to 0.95–1.0 in the fine mode and to 0.4–0.8 in the coarse mode. Also shown in Figure 4.7a, an increasing pattern with solar zenith angles is found in the DFS components for the fine-mode aerosol at larger wavelengths because stronger sensitivity occurs in larger scattering angles.

As expected, the retrieval of  $m_r$  can be more accurate by adding additional measurements. According to Figure 4.7c-d, the *a posteriori* error in  $m_r$  averaged on the four spectral bands is  $\sim 0.015$  (0.065) for aerosols in the fine (coarse) mode from measurements in the scenario I1. In contrast, it is reduced to 0.008 (0.037), 0.005 (0.035), and 0.009 (0.040) in the scenarios I2, P1, and P2, respectively. Retrieval errors in the coarse-mode  $m_r$  are larger in shorter spectral wavelengths because of weaker sensitivity to the  $I_{\text{alm}}$  and  $\text{DOLP}$ . For instance of the scenario P1, it is about 0.06 at 440 nm, 0.035 at 675 nm, and 0.02 at 870 and 1020 nm.

The DFS components for the  $m_i$  are shown in Figure 4.8a–b, and the corresponding

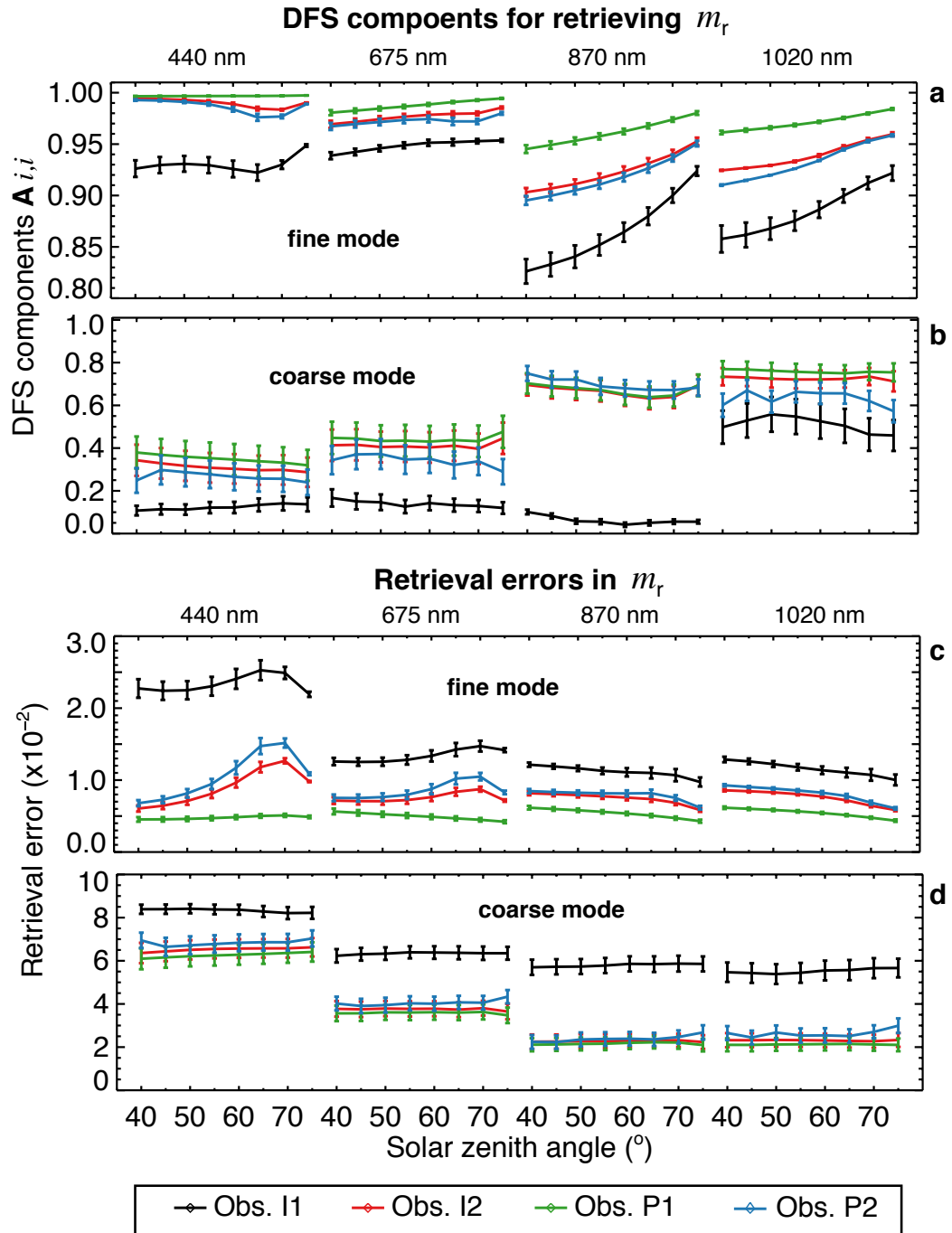


Figure 4.7: Same as Figure 4.6 but for DFS components (a-b) and retrieval uncertainty (c-d) for retrieving real part refractive index  $m_{real}$  in four wavelength bands. (a) and (c) are for the fine aerosol mode, while (b) and (d) for the coarse mode.

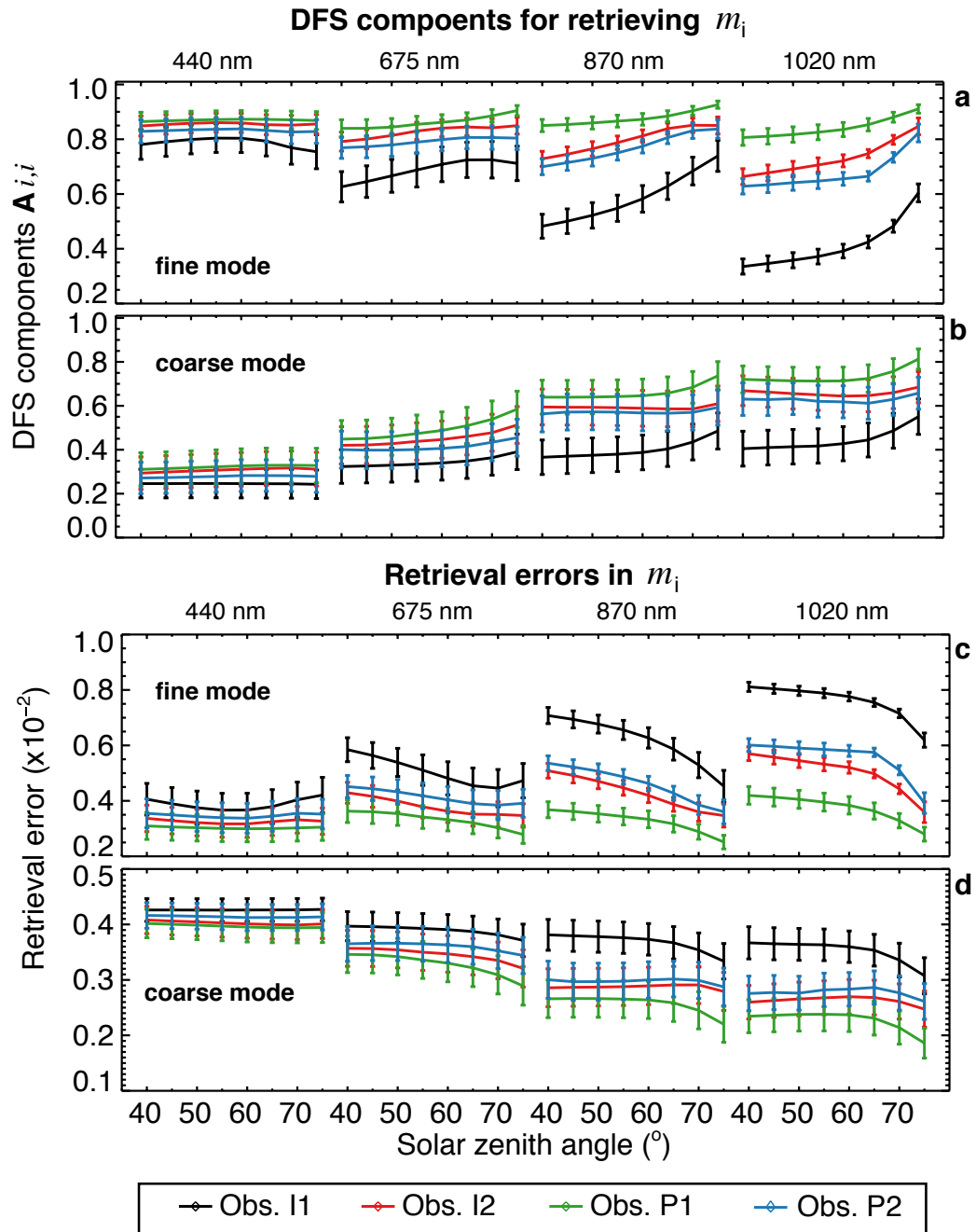


Figure 4.8: Same as Figure 4.7 but for retrieving imaginary part refractive index  $m_i$ .



Table 4.4: Error for retrieved and derived parameters among *a priori*, *a posteriori*, and Glory characterization<sup>a</sup>.

Entries	Error in retrieved parameters					
	$V_0$ (%)	$r_{\text{eff}}$ (%)	$v_{\text{eff}}$ (%)	$m_r$	$m_i$	$\omega_A$
A priori	100/100	80/80	80/80	.15/.15	.01/.05	-
Obs. I1	11./9.0	5.5/6.8	23/25	.015/.065	.0057/.0038	.037/.085
Obs. I2	4.1/5.5	1.8/4.4	10/18	.008/.037	.0041/.0032	.024/.073
Obs. P1	2.3/2.9	1.3/3.5	7.2/12	.005/.035	.0033/.0030	.019/.068
Obs. P2	4.9/6.2	1.9/4.9	11/19	.009/.040	.0044/.0034	.026/.076
Glory <sup>b</sup>	–	10	40	.02	–	.03

<sup>a</sup>Results of our work are averaged values for three aerosol types and for solar zenith angles from 40° to 70°.

<sup>b</sup>Referred to [Mishchenko et al. \[2004\]](#).

retrieval errors in  $m_i$  are displayed in Figure 4.8c–d. Similar to those for the  $m_i$ , DFS components for retrieving the  $m_i$  are larger in the fine mode and show an increasing pattern with the solar zenith angle. Observations in the scenario P1 always yield largest DFS components and smallest retrieval error for the  $m_i$ , followed by the scenarios P2 and I2. Observations in the scenario I1 offer the  $m_i$  retrieval with largest error. If averaged on the solar zenith angles and aerosol types, the retrieval error in the  $m_i$  is 0.006 (0.004) for aerosol in the fine (coarse) mode in the scenario I1, and can be reduced to 0.003 (0.003) in the scenario P1.

#### 4.3.2.3 Single scattering albedo

Note that the aerosol single scattering albedo  $\omega_A$  is an intermediate rather than a directly retrieved parameter. The error in  $\omega_A$  can be estimated from the  $\hat{\mathbf{S}}$  with the equation (3.9). The  $\omega_A$  for each aerosol mode uniquely depends on the light wavelength and aerosol microphysical parameters including  $r_{\text{eff}}$ ,  $v_{\text{eff}}$ , and  $m_r$  and  $m_i$ , although the  $m_i$  impacts  $\omega_A$  most significantly [[Hansen and Travis, 1974](#)]. Required derivatives of  $\omega_A$  to these parameters in the equation (3.9) can be obtained from the linearized Mie code (section 2.2.2) integrated

into the UNL-VRM. We calculated uncertainties in the  $\omega_A$  for each wavelength and each aerosol type, and the averaged values are summarized in Table 4.4. Observations in these four scenarios can retrieve  $\omega_A$  with the uncertainty of 0.037, 0.024, 0.019, and 0.026 for the fine mode, and 0.085, 0.073, 0.068, and 0.076 for the coarse mode, respectively. Thus, only the fine-mode  $\omega_A$  retrieval with polarization involved can meet the accuracy requirements (0.03) for accurate climate forcing estimates [Mishchenko *et al.*, 2004]. We noted that the mean uncertainty in the coarse-mode  $\omega_A$  exceeds 0.06 in all of these four scenarios, but higher accuracy may be achieved under coarse-dominated conditions as shown in the following section.

#### 4.4 Sensitivity of Retrieval Error to AOD and $\text{fmf}_v$

The performance of retrieval usually varies with aerosol conditions like the aerosol loading and the prevalence of aerosol in either the fine or the coarse modes (e.g., fine-mode volume fraction,  $\text{fmf}_v$ ). As a result, uncertainties in aerosol retrievals can depend much more strongly on the AOD than they do on the properties of an individual aerosol model [Knobelspiesse *et al.*, 2012]. For the same reason, the inversion of refractive indices and  $\omega_A$  in the current AERONET algorithm is confined to the condition when the 440-nm AOD is larger than 0.4 [Dubovik *et al.*, 2000; Holben *et al.*, 2006]. Our above analysis, which focused on three aerosol types by a constant AOD value at 440 nm ( $\tau_{A440}=1.0$ ), is insufficient to represent variable global conditions. At the same time, we also found noticeable variability of the DFS components and a posteriori errors existing among three aerosol types with different  $\text{fmf}_v$ , especially for the coarse-mode parameters. Thus, it is necessary to investigate how aerosol conditions affect the retrieval error, in order to answer the question: under what aerosol conditions the AERONET measurements (with and without polarization) are capable to yield retrievals with satisfied accuracy?

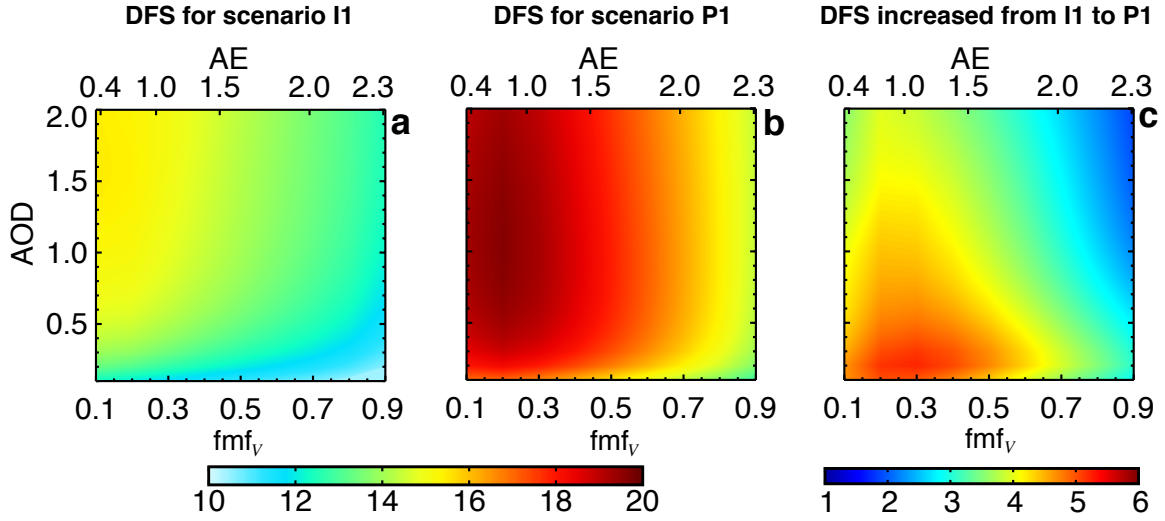


Figure 4.9: Contours of DFS as a function of  $fmf_v$  and AOD in scenarios I1 (a) and P1 (b). (c) the difference of DFS between (a) and (b). Simulations are for solar zenith angle of  $55^\circ$ . The top abscissa denotes Ångström exponent (AE).

We expand our analysis for the  $\tau_{A440}$  ranging from 0.1 to 2.0 and for the  $fmf_v$  from 0.1 to 0.9. In practice, the  $fmf_v$  is inaccessible prior to inversion. Instead, we use the Ångström exponent (AE) from 870 to 1020 nm together with  $\tau_{A440}$  to define the aerosol conditions, because the AE in the longer paired wavelength is highly related to the  $fmf_v$  [Schuster *et al.*, 2006] and immediately available from the AERONET direct sun measurements. With the aerosol properties defined in the Table 4.3, the  $fmf_v$  from 0.1 to 0.9 gives AE values from 0.35 to 2.3. We exclude the scenarios of I2 and P2 in our following analysis, because the scenario P1 demonstrates the most superior performance and is also the focus of our algorithm development.

Figure 4.9a–b display the contours of DFS as a function of the AE (or  $fmf_v$ ) and  $\tau_{A440}$  in the scenarios I1 and P1, respectively. We found that the DFS decreases with an increasing AE and  $fmf_v$  for the same AOD. This is attributed to the fact that the coarse-mode parameters are more difficult to retrieve than their fine-mode counterparts, restrained by their weaker sensitivities to the  $I_{alm}$  and the  $DOLP_{pp}$ . Thus, the decrease in the coarse-mode fraction

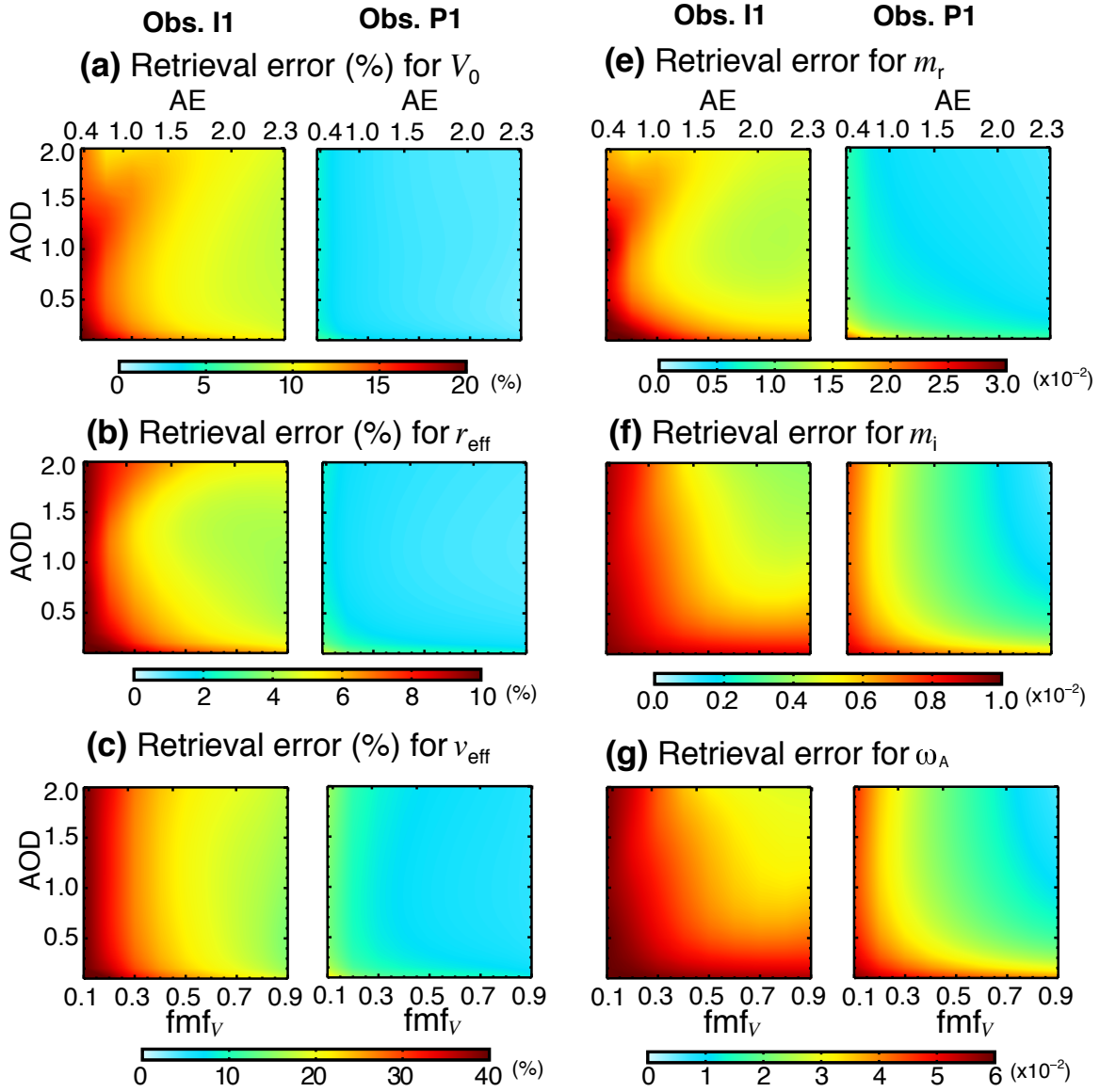


Figure 4.10: Retrieval uncertainties as a function of  $\text{fmf}_v$  (or AE) and AOD for each individual aerosol parameters in the *fine* mode: (a)  $V_0$ , (b)  $r_{\text{eff}}$ , (c)  $v_{\text{eff}}$ , (d)  $m_r$ , (e)  $m_i$ , and (f)  $\omega_A$ . Two sub-panels in each panel indicate observations in the scenarios I1 and P1, respectively. Simulations are for solar zenith angle of  $55^\circ$ . The x- and y-axis are identical to those in Figure 4.9. Relative uncertainties are shown for  $V_0$ ,  $r_{\text{eff}}$  and  $v_{\text{eff}}$ , while absolute errors for  $m_r$ ,  $m_i$ , and  $\omega_A$ . Retrieval errors for  $m_r$ ,  $m_i$ , and  $\omega_A$  are averaged values over the four spectral bands.

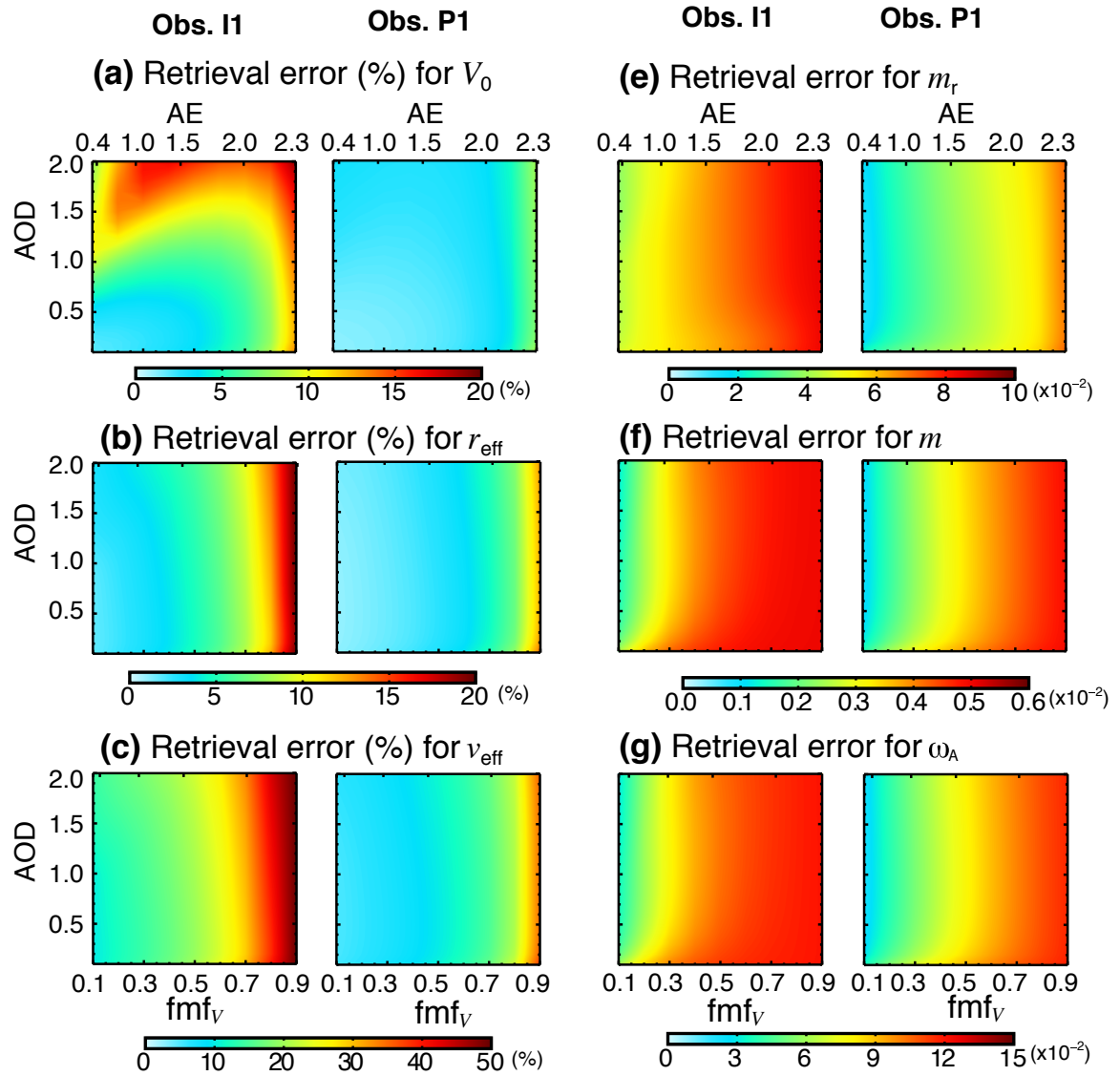


Figure 4.11: Same as Figure 4.10, but for aerosol parameters in the *coarse* mode.

significantly reduces the aerosol information for coarse-mode parameters but retain the information for fine-mode parameters, resulting in decreases in the total DFS. We also notice from Figure 4.9a that the DFS increases with an increasing AOD in the scenario I1. However, AOD change has less impact in the scenario P1 (Figure 4.9b). For example, the DFS values are lower than 14 when  $\text{AOD} < 0.4$  in the scenario I1, whereas even larger DFS can be found in the scenario P1 when  $\text{AOD} < 0.2$ . Therefore, we may expect that the inversion in the scenario P1 will be capable to retrieve aerosol parameters in conditions of lower aerosol loading, and may bring down the  $\tau_{\text{A440}}$  threshold of 0.4 from the current AERONET inversion algorithm to retrieve the refractive index and  $\omega_{\text{A}}$ . Finally, as indicated in Figure 4.9c, the addition of  $I_{\text{pp}}$  and  $\text{DOLP}_{\text{pp}}$  in the inversion can add 2–5 pieces of useful information. Such improvement occurs in all aerosol conditions but is more dominated when enough coarse particles are present:  $\text{fmf}_v < 0.5$  (or  $\text{AE} < 1.6$ ), in which the radiance-only inversion usually yields a large retrieval error for the fine-mode aerosol.

In Figures 4.10 and 4.11, we show the contours of the a posteriori error  $\hat{\epsilon}$  in the scenarios I1 and P1 for the individual fine-mode and coarse-mode parameters, respectively. Overall, observations in scenarios P1 offer more accurate retrievals for all parameters in both the fine and the coarse aerosol modes. In both scenarios, the  $\hat{\epsilon}$  decreases for fine-mode parameters and increases for coarse-mode parameters with increasing the AE (or  $\text{fmf}_v$ ) for same  $\tau_{\text{A440}}$ , indicating that the relative contribution of fine and coarse modes determines the relative information of each mode. Extreme cases are  $\text{fmf}_v$  of 1 or 0, i.e., the absence of the coarse- or fine-mode aerosols, which certainly will only allow a mono-modal retrieval. Thus, the bi-modal retrieval, especially for refractive indices, requires that aerosols reach certain mixture conditions to contain enough information for both modes. For example in the scenario I1, while the fine-mode  $r_{\text{eff}}$  can be well retrieved with 5% accuracy when the  $\text{fmf}_v > 0.2$  at  $\tau_{\text{A440}}$  of 0.5 (Figure 4.10b), the  $\text{fmf}_v > 0.3$  is required to ensure the  $\hat{\epsilon} < 0.02$  in the fine-mode  $m_r$  (Figures 4.10e). Comparing to the change of the  $\text{fmf}_v$ , the change of

Table 4.5: Required aerosol conditions ( $\tau_{A440}$  and AE) to achieve anticipated retrieval accuracy  $< \varepsilon >$  for observations in scenario I1 and P1.

$\mathbf{x}$	$< \varepsilon >$	Scenario I1		Scenario P1	
		$\tau_{A440}$	AE	$\tau_{A440}$	AE
$V_0^f$	10%	$>0.3$	$>1.5$	<sup>a</sup> All	All
$V_0^c$	10%	$<1.3$	$<2.2$	All	All
$r_{\text{eff}}^f$	5%	$>0.3$	$>1.3$	All	All
$r_{\text{eff}}^c$	10%	All	$<2.0$	All	$<2.2$
$v_{\text{eff}}^f$	20%	$>0.3$	$>1.5$	All	All
$v_{\text{eff}}^c$	30%	All	$<1.8$	All	$<2.2$
$m_r^f$	0.02	$>0.4$	<sup>b</sup> $>1.0$	All	All
$m_r^c$	0.04	All	$<1.0$	All	$<1.8$
$\omega_A^f$	0.04	$>0.6$	$>1.5$	$>0.2$	$>0.7$
$\omega_A^c$	0.08	$>0.2$	$<1.1$	All	$<1.6$

<sup>a</sup>‘All’ indicates conditions:  $0.1 < \tau_{A440} < 2.0$  and  $0.35 < \text{AE} < 2.3$ ;

<sup>b</sup>Underlined bold indicate conditions that cannot allow bi-modal retrievals.

$\tau_{A440}$  has less impact on the  $\hat{\varepsilon}$  of the PSD parameters; and this impact occurs in low aerosol loadings. For example, Figure 4.10g shows that a minimum of  $\sim 0.4$  for  $\tau_{A440}$  is required in the scenario I1 to guarantee a retrieval error in the fine-mode  $\omega_A$  less than 0.04 when  $\text{fmf}_v = 0.5$ .

From the Figures 4.10 and 4.11, we can identify required aerosol conditions in terms of the AE and  $\tau_{A440}$  in order to achieve certain anticipated accuracy  $< \varepsilon >$ , which are summarized in Table 4.5. Clearly, observations with polarization can enable retrievals of same accuracy in a lower aerosol loading. For example, the retrieval accuracy of 10% for the  $V_0$  and  $r_{\text{eff}}$  and 30% for the  $v_{\text{eff}}$  in the fine mode requires  $\tau_{A440}$  to be larger than 0.3 for inversion in the scenario I1 (Figure 4.10a–c). In contrast, inversion in the scenario P1 can easily ensure retrievals of the same accuracy when  $\tau_{A440}$  is 0.1. For the fine-mode  $m_r$  retrieval, an accuracy of 0.04 requires  $\tau_{A440} > 0.4$  for the inversion I1 but  $\tau_{A440} > 0.2$  for the inversion P1 (Figure 4.10e). Moreover, the radiance-only inversion is unable to resolve the bi-modal  $m_r$  and  $\omega_A$  under any circumstance, because  $\text{AE} > 1.5$  is necessary for retrieving the fine-mode  $\omega_A$  (Figure 4.10g), meanwhile  $\text{AE} < 1.1$  is required for its coarse-mode retrieval

(Figure 4.11g). This agrees with *Dubovik et al.* [2000] in that the retrieval of refractive indices for both fine and coarse mode is essentially non-unique due to limited information in the AERONET (radiance-only) observations. In contrast, observations in the scenario P1 can allow bi-modal retrievals of the  $m_i$  and  $\omega_A$  when  $0.7 < AE < 1.6$  and  $\tau_{A440} > 0.2$  (Figures 4.10g and 4.11g). Therefore, our retrieval algorithm is designed to use observations of scenario P1 to retrieve bi-modal refractive indices when  $\tau_{A440}$  and AE reach these criteria. In aerosol conditions beyond the criteria, bi-modal PSD along with a mono-modal refractive index will be retrieved by assuming the refractive index is independent of the aerosol mode.

## 4.5 Summary

In an effort to improve the AERONET inversion by including additional polarization measurements, this study examines the potential microphysical aerosol information contained in the AERONET photo-polarimetric observations. We have focused our analysis on how the added polarization measurements impact on the retrieval accuracy the in aerosol particle size distribution (PSD), spectral refractive index, and single scattering albedo  $\omega_A$ . A numerical testbed has been constructed to generate the synthetic AERONET radiance and degree of linear polarization (DOLP) over 440, 675, 870, and 1020 nm. We considered four scenarios of observations to whether or not include the DOLP for the inversion, i.e., (I1) direct Sun AOD and almucantar sky radiances, (I2) observations in the scenario I1 with additional radiance measurements in the solar principal plane, (P1) observations in the scenario I2 plus polarization measurements in the solar principal plane, and (P2) observations in the scenario I1 plus almucantar polarization. Measurements in the scenario I1 are those used in current AERONET inversion algorithm, and thus represent a control experiment. For each observation scenario, we also considered three aerosol types to represent general aerosol climatology. The Bayesian statistical approach then was applied to relate information



contained in those synthetic data and retrieval errors in aerosol physical parameters to the instrumental as well as the a priori characteristics. Then the error-normalized Jacobian, degree of freedom for signal (DFS), and the a posteriori error in each individual retrieved parameter were presented as function of solar zenith angle for these observation scenarios.

The results show a remarkable increase in information by adding additional polarization and/or radiances into the inversion. Overall, observations in the scenario P1 yield the highest DFS, which is larger than that in the scenario I1 by 2–5 for all defined aerosol types. This can be understood that polarization measurements in the solar principal plane, in comparing with sky radiances in solar almucantar, have complementary sensitivities with respect to retrieved aerosol parameters. Also, measurements in the principal plane allow a wider range of scattering angles and supplies more information on aerosol backscattering. In scenario P2, adding polarization in the solar almucantar offer an increase of  $\sim 2$  pieces of information with DFS values slightly below those in scenarios I2. We also note that the DFS increases with increasing solar zenith angle for all cases, resulting from more information contained in observations of a wider range of scattering angle.

We also analyzed the DFS components and the a posteriori uncertainty for each individual retrieved parameter. As expected, the smallest retrieval errors were always found in the scenario P1: 2.3% (2.9%) for the volume concentration, 1.3% (3.5%) and 7.2% (12%) for the effective radius and effective variance, 0.005 (0.035) for the real part of refractive index, and 0.019 (0.068) for the single scattering albedo in the fine (coarse) mode. These values represent an error reduction from the scenario I1 of 79% (57%), 76% (49%), 69% (52%), 66% (46%), and 49% (20%), respectively. Uncertainties in retrieved parameters averaged among these three aerosol types are summarized in the Table 4.4 for each observation scenario.

Seeking to answer under what conditions the inversions can achieve a mode-resolved aerosol refractive index and  $\omega_A$ , we further investigated how the AOD ( $\tau_{A440}$ ) and fine/coarse

modal domination (in terms of Ångström exponent, or AE) influence the retrieving accuracy from observations in the scenarios I1 and P1. We found that adding principal-plane polarization measurements can increase the DFS by up to  $\sim 5$  in cases dominated by coarse-mode particles ( $\text{fmf}_v < 0.5$ ), in which the radiance-only inversion usually yields larger retrieval uncertainty for fine-mode aerosol. As a consequence, these photo-polarimetric observations can enable accurate retrievals in a lower aerosol loading when the  $\tau_{A440}$  is 0.1, except for the fine-mode  $m_r$  retrieval that requires  $\tau_{A440} > 0.2$ . The analysis also indicate that the radiance-only inversion is unable to resolve bi-modal  $m_i$  and  $\omega_A$  under any circumstance. However, observations in the scenario P1 can allow bi-modal retrievals of  $m_i$  and  $\omega_A$  when  $0.7 < \text{AE} < 1.6$ . Such criteria can guide us in the practical retrieval algorithm to determine whether a mono-modal or bi-modal retrieval of the aerosol refractive index and  $\omega_A$ . In aerosol conditions beyond the criteria, bi-modal PSD along with the mode-independent refractive index will be retrieved.

Finally, it should be noted that in our analysis the aerosol particles in each mode are assumed to be poly-disperse homogeneous spheres. Although the linearized T-matrix code has been implemented in our model, the simulation of scattering properties for large non-spherical particles (for example spheroids) still remain computational limitations. Our future efforts will implement non-spherical treatment in order to more realistically represent mineral dust aerosols.

## CHAPTER 5

### CASE DEMONSTRATIONS

#### 5.1 Introduction

As suggested by the information content analysis in last chapter, adding polarization data into the AERONET inversion will enable the retrieval of bi-modal refractive index and SSA even for 440-nm AOD as low as 0.2 when the Ångström exponents (AE) is between 0.7 and 1.6. We also found that the uncertainty in the retrieval can be reduced by up to 79% (57%), 76% (49%), 69% (52%), 66% (46%), and 49% (20%) for the fine-mode (coarse-mode)  $V_0$ ,  $r_{\text{eff}}$ ,  $r_{\text{eff}}$ ,  $m_r$ , and SSA, respectively. In this chapter, our new research algorithm is applied to a suite of photo-polarimetric measurements taken from the new-generation SunPhotometer at the Beijing\_RADI AERONET station. I present the selected cases and the *a priori* characterization in section 5.2, and discuss the fitting residuals in section 5.3 and the retrieved results in section 5.4. A contrast analysis is presented in section 5.5 to demonstrate the superiority of the inversion involving polarization.

#### 5.2 Selected Cases and the *a priori* Characterization

We applied our algorithm to the radiance and polarization measured by the CIMEL CE318-DP SunPhotometer (instrument #350) at Beijing\_RADI (116.37°E, 40.00°N), which is a joint station of the AERONET and the Sun/sky-radiometer Observation NETwork (SOnet).

The AOD measurements are designated from the field-calibrated level 1.5 products. Measurements of the direct and diffuse radiance as well as DOLP were performed at eight spectral wavelengths, with the measurements at 440, 675, 870, and 1020 nm chosen for the inversion. The sky radiances were calibrated following *Li et al.* [2008] and are reported as values normalized by the extra-terrestrial solar irradiance. The DOLP were calibrated in the laboratory following *Li et al.* [2010]. Measurement uncertainties were estimated to be 0.01–0.02 for AOD, 3–5% for radiance, and 0.01 for DOLP.

The *a priori* is characterized with the climatology of aerosol properties derived from the version 2.0 AERONET daily inversion products of the same site during 2011–2013. The PSD parameters were analyzed with 299 available daily inversions when the 440-nm AOD is larger than 0.2. The refractive index and SSA were analyzed with 215 inversions when the 440-nm AOD is larger than 0.4. In Figure 5.1, the variables are shown as functions of the fine-mode-fraction in terms of the aerosol volume, or  $\text{fmf}_v$ . It can be found that the  $\text{fmf}_v$  from 0.2 to 0.6 accounts for  $\sim 70\%$  of occurrences (Figure 5.1a), indicating aerosol over this site is dominated by the mixed fine-coarse aerosols. The AE derived from the 1020-nm and 870-nm AOD pairs is more linearly related to the  $\text{fmf}_v$  than the 440-nm and 870-nm AE (Figure 5.1b), because AE over the longer-wavelength pairs is more sensitive to the component fraction and less sensitive to the change of component particle size [*Schuster et al.*, 2006]. From Figure 5.1c–f, we determine the *a priori* ( $\mathbf{x}_a$ ) based on the corresponding mean values. For refractive index, we pick their mean values when  $\text{fmf}_v < 0.2$  for the coarse

Table 5.1: Main characteristics of case studies in this work.

Case	Date & Time UTC	$\theta_0(^{\circ})$	$\tau_{A440}$	AE (870/1020nm)	OMI NO <sub>2</sub> (molec/cm <sup>2</sup> )	OMI O <sub>3</sub> (DU)	Vapor (cm)
A	02/22/2011 04:30	50.3–50.6	3.46	1.57	$6.3 \times 10^{16}$	356.5	0.86
B	03/17/2013 03:25	43.0–42.2	2.74	1.39	$4.2 \times 10^{16}$	332.7	0.76
C	03/22/2013 07:23	57.0–60.0	1.05	1.01	$4.1 \times 10^{16}$	386.7	1.01

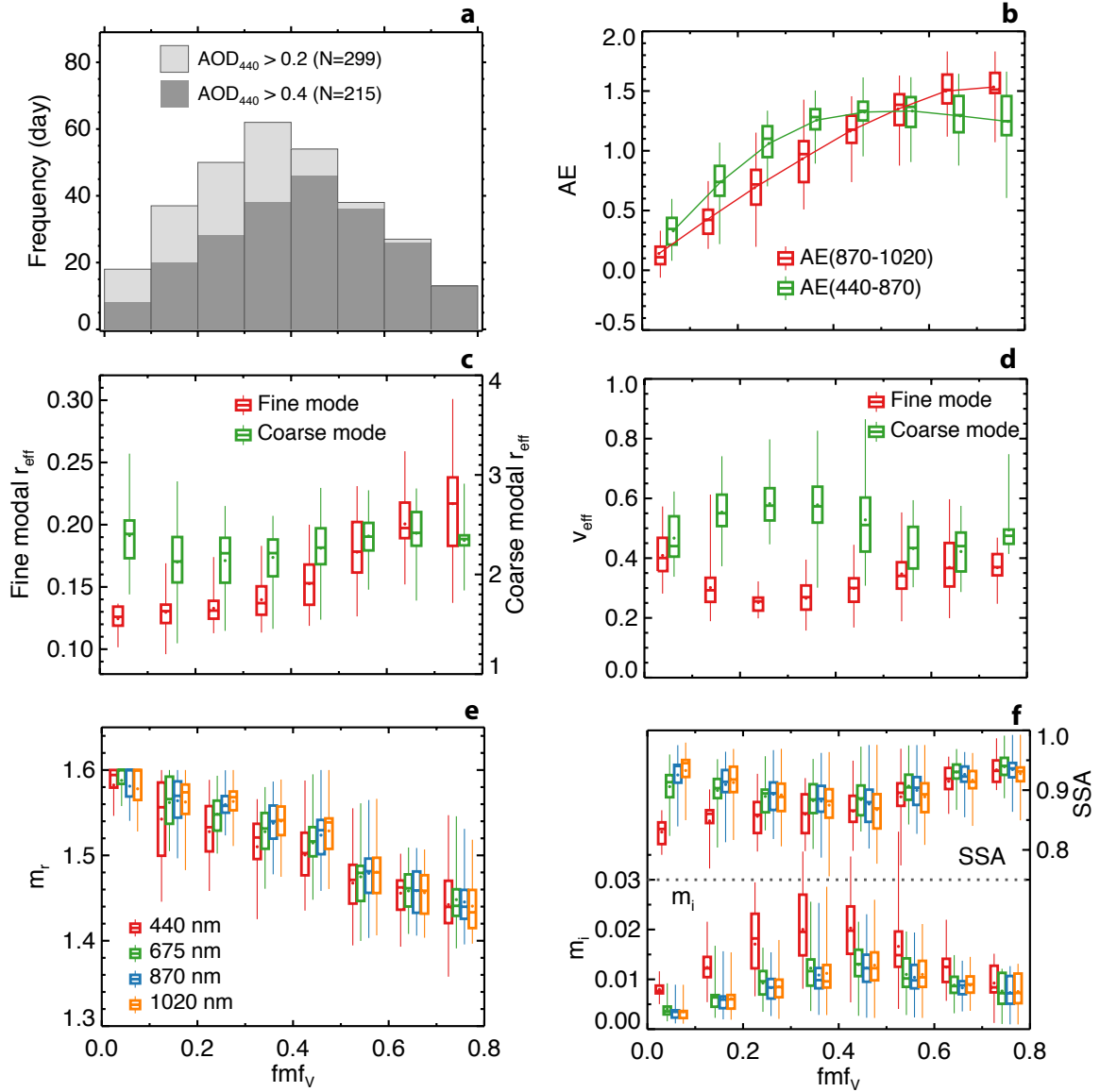


Figure 5.1: Climatology of aerosol properties over the Beijing\_RADI site derived from AERONET daily inversion products during 2011–2013. The variables are shown as functions of the fine-mode-fraction in terms of the aerosol volume, or  $\text{fmf}_v$ . Eight bins are applied for  $\text{fmf}_v$  from 0 to 0.8 with an increment of 0.1. The six panels are: (a) Histogram of used data; (b) the Ångström exponents (AE) derived from 870 to 1020 nm (red) and from 440 to 870 nm (green) wavelength pairs; (c) the effective radius for aerosols in the fine (red) and coarse (green) mode; (d) the effective variance in the fine (red) and coarse (green) mode; (e) the real part of the refractive index at 440, 675, 870, and 1020 nm; and (f) the imaginary part of the refractive index and aerosol SSA at the same wavelengths.

mode and when  $\text{fmf}_v > 0.6$  for the fine mode. The *a priori* error ( $\epsilon_a$ ) for each parameter is determined by the relevant physical range, and is listed in the last column of Table 5.4. In addition, we found in the Figure 5.1e that the  $m_r$  retrievals decrease quasi-linearly with the increasing  $\text{fmf}_v$ , which indicates the  $m_r$  has distinct values between aerosols in the fine and the coarse modes over this site. It is expected that, the  $m_r$  in the mixed aerosol situations, e.g.,  $0.3 < \text{fmf}_v < 0.6$ , is also expected to have the separated values for fine- and coarse-mode particles.

With the above *a priori* characterization, we performed retrievals for three cases, respectively, on 22 February 2011, 17 March 2013, and 22 March 2013 (hereinafter, cases A, B, and C). A brief characterization of these cases is presented in Table 5.1. Indeed, these cases represent different aerosol mixtures: (A) dominated by fine particles, (B) well-mixed, and (C) dominated by large particles. Moreover, the present algorithm is designed to run with two inversion scenarios: the first includes DOLP, while the second ignores it—hereafter, we label these scenarios type P and I, respectively. An examination of the difference in the fitting results between these two types of inversion would indicate the value of DOLP in improving the retrieval. For all cases, optimal solutions are achieved within less than thirty iterations, and further iterations yield negligible reduction of the cost function.

### 5.3 Fitting Residuals

The fitting residual characterizes the disagreement between the model and the measurement. The individual sky radiance residual is defined as a relative quantity:

$$e_I = (I_{\text{calc}} - I_{\text{meas}}) / I_{\text{meas}} \quad (5.1)$$

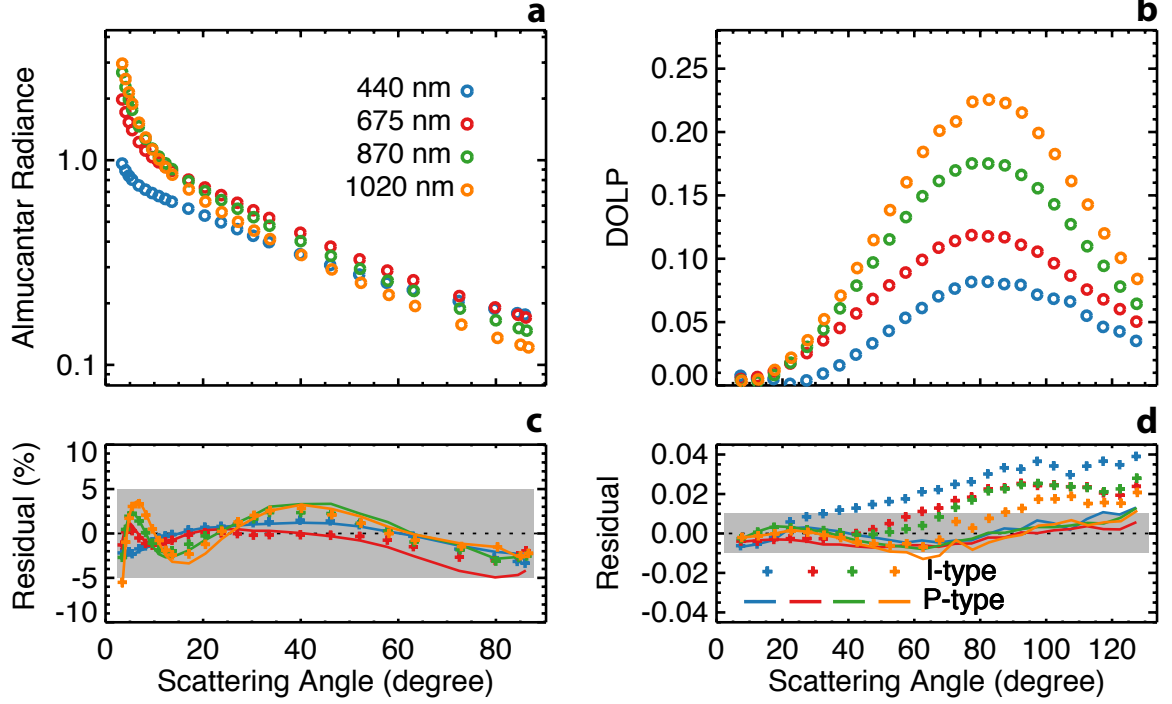


Figure 5.2: a) Measured almucantar normalized radiances. (b) Measured DOLP in the solar principal plane. (c) Fitting residuals for almucantar radiances by the P-type inversion (solid curves) and I-type inversion (crosses). (d) Same as panel (c), but for fitting the residuals of principal-plane DOLP. Four colors indicate different wavelengths: blue for 440 nm, green for 675 nm, red for 870 nm, and orange for 1020 nm. Gray areas in panels c–d indicate the measurement uncertainty.

where  $I_{\text{calc}}$  and  $I_{\text{meas}}$  denote the calculated (using the retrieved aerosol parameters) and measured sky radiances, respectively. In contrast, the fitting residuals for AOD and DOLP are defined by:

$$e_{\text{AOD}} = \text{AOD}_{\text{calc}} - \text{AOD}_{\text{meas}}, \quad (5.2)$$

$$e_{\text{DOLP}} = \text{DOLP}_{\text{calc}} - \text{DOLP}_{\text{meas}}. \quad (5.3)$$

The residual errors for AOD, sky radiance, and DLOP are mean values of  $|e_I|$ ,  $|e_{\text{AOD}}|$ , and  $|e_{\text{DOLP}}|$ , respectively.

Because similar fitting results are found for these three aerosol types (cases), we illustrate

Table 5.2: Summary of measurement fitting errors.

Case	Inversion type	AOD residual error	Radiance residual error	DOLP residual error
A	I	0.0005	1.68%	0.008
	P	0.0010	1.78%	0.005
B	I	0.0003	1.43%	0.014
	P	0.0003	1.67%	0.004
C	I	0.0007	2.77%	0.027
	P	0.0034	3.73%	0.009

in Figure 5.2 the fitting results for sky radiances and DOLP only for the case B. The statistical residual errors are displayed in Table 5.2 for all three cases. We found that retrievals from both types of inversion can well reproduce these AERONET measurements of AOD and sky radiances. Fitting residuals from both types of inversions for individual ALM radiance measurement lie within the experimental uncertainty of 5%, although the fit of radiances from the P-type inversion is slightly deteriorated: residual error is 1.67% for the P-type compared 1.43% for the I-type inversion. However, the DOLP residual error can be much larger for the I-type inversion than that for the P-type inversion: 0.014 versus 0.004. As these fitting results show, without the constraints imposed by polarization, the retrieved aerosol microphysical parameters could result in larger error in polarization simulations, highlighting the necessity to include polarization in the inversion as an additional source of constraint.

## 5.4 Retrieved Aerosol Properties

Figure 5.3 displays our retrievals from both I-type and P-type inversions for the aerosol volume PSD and complex refractive indices. Also shown are the retrievals from the AERONET Dubovik00&06 inversion. Table 5.3 presents the values of the (P-type inversion) retrieved PSD parameters including  $V_0$ ,  $r_{\text{eff}}$ ,  $v_{\text{eff}}$ ,  $r_v$ , and  $\sigma_g$  for both fine and coarse modes, and



corresponding values from the Dubovik00&06 inversion. The PSD in these cases consists separated fine and coarse aerosol modes. In the cases dominated by fine-mode aerosol (A) and well-mixed aerosol (B), our retrievals agree with the AERONET inversions, though marginal differences are found in the effective radius and standard deviation. In case C dominated by coarse-mode aerosols, our algorithm results in a smaller coarse mode  $r_{\text{eff}}$  than that from the AERONET algorithm; this may be caused by our assumption of spherical particles, whereas the Dubovik00&06 algorithm considers non-sphericity for coarse particles. We did not find significant differences in the aerosol volumes between our algorithm and the Dubovik00&06 algorithm. As Figure 5.3b–c indicate, fine-mode volume retrieved by the P-type inversion is lower than that retrieved by the I-type inversion; such an overestimation from radiance-only inversion was also found by *Li et al.* [2009].

In contrast with the Dubovik00&06 algorithm, which retrieves a single refractive index for each spectrum that is independent of aerosol size, our retrieved aerosol refractive indices are pertain to the corresponding fine and coarse modes. In order to get a general impression of the agreement between our retrievals and the AERONET inversions, we compute the bulk refractive index that is a weighted average by the particle volume of each mode in our retrieval [e.g., *Wang and Martin, 2007*]. According to Figure 5.3d–f, while the bulk value of  $m_r$  is in good agreement (differences  $< 0.03$ ) with that of the Dubovik00&06 retrievals, our retrieval allows for a mode-resolved characterization of aerosol refractive index. For instance, the aerosol  $m_r$  has values 1.5–1.6 in the coarse mode, which is larger than that in the fine mode (1.4–1.5). In addition, we found that the P-type inversion usually yields higher values of  $m_r$  compared to the I-type inversion; this finding agrees with *Li et al.* [2009] in that the radiance-only inversion underestimates  $m_r$ .

According to Figure 5.3g–i, the bulk  $m_i$  retrieved by our algorithm is consistent overall with that from the Dubovik00&06 algorithm, with both retrievals showing similar spectral dependencies. One exception is for case C;  $m_i$  at 440 nm is about 0.01 from our algorithm but

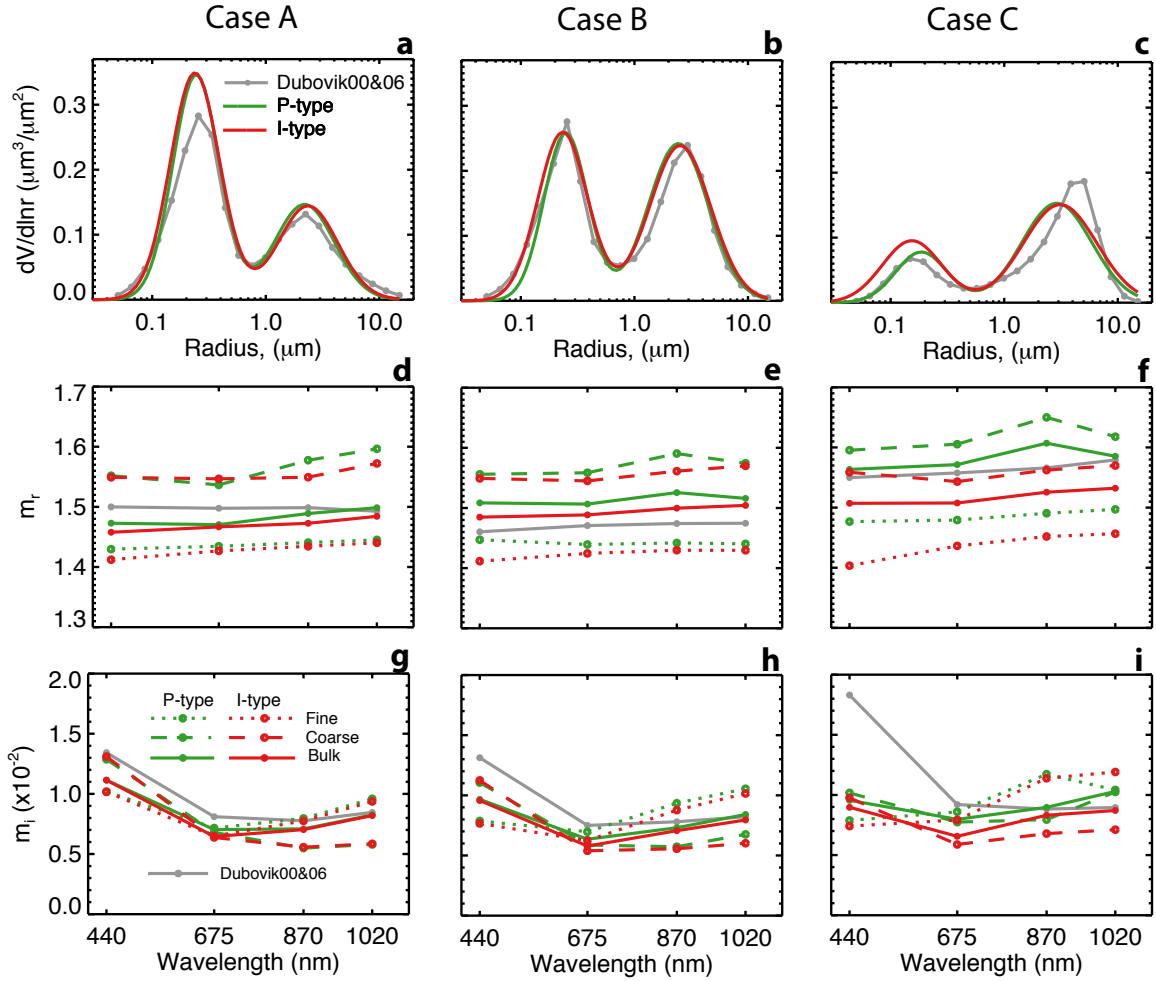


Figure 5.3: Retrieved aerosol volume size distribution (PSD) and refractive index compared with Dubovik00&06 inversions (gray). P-type and I-type inversions are represented by green and red colors, respectively. In panels d–i, the retrievals are shown for aerosols in both fine (dotted) and coarse (dashed) modes, as well as bulk averages (solid). The PSD relevant quantities for panels a–c are summarized in Table 5.3.

is about 0.02 with the Dubovik00&06 algorithm. As expected, our inversion algorithm also offers mode-resolved  $m_i$ . We notice in our retrieval that  $m_i$  shows an increasing dependence on the spectral wavelength for the fine mode but a decreasing tendency for the coarse mode.

In the forward modeling framework, the aerosol macrophysical optical properties act as intermediate model parameters to link the aerosol microphysical characteristics to the radiation fields. These macrophysical optical parameters include but are not limited to the

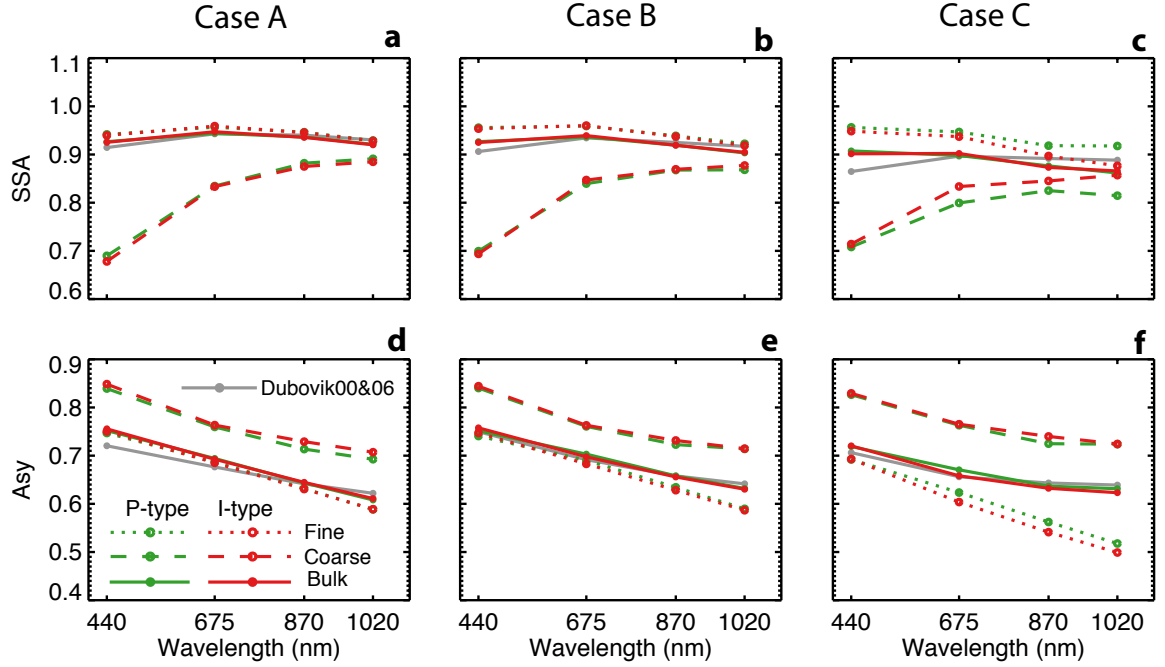


Figure 5.4: Same as Figure 5.3, but for derived aerosol SSA and Asy.

Table 5.3: PSD-related parameters retrieved by our P-type inversion, compared with values from the AERONET Dubovik00&06 inversion.

x	Units	Case A		Case B		Case C	
		Ours	AERONET	Ours	AERONET	Ours	AERONET
$V_0^f$	$\mu\text{m}^3\mu\text{m}^{-2}$	0.41	0.36	0.29	0.31	0.10	0.09
$r_{\text{eff}}^f$	$\mu\text{m}$	0.218	0.208	0.226	0.201	0.163	0.156
$v_{\text{eff}}^f$	—	0.25	0.32	0.22	0.32	0.31	0.33
$r_v^f$	$\mu\text{m}$	0.243	0.240	0.249	0.232	0.186	0.179
$\sigma_g^f$	—	1.60	1.69	1.56	1.69	1.68	1.70
$V_0^c$	$\mu\text{m}^3\mu\text{m}^{-2}$	0.22	0.21	0.37	0.32	0.27	0.26
$r_{\text{eff}}^c$	$\mu\text{m}$	1.83	2.01	2.02	2.26	2.26	2.61
$v_{\text{eff}}^c$	—	0.44	0.53	0.45	0.38	0.65	0.50
$r_v^c$	$\mu\text{m}$	2.20	2.44	2.44	2.65	2.91	3.28
$\sigma_g^c$	—	1.83	1.92	1.84	1.76	2.03	1.89

aerosol SSA ( $\omega_A$ ), the scattering phase function, and the asymmetry factor (Asy). These quantities do not appear in the state vector; instead, they can be derived from the retrieved microphysical parameters, and are thus called derived or intermediate parameters. In Figure 5.4, we present  $\omega_A$  and Asy from our retrieval, and the comparison with their counterparts

from the Dubovik00&06 inversion. In our retrieval, bulk values of  $\omega_A$  and  $Asy$  are again calculated by a scatter-weight averaging of the fine and coarse mode values. We found that the bulk  $\omega_A$  and  $Asy$  from our algorithm and the Dubovik00&06 algorithm agree very well. However, our retrieved coarse-mode  $\omega_A$  varies from 0.7 to 0.9, increasing with wavelength. In contrast, the retrieved fine-mode  $\omega_A$  runs close to 0.9.

## 5.5 Improvement over Radiance-Only Retrievals

The above comparisons of retrieval results confirm that both P- and I-type inversions by our algorithm can generate solutions quite consistent with the current Dubovik00&06 algorithm. In order to demonstrate the improvements in the retrieval by including polarization, we compare the retrieval errors between the P-type and I-type inversions in Table 5.4 for individual aerosol parameters. Also compared are the errors in the derived  $\omega_A$  and  $Asy$ . Clearly, the P-type inversion yields lower retrieval errors for all the retrieved and derived parameters; this is confirmed by the theoretical analysis in Chapter 4 of this thesis. The key points from the comparison are:

(i) Polarization measurements provide important constraints in improving the retrieval of  $V_0$ ,  $r_{eff}$ , and  $v_{eff}$  for both fine and coarse aerosol modes. For these three cases, the errors in the retrieved  $V_0$  with polarization are less than 3% for the fine mode and less than 5% for the coarse mode, representing a significant decrease from their counterparts ( $\sim 15\%$  and  $\sim 10\%$ ) in the I-type inversion. Adding polarization can also decrease the error in  $r_{eff}$  of both fine and coarse modes from 10–15% for the I-type inversion to 3% and below. Errors in  $v_{eff}$  retrieved by the P-type inversion are 9–11% for aerosol in the fine mode and 17–26% in the coarse mode, whereas they can exceed 60% with the I-type inversion.

(ii) Polarization measurements also provide useful constraints in improving the refractive index retrievals. The most significant improvement is found in the fine-mode  $m_r$ , where

Table 5.4: Errors on the retrieved and derived parameters from both types of inversion<sup>a</sup>.

$\mathbf{x}$	Case A		Case B		Case C		$\epsilon_a$
	$\hat{\epsilon}_P$	$\hat{\epsilon}_I$	$\hat{\epsilon}_P$	$\hat{\epsilon}_I$	$\hat{\epsilon}_P$	$\hat{\epsilon}_I$	
$V_0^f$	2.1%	15%	2.2%	18%	3.0%	25%	100%
$r_{\text{eff}}^f$	1.3%	9.2%	1.3%	11%	2.4%	14%	80%
$v_{\text{eff}}^f$	9.3%	33%	9.3%	38%	11%	33%	80%
$m_r^f$	0.005	0.020	0.006	0.023	0.009	0.035	0.14
$m_i^f$	0.002	0.002	0.003	0.004	0.004	0.006	0.010
$\omega_A^f$	0.009	0.010	0.016	0.018	0.021	0.037	–
$\text{Asy}^f$	0.003	0.005	0.003	0.006	0.003	0.009	–
$V_0^c$	4.8%	14%	3.2%	10%	2.9%	9.4%	100%
$r_{\text{eff}}^c$	6.7%	15%	3.3%	7.1%	1.9%	6.0%	80%
$v_{\text{eff}}^c$	26%	66%	17%	48%	10%	33%	80%
$m_r^c$	0.108	0.137	0.080	0.122	0.044	0.100	0.16
$m_i^c$	0.006	0.007	0.005	0.006	0.003	0.005	0.008
$\omega_A^c$	0.059	0.065	0.050	0.058	0.031	0.051	–
$\text{Asy}^c$	0.024	0.036	0.018	0.028	0.012	0.025	–

<sup>a</sup> $\hat{\epsilon}_P$  and  $\hat{\epsilon}_I$  are retrieval error respectively from the P-type and I-type inversions,  $\epsilon_a$  is the a priori error.

the error is lower than 0.01 for the P-type inversion, compared to 0.02–0.04 for the I-type inversion. The error in the coarse-mode  $m_r$  from P-type inversion ranges from 0.04 to 0.11, depending on the prevalence of coarse-mode particles. For retrieving  $m_i$ , the inclusion of polarization reduces the error by 10–30%, a value also depending on coarse-mode dominance.

(iii) Adding the polarization yields better estimates of the aerosol SSA and Asy for both aerosol modes. From P-type inversion, the errors in the retrieved  $\omega_A$  are lower than 0.02 for aerosols in the fine mode and 0.06 for aerosols in the coarse mode, representing a 10–40% decrease from the I-type inversion. As expected, errors in the Asy also reveal a 30–50% decrease.

## 5.6 Summary

In this chapter, we applied the new algorithm to a suite of photo-polarimetric measurements taken from the new-generation SunPhotometer at the Beijing\_RADI AERONET station. In order to demonstrate the importance of adding polarization measurements, we performed aerosol retrievals from radiance measurements only (the I-type inversion), in addition to the retrievals using both radiance and polarization measurements (the P-type inversion). We found that, for both types of inversion, the fitting errors for the AOD and sky radiance are much smaller than the calibration uncertainties (0.02 for AOD and 5% for sky radiance). Also, the fitting errors of the degree of linear polarization (DOLP) with the P-type inversion are much smaller than the calibration error ( $\sim 0.01$ ). However, the DOLP fitting errors in the I-type inversion usually exceed 0.01, and even reach 0.04 for many individual measurements in the case dominated by coarse aerosols, which highlights the necessity to include polarization in the inversion as an additional source of constraint.

Our retrieval results are generally consistent with the AERONET inversion products, but we found distinct differences between the values of the refractive index and SSA for the fine- and coarse-mode aerosols. For these three cases selected for our study, we found that the retrieved real part refractive index is about 1.5–1.6 in the coarse mode, which is higher than those for the fine mode, 1.4–1.5. Also, the coarse-mode aerosols are more absorbing than the fine-mode ones.

We also compared the retrieval error for each retrieved parameters between the I-type and P-type inversions. A comparison analysis indicates that the retrieval error can be reduced by at least 50% in PSD parameters, by 10–30% the refractive index components, and by 10–40% in the aerosol SSA. These error reductions depend on the fine/coarse-mode fraction, specifics of instrumentation, and aerosol properties. These improvements in the P-type inversion are consistent with the theoretical analysis in Chapter 4 of this thesis.

The promising results in this study are obtained from the initial development and preliminary applications of a new algorithm targeted for the retrieval of aerosol properties from new-generation AERONET measurements. Future developments will include, but not be limited to, the treatment of non-spherical large aerosol particles like mineral dust, and the consideration of tri-modal aerosols for special situations. While the bi-lognormal PSD can well represent the aerosol size spectrum in most cases, future research efforts will include the implementation of tri-modal aerosol mixtures in situations of cloud formation [Eck *et al.*, 2012] or volcanic aerosols [Eck *et al.*, 2010]. Moreover, extensive retrievals for a longer period of time will also be performed over sites where CE318-DP SunPhotometer instruments have been installed (i.e., Beijing\_RADI and Lille).

## CHAPTER 6

### CONCLUSIONS AND OUTLOOK

#### 6.1 Conclusions

Aerosols have been recognized as major components of the Earth's climate system, influencing the radiative budget, clouds, and precipitation processes. An accurate assessment of these effects requires realistic representation of the aerosol loading and distribution across the globe, as well as the characteristics of the aerosol particle size distribution and chemical composition (refractive index).

The objective of this thesis is to contribute an improved research algorithm retrieving aerosol microphysical properties from AERONET measurements of light radiance and polarization, with emphasis on elucidating the potentially important role of polarization measurements. As outlined in section 1.2, specific investigations towards this research goal are: the development of an retrieval algorithm that integrates a rigorous radiative transfer model (Chapter 2) and statistical optimized inversion (Chapter 3), the examination of potential aerosol information contained in the AERONET polarization measurements (Chapter 4), and the application of our designed inversion algorithm to the real AERONET measurements (Chapter 5). Below, I briefly summarize the contributions of this thesis by these three investigations.



### 6.1.1 UNL-VRM and new AERONET inversion algorithm

The UNified Linearized Vector Radiative Transfer Model, or UNL-VRM integrates the linearized codes computing vector radiative transfer (VLIDORT) and scattering of spherical (LMIE) and non-spherical (LTMATRIX) particles, hyperspectral treatment for air molecular scattering and gaseous absorption, and models describing bidirectional surface reflectance and polarization (BRDF/BPDF). As shown in Chapter 2, the direct coupling of these components by UNL-VRM allows it not only able to compute the four Stokes parameters and degree of linear polarization (DOLP) with high accuracy and high spectral resolution, but also to simultaneously and analytically generate sensitivities of these Stokes parameters with respect to aerosol parameters of both the fine and coarse modes. By inclusion of HITRAN and other molecular spectroscopy data for atmospheric trace gases, the UNL-VRM is also able to perform line-by-line calculation of gas absorption, thus providing another opportunity for the future study of the effect of absorbing gases (such as  $\text{SO}_2$ ,  $\text{NO}_2$ ,  $\text{O}_3$ , and water vapor) on the aerosol retrieval. Although the UNL-VRM is used to simulate the AERONET measurements in this work, the module-based structure of UNL-VRM allows a broad application to the remote sensing observations from other platforms.

In Chapter 3, I have presented a new algorithm to retrieve both fine- and coarse-mode aerosol properties from multi-spectral and multi-angular solar polarimetric radiation fields measured by AERONET including additional spectra of polarization observations. The retrieval algorithm uses UNL-VRM and incorporates the statistical optimized inversion to retrieve aerosol parameters pertaining to a bi-lognormal particle size distribution (PSD), including the aerosol volume concentration, effective radius and variance, and complex indices of refraction. While the new algorithm has heritage from the existing AERONET inversion algorithm in using multiple a priori constraints, it is different from the existing AERONET algorithm in that: (a) a bi-modal lognormal PSD (instead of 22 size bins) is

assumed; (b) the spectral refractive indices are retrievable for both fine and coarse modes. The mode-separated aerosol microphysical and optical retrievals can benefit the analysis for aerosol chemical compositions and climate radiative impacts study of aerosol, and most importantly, can thereby facilitate the evaluation of atmospheric chemistry models and the validation of aerosol products from satellite sensors with polarization capability.

### 6.1.2 Potential information contained in AERONET polarization

In Chapter 4, I have examined the potential microphysical aerosol information contained in the AERONET photo-polarimetric observations. The analysis focused on how the added polarization measurements impact on the retrieval accuracy the in aerosol particle size distribution, spectral refractive index, and single scattering albedo. We used the UNL-VRM to generate the synthetic AERONET spectral radiance and DOLP, as well as their sensitivities with respect to these aerosol properties. Then, we quantify the aerosol information content in various observation scenarios in terms of degree of freedom for signal (DFS) and *a posteriori* error.

The results show a remarkable increase in information by adding additional polarization and/or radiances into the inversion: an overall increase of 2–5 of DFS comparing with radiance-only measurements. Correspondingly, smallest retrieval errors are found in the added-polarization scenario: 2.3% (2.9%) for the fine-mode (coarse-mode) aerosol volume concentration, 1.3% (3.5%) for the effective radius, 7.2% (12%) for the effective variance, 0.005 (0.035) for the real part refractive index, and 0.019 (0.068) for the single scattering albedo. These errors represent a reduction from their counterparts in the radiance-only scenario of 79% (57%), 76% (49%), 69% (52%), 66% (46%), and 49% (20%), respectively.

We have further investigated those retrieval errors over a variety of aerosol loading and fine/coarse-mode prevalence (section 4.4), which indicates that the combined use of radiance

and polarization observations can yield the retrieval of refractive index and single scattering albedo for both fine and coarse aerosol modes, when AOD at 440 nm is larger than 0.2 and 870/1020-nm Ångström exponent ranges between 0.7 and 1.6.

### 6.1.3 Application to real retrieval

In Chapter 5, we have applied our new AERONET inversion algorithm to a suite of real cases over Beijing\_RADI site. We found that our retrievals are overall consistent with AERONET operational inversions, but can offer mode-resolved refractive index and SSA with acceptable accuracy for the aerosol composed by spherical particles. Along with the retrieval using both radiance and polarization, we also performed radiance-only retrieval to demonstrate the improvements by adding polarization in the inversion. Contrast analysis indicates that with polarization, retrieval error can be reduced by over 50% in PSD parameters, 10–30% in the refractive index, and 10–40% in SSA, which is consistent with theoretical analysis presented in Chapter 4.

## 6.2 Outlook and Future Work

The promising results in this study are obtained from the initial development and preliminary applications of a new algorithm targeted for the retrieval of aerosol properties from new-generation AERONET measurements. Future developments will include, but not be limited to, the treatment of non-spherical large aerosol particles like mineral dust, and the consideration of tri-modal aerosols for special situations. Another interesting research topic is to investigate the chemical composition from the multi-spectral and multi-angular photo-polarimetric measurements. Below, I list particularly promising directions for future investigations.

1. Implement the consideration of non-spherical dust.
2. While the bi-lognormal PSD can well represent the aerosol size spectrum in most cases, future research efforts will include the implementation of tri-modal aerosol mixtures in situations of cloud formation [[Eck et al., 2012](#)] or volcanic aerosols [[Eck et al., 2010](#)].
3. Explore the potential use of multi-spectral and multi-angular photo-polarimetric measurements for aerosol chemical composition. This will benefit the source identification of species-specified aerosols.
4. Last but not least, extensive retrievals for a longer period of time will also be performed over sites where CE318-DP SunPhotometer instruments have been installed (i.e., Beijing\_RADI and Lille). Such long-term retrieval will provide more robust resources for studying the aerosol climatology.

## APPENDIX A

### ABBREVIATIONS AND ACRONYMS

AE	Ångström Exponent
AOD	Aerosol Optical Depth
BRDF	Bidirectional Reflectance Distribution Function

## APPENDIX B

### SYMBOLS

- A** Averaging kernel matrix
- B<sup>j</sup>** Greek matrix, or the coefficients of phase matrix expansion

## APPENDIX C

### DERIVATIONS OF TRANSFORMATION VECTOR $\Pi$

Let  $x$  be an aerosol microphysical parameter. The aerosol extinction and scattering optical thickness ( $\tau_A$  and  $\delta_A$ ), single scattering albedo ( $\omega_A$ ), and Greek coefficient matrix ( $\mathbf{B}_A^j$ ) are functions of  $x$ . However, the gaseous absorption and Rayleigh scattering parameters are independent of  $x$ . This appendix outlines the derivations of equations (2.19) and (2.21) and the expressions in Table 2.1 and Table 2.2.

First, we transform equation (2.18) as below:

$$\phi_x = \frac{x}{\tau} \frac{\partial \tau}{\partial x} = \frac{x}{\tau} \frac{\partial (\tau_G + \tau_R + \tau_A)}{\partial x} = \frac{1}{\tau} x \frac{\partial \tau_A}{\partial x} \quad (\text{C.1})$$

$$\begin{aligned} \phi_x &= \frac{x}{\omega} \frac{\partial \omega}{\partial x} = \frac{x}{\omega} \frac{[(\delta_A + \tau_G)]}{\partial x} \\ &= \frac{x}{\omega} \frac{1}{\tau^2} \left[ \tau \frac{\partial (\delta_A + \tau_R)}{\partial x} - (\delta_A + \tau_R) \frac{\partial \tau}{\partial x} \right] \\ &= \frac{x}{\omega \tau} \frac{\partial \delta_A}{\partial x} - (\delta_A + \tau_R) \frac{x}{\omega \tau^2} \frac{\partial \tau_A}{\partial x} \\ &= \frac{x}{\delta_A + \tau_R} \frac{\partial \delta_A}{\partial x} - \frac{1}{\tau} \frac{\partial \tau_A}{\partial x} \\ &= \frac{x}{\delta_A + \tau_R} \frac{\partial \delta_A}{\partial x} - \phi_x \end{aligned} \quad (\text{C.2})$$

$$\Psi_x^j = \frac{x}{\mathbf{B}^j} \frac{\partial \mathbf{B}^j}{\partial x} = \frac{x}{\mathbf{B}^j} \frac{\partial [(\tau_R \mathbf{B}_R^j + \delta_A \mathbf{B}_A^j) / (\delta_A + \tau_R)]}{\partial x}$$

$$\begin{aligned}
&= \frac{x}{\mathbf{B}^j} \frac{1}{(\delta_A + \tau_R)^2} \left[ (\delta_A + \tau_R) \frac{\partial(\delta_A \mathbf{B}_A^j)}{\partial x} - (\tau_R \mathbf{B}_R^j + \delta_A \mathbf{B}_A^j) \frac{\partial \delta_A}{\partial x} \right] \\
&= \frac{x}{\mathbf{B}^j} \frac{1}{\delta_A + \tau_R} \left[ \frac{\partial(\delta_A \mathbf{B}_A^j)}{\partial x} - \mathbf{B}^j \frac{\partial \delta_A}{\partial x} \right] \\
&= \frac{1}{(\delta_A + \tau_R) \mathbf{B}^j} \left[ \delta_A x \frac{\mathbf{B}_A^j}{\partial x} + (\mathbf{B}_A^j - \mathbf{B}^j)_x \frac{\partial \delta_A}{\partial x} \right] \tag{C.3}
\end{aligned}$$

These expressions are linear combinations of  $\phi'_x$ ,  $\varphi'_x$ , and  $\Psi_x'^j$  (as defined by equation (2.20)), where

$$\left[ \phi'_x, \varphi'_x, \langle \Psi_x'^j \rangle_{j=1,J} \right]^T = \left[ x \frac{\partial \tau_A}{\partial x}, x \frac{\partial \delta_A}{\partial x}, \left\langle x \frac{\partial \mathbf{B}_A^j}{\partial x} \right\rangle_{j=1,J} \right]^T \tag{C.4}$$

We then can write above equations (C.1)–(C.3) into vector formulism (as equation (2.19):

$$\left[ \phi_x, \varphi_x, \langle \Psi_x^j \rangle_{j=1,J} \right]^T = \mathbf{\Pi} \left[ \phi'_x, \varphi'_x, \langle \Psi_x'^j \rangle_{j=1,J} \right]^T \tag{C.5}$$

where  $\mathbf{\Pi}$  is a matrix comprising the relevant coefficients, as noted in equation (2.21). Equations (C.5) and (2.21) then act as a universal formulation for preparing linearized inputs of optical property for VLIDORT. Computation of  $\left[ \phi_x, \varphi_x, \langle \Psi_x^j \rangle_{j=1,J} \right]$  can then be achieved by the calculation of  $\left[ \phi'_x, \varphi'_x, \langle \Psi_x'^j \rangle_{j=1,J} \right]$  for a given parameter  $x$ .

Let us first consider the derivation of  $\left[ \phi'_x, \varphi'_x, \langle \Psi_x'^j \rangle_{j=1,J} \right]$  for certain aerosol optical properties in a given atmospheric layer, i.e.,  $\tau_A$ ,  $\omega_A$ , and  $\beta_A^k$ , where  $\beta_A^k$  indicates one of the elements in the  $k$ th aerosol scattering Greek matrix  $\mathbf{B}_A^k$ .

For  $x = \tau_A$ , we have

$$\phi'_x = \tau_A \frac{\partial \tau_A}{\partial \tau_A} = \tau_A \tag{C.6}$$



$$\phi'_x = \tau_A \frac{\partial \delta_A}{\partial \tau_A} = \tau_A \omega_A \quad (\text{C.7})$$

$$\Psi'^j_x = \tau_A \frac{\partial \mathbf{B}^j_A}{\partial \tau_A} = \mathbf{0} \quad (\text{C.8})$$

For  $x = \omega_A$ , we have

$$\phi'_x = \omega_A \frac{\partial \tau_A}{\partial \omega_A} = 0 \quad (\text{C.9})$$

$$\phi'_x = \omega_A \frac{\partial \delta_A}{\partial \omega_A} = \omega_A \tau_A \quad (\text{C.10})$$

$$\Psi'^j_x = \omega_A \frac{\partial \mathbf{B}^j_A}{\partial \omega_A} = \mathbf{0} \quad (\text{C.11})$$

For  $x = \beta_A^k$ , we have

$$\phi'_x = \beta_A^k \frac{\partial \tau_A}{\partial \beta_A^k} = 0 \quad (\text{C.12})$$

$$\phi'_x = \beta_A^k \frac{\partial \delta_A}{\partial \beta_A^k} = 0 \quad (\text{C.13})$$

$$\Psi'^j_x = \beta_A^k \frac{\partial \mathbf{B}^j_A}{\partial \beta_A^k} = \begin{cases} \frac{\delta_A \beta_A^k}{\beta^k} & \text{if } j = k \\ 0 & \text{if } j \neq k \end{cases} \quad (\text{C.14})$$

Expressions in Table 2.1 are then derived by substituting equations (C.6)–(C.14) into equation (C.5).

The UNL-VRM integrates the VLIDORT with linearized Mie/T-matrix codes, and this combination allows us to generate Stokes vectors and associated analytical Jacobians with respect to aerosol microphysical parameters for two aerosol modes. Thus, we must supply the  $\left[ \phi'_x, \phi'_x, \left\langle \Psi'^j_x \right\rangle_{j=1,J} \right]$  quantities for all such parameters. We give an example here, assuming that the aerosols are bimodal, with two lognormal size distributions described by geometric standard deviations ( $\sigma_g^f$  and  $\sigma_g^c$ ), geometric median radii ( $r_g^f$  and  $r_g^c$ ), and non-sphericity

parameters ( $\varepsilon^f$  and  $\varepsilon^c$ ) for the fine and coarse modes. We note that  $\varepsilon$  is available only when non-spherical particles are assumed (T-matrix code is applied). Complex refractive indices are  $m_r^f - m_i^f i$  and  $m_r^c - m_i^c i$ . Given these microphysical properties, the linearized Mie/T-matrix codes will compute for each mode the scattering and extinction efficiencies ( $Q_{\text{sca}}$  and  $Q_{\text{ext}}$ ), the set of expansion coefficients ( $\mathbf{B}_A^j$ ) of scattering phase matrix, as well as the derivatives of these quantities with respect to these microphysical properties. For a wide size range of aerosol particles, which enable am about 100% accumulated value for the bi-lognormal probability function, the optical thickness for aerosol extinction and scattering and the associated Greek matrix coefficients within for one atmospheric layer can be calculated through

$$\tau_A = \tau_A^f + \tau_A^c = \frac{3V_0^f Q_{\text{ext}}^f}{4r_{\text{eff}}^f} + \frac{3V_0^c Q_{\text{ext}}^c}{4r_{\text{eff}}^c} \quad (\text{C.15})$$

$$\delta_A = \delta_A^f + \delta_A^c = \frac{3V_0^f Q_{\text{sca}}^f}{4r_{\text{eff}}^f} + \frac{3V_0^c Q_{\text{sca}}^c}{4r_{\text{eff}}^c} \quad (\text{C.16})$$

$$\mathbf{B}_A^j = \frac{\delta_A^f \mathbf{B}_A^{fj} + \delta_A^c \mathbf{B}_A^{cj}}{\delta_A^f + \delta_A^c} \quad (\text{C.17})$$

We can compute vector  $\left[ \phi'_x, \varphi'_x, \langle \Psi_x'^j \rangle_{j=1,J} \right]$  for a given parameter by differentiating above equations (C.15)–(C.17). For  $x = V_0^f$  as an example:

$$\phi'_x = V_0^f \frac{\partial \tau_A}{\partial V_0^f} = V_0^f \frac{3Q_{\text{ext}}^f}{4r_{\text{eff}}^f} = \tau_A^f \quad (\text{C.18})$$

$$\varphi'_x = V_0^f \frac{\partial \delta_A}{\partial V_0^f} = V_0^f \frac{3Q_{\text{sca}}^f}{4r_{\text{eff}}^f} = \delta_A^f \quad (\text{C.19})$$

$$\Psi_x'^j = V_0^f \frac{\partial \mathbf{B}_A^j}{\partial V_0^f} = \frac{\delta_A^f}{\delta_A} (\mathbf{B}_A^{fj} - \mathbf{B}_A^j) \quad (\text{C.20})$$

And similarly for  $x = r_g^f$ , we have

$$\phi'_x = \tau_A^f \left( \frac{r_g^f}{Q_{\text{ext}}^f} \frac{\partial Q_{\text{ext}}^f}{\partial r_g^f} - \frac{r_g^f}{r_{\text{eff}}^f} \frac{\partial r_{\text{eff}}^f}{\partial r_g^f} \right) \quad (\text{C.21})$$

$$\phi'_x = \delta_A^f \left( \frac{r_g^f}{Q_{\text{sca}}^f} \frac{\partial Q_{\text{sca}}^f}{\partial r_g^f} - \frac{r_g^f}{r_{\text{eff}}^f} \frac{\partial r_{\text{eff}}^f}{\partial r_g^f} \right) \quad (\text{C.22})$$

$$\Psi_x'^j = \frac{\phi'_x}{\delta_A} (\mathbf{B}_A^{f,j} - \mathbf{B}_A^j) + r_g^f \frac{\partial \mathbf{B}_A^{s,j}}{\partial r_g^f} \quad (\text{C.23})$$

In a similar fashion, we can obtain the vector  $\left[ \phi'_x, \phi'_x, \langle \Psi_x'^j \rangle_{j=1,J} \right]$  for other fine-mode aerosol parameters including  $\tau_A^f$ ,  $\omega_A^f$ ,  $V_0^f$ ,  $m_r^f$ ,  $m_1^f$ ,  $r_g^f$ ,  $\sigma_g^f$ , and  $\varepsilon^f$  (as listed in Table 2.2). For coarse-mode aerosol parameters, the derivations are the same with superscript ‘s’ replaced by ‘c’.

We have implemented various aerosol-loading vertical profiles into the testbed, including uniform, exponential-decreasing, and quasi-Gaussian profile shapes. For the uniform profile, aerosols are assumed evenly distributed with height. The layer AOD for the exponential-decreasing profile follows form

$$\int_{+\infty}^z \tau_A(z) dz = \tau_{a0} \exp\left(-\frac{z}{H}\right) \quad (\text{C.24})$$

where  $\tau_{a0}$  is the columnar AOD, and  $H$  is a scale height parameter. The quasi-Gaussian profile is derived from a generalized distribution function [Spurr and Christi, 2014]

$$\tau_A(z) = K \frac{\exp(-\gamma|z - z_{\text{peak}}|)}{[1 + \exp(-\gamma|z - z_{\text{peak}}|)]^2} \quad (\text{C.25})$$

where  $K$  is a constant related to  $\tau_{a0}$ ,  $\gamma$  is related to half-width constant, and  $z_{\text{peak}}$  is the height having peak loading. Derivatives of layer aerosol optical thickness with respect to these profile parameters ( $H$ ,  $\gamma$ , and  $z_{\text{peak}}$ ) are also included in order to calculate Jacobians of Stokes

vector to these parameters, and the vectors  $\left[ \phi'_x, \phi'_x, \left\langle \Psi'^j_x \right\rangle_{j=1,J} \right]$  for these derivatives are also shown in Table 2.2.

## APPENDIX D

### **LIST OF PUBLICATIONS GENERATED DURING PHD STUDY**

## REFERENCES

- Bodhaine, B. A., N. B. Wood, E. G. Dutton, and J. R. Slusser (1999), On rayleigh optical depth calculations, *Journal of Atmospheric and Oceanic Technology*, 16(11), 1854–1861. [2.2.1](#)
- Boesche, E., P. Stammes, T. Ruhtz, R. Preusker, and J. Fischer (2006), Effect of aerosol microphysical properties on polarization of skylight: sensitivity study and measurements, *Appl. Opt.*, 45(34), 8790–8805. [4.1](#)
- Boucher, O., et al. (2013), *Clouds and Aerosols. In Climate Change 2013: The Physical Science Basis. Contribution of Working Group I to the Fifth Assessment Report of the Intergovernmental Panel on Climate Change [Stocker T.F., et al. (eds.)]*, p. 571–658, Cambridge University Press, Cambridge, United Kingdom and New York, NY, USA. [1.1](#)
- Byrd, R. H., P. Lu, J. Nocedal, and C. Zhu (1995), A limited memory algorithm for bound constrained optimization, *SIAM Journal on Scientific Computing*, 16, 1190–1208. [3.3.3](#)
- Cairns, B., B. E. Carlson, A. A. Lacis, and E. E. Russell (1997), *An analysis of ground-based polarimetric sky radiance measurements*, p. 383–393, Proc. SPIE. [4.1](#)
- Chin, M., et al. (2002), Tropospheric aerosol optical thickness from the gocart model and comparisons with satellite and sun photometer measurements, *Journal of the Atmospheric Sciences*, 59(3), 461–483. [1.1.3](#)
- Chowdhary, J., B. Cairns, M. Mishchenko, and L. Travis (2001), Retrieval of aerosol properties over the ocean using multispectral and multiangle photopolarimetric measurements from the research scanning polarimeter, *Geophysical Research Letters*, 28(2), 243–246. [1.1.3](#)
- Chowdhary, J., B. Cairns, and L. D. Travis (2002), Case studies of aerosol retrievals over the ocean from multiangle, multispectral photopolarimetric remote sensing data, *Journal of the Atmospheric Sciences*, 59(3), 383–397. [1.1.3](#)

- Chowdhary, J., B. Cairns, M. I. Mishchenko, P. V. Hobbs, G. F. Cota, J. Redemann, K. Rutledge, B. N. Holben, and E. Russell (2005), Retrieval of aerosol scattering and absorption properties from photopolarimetric observations over the ocean during the clams experiment, *Journal of the Atmospheric Sciences*, 62(4), 1093–1117. [1.1.3](#)
- Coulson, A. (1988), *Polarization and intensity of light in the atmosphere*, VA A Deepak Pub, Hampton. [\(document\)](#), [2.3](#), [2.3](#)
- Coulson, K., J. Dave, and Z. Sekera (1960), *Tables related to radiation emerging from a planetary atmosphere With Rayleigh scattering*, Univ California Press, Berkeley, CA. [\(document\)](#), [2.3](#), [2.3](#)
- Cox, C., and W. Munk (1954), Measurement of the roughness of the sea surface from photographs of the sun's glitter, *Journal of the Optical Society of America*, 44(11), 838–850. [2.2.3](#)
- Curcio, J. (1961), Evaluation of atmospheric aerosol particle size distribution from scattering measurements in the visible and infrared, *Journal of the Optical Society of America*, 51(5), 548–551. [1.1.1](#)
- Dave, J. V. (1971), Determination of size distribution of spherical polydispersions using scattered radiation data, *Applied Optics*, 10(9), 2035–2044. [1.1.1](#)
- de Rooij, W. A., and C. C. A. H. v. d. Stap (1984), Expansion of mie scattering matrices in generalized spherical functions, *Astronomy and Astrophysics*, 131(2), 237–248. [2.2.2](#)
- Deuzé, J. L., F. M. Bréon, P. Y. Deschamps, C. Devaux, M. Herman, A. Podaire, and J. L. Roujean (1993), Analysis of the polder (polarization and directionality of earth's reflectances) airborne instrument observations over land surfaces, *Remote Sensing of Environment*, 45(2), 137–154. [1.1.3](#)
- Deuzé, J. L., et al. (2001), Remote sensing of aerosols over land surfaces from polder-aerosol polarized measurements, *Journal of Geophysical Research: Atmospheres*, 106(D5), 4913–4926. [1.1.3](#)
- Diner, D. J., et al. (1998), Multi-angle imaging spectroradiometer (misr) instrument description and experiment overview, *Geoscience and Remote Sensing, IEEE Transactions on*, 36(4), 1072–1087. [1.1.3](#)

- Ding, S., J. Wang, X. Xu, and R. Spurr (2014), Retrieval of optical depth and vertical distribution of atmospheric aerosols from light intensity and polarization in o2a and o2b bands, in *2014 AGU Fall Meeting*. [2.2](#)
- Drury, E., et al. (2010), Synthesis of satellite (modis), aircraft (icartt), and surface (improve, epa-aqs, aeronet) aerosol observations over eastern north america to improve modis aerosol retrievals and constrain surface aerosol concentrations and sources, *J. Geophys. Res.*, *115*(D14), D14,204. [1.1.3](#), [4.2.1](#)
- Dubovik, O. (2004), *Optimization of Numerical Inversion in Photopolarimetric Remote Sensing*, *NATO Science Series II: Mathematics, Physics and Chemistry*, vol. 161, book section 3, pp. 65–106, Springer Netherlands. [3.3.3](#), [4.3.1](#)
- Dubovik, O., and M. D. King (2000), A flexible inversion algorithm for retrieval of aerosol optical properties from sun and sky radiance measurements, *J. Geophys. Res.*, *105*(D16), 20,673–20,696. [1.1.1](#), [1.1.2](#), [3.3.2](#), [3.3.2](#), [3.3.2](#), [3.3.3](#)
- Dubovik, O., A. Smirnov, B. N. Holben, M. D. King, Y. J. Kaufman, T. F. Eck, and I. Slutsker (2000), Accuracy assessments of aerosol optical properties retrieved from aerosol robotic network (aeronet) sun and sky radiance measurements, *Journal of Geophysical Research*, *105*(D8), 9791–9806. [1.1.2](#), [1.1.3](#), [4.4](#), [4.4](#)
- Dubovik, O., B. N. Holben, T. Lapyonok, A. Sinyuk, M. I. Mishchenko, P. Yang, and I. Slutsker (2002a), Non-spherical aerosol retrieval method employing light scattering by spheroids, *Geophysical Research Letters*, *29*(10). [1.1.1](#)
- Dubovik, O., B. Holben, T. F. Eck, A. Smirnov, Y. J. Kaufman, M. D. King, D. Tanre, and I. Slutsker (2002b), Variability of absorption and optical properties of key aerosol types observed in worldwide locations, *Journal of the Atmospheric Sciences*, *59*(3), 590–608. [1.1.3](#)
- Dubovik, O., et al. (2006), Application of spheroid models to account for aerosol particle nonsphericity in remote sensing of desert dust, *Journal of Geophysical Research: Atmospheres*, *111*, D11,208. [1.1.1](#), [1.1.2](#), [1.1.3](#), [4.1](#)
- Dubovik, O., M. Herman, A. Holdak, T. Lapyonok, D. Tanre, J. L. Deuze, F. Ducos, A. Sinyuk, and A. Lopatin (2011), Statistically optimized inversion algorithm for enhanced retrieval of aerosol properties from spectral multi-angle polarimetric satellite observations, *Atmos. Meas. Tech.*, *4*(5), 975–1018, aMT. [2.2.3](#)



- Eck, T. F., et al. (2010), Climatological aspects of the optical properties of fine/coarse mode aerosol mixtures, *Journal of Geophysical Research: Atmospheres*, 115(D19), D19,205. [5.6](#), [2](#)
- Eck, T. F., et al. (2012), Fog- and cloud-induced aerosol modification observed by the aerosol robotic network (aeronet), *Journal of Geophysical Research: Atmospheres*, 117(D7), D07,206. [5.6](#), [2](#)
- Emde, C., R. Buras, B. Mayer, and M. Blumthaler (2010), The impact of aerosols on polarized sky radiance: model development, validation, and applications, *Atmos. Chem. Phys.*, 10(2), 383–396, aCP. [4.1](#)
- Evans, K. F., and G. L. Stephens (1991), A new polarized atmospheric radiative transfer model, *Journal of Quantitative Spectroscopy and Radiative Transfer*, 46(5), 413–423, doi: DOI: 10.1016/0022-4073(91)90043-P. [2.3](#)
- Frankenberg, C., O. Hasekamp, C. O'Dell, S. Sanghavi, A. Butz, and J. Worden (2012), Aerosol information content analysis of multi-angle high spectral resolution measurements and its benefit for high accuracy greenhouse gas retrievals, *Atmos. Meas. Tech.*, 5(7), 1809–1821, aMT. [3.2.2](#)
- Garcia, R. D. M., and C. E. Siewert (1989), The fn method for radiative transfer models that include polarization effects, *Journal of Quantitative Spectroscopy and Radiative Transfer*, 41(2), 117–145, doi: DOI: 10.1016/0022-4073(89)90133-7. ([document](#)), [2.4](#), [2.3](#)
- Grassl, H. (1971), Determination of aerosol size distributions from spectral attenuation measurements, *Applied Optics*, 10(11), 2534–2538. [1.1.1](#)
- Halothore, R. N., T. F. Eck, B. N. Holben, and B. L. Markham (1997), Sun photometric measurements of atmospheric water vapor column abundance in the 940-nm band, *Journal of Geophysical Research: Atmospheres*, 102(D4), 4343–4352. [2.2.1](#)
- Han, D., J. Wang, X. Xu, W. Hou, and L. Chen (2014), Application of gosat tanso-cai observations for aerosol optical depth retrieval and surface pm2.5 air quality monitoring, in *2014 AGU Fall Meeting*. [2.2](#)
- Hansen, J. E., and L. D. Travis (1974), Light scattering in planetary atmospheres, *Space Sci. Rev.*, 16, 572–610. [1.1.1](#), [1.1.3](#), [2.1](#), [2.2.1](#), [3.3.1](#), [4.1](#), [4.3.1](#), [4.3.2.3](#)

- Hansen, P. C. (1998), *Rank-Deficient and Discrete Ill-Posed Problems: Numerical Aspects of Linear Inversion*, Soc. for Ind. and Appl. Math., Philadelphia, Pa. [3.3.3](#)
- Hasekamp, O. P., and J. Landgraf (2005a), Retrieval of aerosol properties over the ocean from multispectral single-viewing-angle measurements of intensity and polarization: Retrieval approach, information content, and sensitivity study, *J. Geophys. Res.*, *110*(D20), D20,207. [3.2.2](#), [3.3.1](#)
- Hasekamp, O. P., and J. Landgraf (2007), Retrieval of aerosol properties over land surfaces: capabilities of multiple-viewing-angle intensity and polarization measurements, *Applied Optics*, *46*(16), 3332–3344. [3.3.1](#)
- Hasekamp, O. P., P. Litvinov, and A. Butz (2011), Aerosol properties over the ocean from parasol multiangle photopolarimetric measurements, *Journal of Geophysical Research: Atmospheres*, *116*(D14), D14,204. [1.1.3](#)
- Haywood, J., and O. Boucher (2000), Estimates of the direct and indirect radiative forcing due to tropospheric aerosols: A review, *Rev. Geophys.*, *38*(4), 513–543. [1.1](#)
- Herman, B. M., S. R. Browning, and J. A. Reagan (1971), Determination of aerosol size distributions from lidar measurements, *Journal of the Atmospheric Sciences*, *28*(5), 763–771. [1.1.1](#)
- Hess, M., P. Koepke, and I. Schult (1998), Optical properties of aerosols and clouds: The software package opac, *Bulletin of the American Meteorological Society*, *79*(5), 831–844. [\(document\)](#), [2.5](#), [4.2.1](#)
- Holben, B. N., et al. (1998), Aeronet - a federated instrument network and data archive for aerosol characterization, *Remote Sensing of Environment*, *66*(1), 1–16. [1.1](#), [1.1.1](#), [1.1.2](#), [4.2.2](#)
- Holben, B. N., T. F. Eck, I. Slutsker, A. Smirnov, A. Sinyuk, J. Schafer, D. Giles, and O. Dubovik (2006), Aeronet's version 2.0 quality assurance criteria, *Proc. SPIE 6408, Remote Sensing of the Atmosphere and Clouds*, 64080Q, 10.1117/12.706524. [1.1.3](#), [3.3.5](#), [4.4](#)
- Hou, W., J. Wang, X. Xu, S. Ding, D. Han, J. Leitch, T. Delker, and G. Chen (2014), An algorithm for simultaneous inversion of aerosol properties and surface reflectance from airborne geotaso hyperspectral data, in *2014 AGU Fall Meeting*. [2.2](#)

- Hovenier, J., C. v. d. Mee, and H. Domke (2004), *Transfer Of Polarized Light In Planetary Atmospheres*, 258 pp., Kluwer Academic Publishers, Dordrecht, The Netherlands. [2.1](#)
- Kahn, R. A., B. J. Gaitley, M. J. Garay, D. J. Diner, T. F. Eck, A. Smirnov, and B. N. Holben (2010), Multiangle imaging spectroradiometer global aerosol product assessment by comparison with the aerosol robotic network, *J. Geophys. Res.*, *115*(D23), D23,209. [1.1.3](#)
- Kaufman, Y. J., A. Gitelson, A. Karnieli, E. Ganor, R. S. Fraser, T. Nakajima, S. Mattoo, and B. N. Holben (1994), Size distribution and scattering phase function of aerosol particles retrieved from sky brightness measurements, *Journal of Geophysical Research: Atmospheres*, *99*(D5), 10,341–10,356. [1.1.1](#)
- Kaufman, Y. J., D. Tanré, L. A. Remer, E. F. Vermote, A. Chu, and B. N. Holben (1997), Operational remote sensing of tropospheric aerosol over land from eos moderate resolution imaging spectroradiometer, *Journal of Geophysical Research: Atmospheres*, *102*(D14), 17,051–17,067. [1.1.3](#)
- Kaufman, Y. J., D. Tanre, and O. Boucher (2002), A satellite view of aerosols in the climate system, *Nature*, *419*, 215 – 223. [1.1](#)
- King, M. D., D. M. Byrne, B. M. Herman, and J. A. Reagan (1978), Aerosol size distributions obtained by inversions of spectral optical depth measurements, *Journal of the Atmospheric Sciences*, *35*(11), 2153–2167. [1.1.1](#)
- Knobelspiesse, K., B. Cairns, M. Mishchenko, J. Chowdhary, K. Tsigaridis, B. van Dieden-hoven, W. Martin, M. Ottaviani, and M. Alexandrov (2012), Analysis of fine-mode aerosol retrieval capabilities by different passive remote sensing instrument designs, *Optics Express*, *20*(19), 21,457–21,484. [3.2.2](#), [4.4](#)
- Levelt, P. F., E. Hilsenrath, G. W. Leppelmeier, G. H. J. van den Oord, P. K. Bhartia, J. Tamminen, J. F. de Haan, and J. P. Veefkind (2006), Science objectives of the ozone monitoring instrument, *Geoscience and Remote Sensing, IEEE Transactions on*, *44*(5), 1199–1208. [2.2.1](#)
- Levy, R. C., L. A. Remer, and O. Dubovik (2007a), Global aerosol optical properties and application to moderate resolution imaging spectroradiometer aerosol retrieval over land, *Journal of Geophysical Research: Atmospheres*, *112*(D13), D13,210. [1.1.3](#)

- Levy, R. C., L. A. Remer, S. Mattoo, E. F. Vermote, and Y. J. Kaufman (2007b), Second-generation operational algorithm: Retrieval of aerosol properties over land from inversion of moderate resolution imaging spectroradiometer spectral reflectance, *J. Geophys. Res.*, *112*(D13), D13,211. [1.1.3](#)
- Levy, R. C., L. A. Remer, R. G. Kleidman, S. Mattoo, C. Ichoku, R. Kahn, and T. F. Eck (2010), Global evaluation of the collection 5 modis dark-target aerosol products over land, *Atmos. Chem. Phys.*, *10*(21), 10,399–10,420, aCP. [1.1.3](#)
- Li, Z., L. Blarel, T. Podvin, P. Goloub, J.-P. Buis, and J.-P. Morel (2008), Transferring the calibration of direct solar irradiance to diffuse-sky radiance measurements for cimel sun-sky radiometers, *Appl. Opt.*, *47*(10), 1368–1377. [5.2](#)
- Li, Z., et al. (2009), Improvements for ground-based remote sensing of atmospheric aerosol properties by additional polarimetric measurements, *Journal of Quantitative Spectroscopy and Radiative Transfer*, *110*(17), 1954–1961. [1.1.2](#), [1.1.3](#), [4.1](#), [4.2.2](#), [5.4](#), [5.4](#)
- Li, Z., L. Blarel, T. Podvin, P. Goloub, and L. Chen (2010), Calibration of the degree of linear polarization measurement of polarized radiometer using solar light, *Appl. Opt.*, *49*(8), 1249–1256. [5.2](#)
- Liou, K. N. (2002), *An Introduction to Atmospheric Radiation*, 583 pp., Academic Press, San Diego, CA, USA, volume 84 doi: DOI: 10.1016/S0074-6142(02)80015-8. [2.2.1](#)
- Litvinov, P., O. Hasekamp, and B. Cairns (2011), Models for surface reflection of radiance and polarized radiance: Comparison with airborne multi-angle photopolarimetric measurements and implications for modeling top-of-atmosphere measurements, *Remote Sensing of Environment*, *115*(2), 781–792. [2.2.3](#)
- Lucht, W., C. B. Schaaf, and A. H. Strahler (2000), An algorithm for the retrieval of albedo from space using semiempirical brdf models, *Geoscience and Remote Sensing, IEEE Transactions on*, *38*(2), 977–998. [2.2.3](#), [2.2.3](#)
- Maignan, F., F. M. Bréon, and R. Lacaze (2004), Bidirectional reflectance of earth targets: evaluation of analytical models using a large set of spaceborne measurements with emphasis on the hot spot, *Remote Sensing of Environment*, *90*(2), 210–220. [2.2.3](#)

- Maignan, F., F.-M. Bréon, E. Fédèle, and M. Bouvier (2009), Polarized reflectances of natural surfaces: Spaceborne measurements and analytical modeling, *Remote Sensing of Environment*, 113(12), 2642–2650. [2.2.3](#), [2.2.3](#), [2.2.3](#)
- Martonchik, J. V., R. A. Kahn, and D. J. Diner (2009), *Retrieval of aerosol properties over land using MISR observations*, Springer, Berlin. [1.1.3](#)
- McClatchey, R. A., R. W. Fenn, J. E. A. Selby, F. E. Volz, and J. S. Garing (1972), Optical properties of the atmosphere (third edition), *Report*, Air Force Cambridge Research Labs Hanscom AFB MA. ([document](#)), [2.2](#), [2.2](#)
- Mishchenko, M. I., and L. D. Travis (1997), Satellite retrieval of aerosol properties over the ocean using polarization as well as intensity of reflected sunlight, *J. Geophys. Res.*, 102(D14), 16,989–17,013. [1.1.3](#), [4.1](#)
- Mishchenko, M. I., and L. D. Travis (1998), Capabilities and limitations of a current fortran implementation of the t-matrix method for randomly oriented, rotationally symmetric scatterers, *Journal of Quantitative Spectroscopy and Radiative Transfer*, 60(3), 309–324. [2.2.2](#)
- Mishchenko, M. I., L. D. Travis, and D. W. Mackowski (1996), T-matrix computations of light scattering by nonspherical particles: A review, *Journal of Quantitative Spectroscopy and Radiative Transfer*, 55(5), 535–575. [2.2.2](#)
- Mishchenko, M. I., L. D. Travis, and A. A. Lacis (2002), *Scattering, Absorption, and Emission of Light by Small Particles*, Cambridge University Press, Cambridge, UK. [1.1.3](#), [2.1](#)
- Mishchenko, M. I., B. Cairns, J. E. Hansen, L. D. Travis, R. Burg, Y. J. Kaufman, J. Vanderlei Martins, and E. P. Shettle (2004), Monitoring of aerosol forcing of climate from space: analysis of measurement requirements, *Journal of Quantitative Spectroscopy and Radiative Transfer*, 88(1-3), 149–161. [1.1](#), [1.1.3](#), [4.3.2.1](#), [4.4](#), [4.3.2.3](#)
- Mishchenko, M. I., et al. (2007), Accurate monitoring of terrestrial aerosols and total solar irradiance: Introducing the glory mission, *Bulletin of the American Meteorological Society*, 88(5), 677–691. [1.1.3](#), [3.3.1](#)

- Myhre, G., et al. (2013), *Anthropogenic and Natural Radiative Forcing. In Climate Change 2013: The Physical Science Basis. Contribution of Working Group I to the Fifth Assessment Report of the Intergovernmental Panel on Climate Change [Stocker T.F., et al. (eds.)]*, book section 8, p. 659–740, Cambridge University Press, Cambridge, United Kingdom and New York, NY, USA. [1.1](#)
- Nadal, F., and F. M. Breon (1999), Parameterization of surface polarized reflectance derived from polder spaceborne measurements, *Geoscience and Remote Sensing, IEEE Transactions on*, 37(3), 1709–1718. [2.2.3](#)
- Nakajima, T., M. Tanaka, and T. Yamauchi (1983), Retrieval of the optical properties of aerosols from aureole and extinction data, *Applied Optics*, 22(19), 2951–2959. [1.1.1](#)
- Nakajima, T., G. Tonna, R. Rao, P. Boi, Y. Kaufman, and B. Holben (1996), Use of sky brightness measurements from ground for remote sensing of particulate polydispersions, *Applied Optics*, 35(15), 2672–2686. [1.1.1](#)
- Orphal, J., and K. Chance (2003), Ultraviolet and visible absorption cross-sections for hitran, *Journal of Quantitative Spectroscopy and Radiative Transfer*, 82(1-4), 491–504. [2.2.1](#)
- Patterson, E. M., D. A. Gillette, and B. H. Stockton (1977), Complex index of refraction between 300 and 700 nm for saharan aerosols, *Journal of Geophysical Research*, 82(21), 3153–3160. [4.2.1](#)
- Phillips, D. L. (1962), A technique for the numerical solution of certain integral equations of the first kind, *J. ACM*, 9(1), 84–97. [1.1.1](#), [3.3.2](#)
- Ramanathan, V., P. J. Crutzen, J. T. Kiehl, and D. Rosenfeld (2001), Aerosols, climate, and the hydrological cycle, *Science*, 294(5549), 2119–2124. [1.1](#)
- Reid, J. S., et al. (2008), An overview of uae2 flight operations: Observations of summertime atmospheric thermodynamic and aerosol profiles of the southern arabian gulf, *Journal of Geophysical Research: Atmospheres*, 113(D14), D14,213. [1.1.2](#), [4.1](#), [4.2.2](#)
- Remer, L. A., et al. (2005), The modis aerosol algorithm, products, and validation, *Journal of the Atmospheric Sciences*, 62(4), 947–973. [1.1.3](#)
- Ricchiazzi, P., S. Yang, C. Gautier, and D. Sowle (1998), Sbdart: A research and teaching software tool for plane-parallel radiative transfer in the earth's atmosphere, *Bulletin of the American Meteorological Society*, 79(10), 2101–2114. [\(document\)](#), [2.2](#), [2.3](#)

- Rodgers, C. D. (1998), Information content and optimisation of high spectral resolution remote measurements, *Advances in Space Research*, 21(3), 361–367. [3.2.2](#), [3.2.2](#)
- Rodgers, C. D. (2000), *Inverse Methods for Atmospheric Sounding: Theory and Practice*, World Scientific, Singapore. [3.2.1](#), [3.2.1](#), [3.2.2](#), [3.3.3](#)
- Rothman, L. S., et al. (2009), The hitran 2008 molecular spectroscopic database, *Journal of Quantitative Spectroscopy and Radiative Transfer*, 110(9-10), 533–572, doi: DOI: 10.1016/j.jqsrt.2009.02.013. [2.2.1](#)
- Sanghavi, S., J. V. Martonchik, J. Landgraf, and U. Platt (2012), Retrieval of aerosol optical depth and vertical distribution using o2 a- and b-band sciamachy observations over kanpur: a case study, *Atmos. Meas. Tech.*, 5(5), 1099–1119, aMTD. [3.2.2](#)
- Schuster, G. L., O. Dubovik, and B. N. Holben (2006), Angstrom exponent and bimodal aerosol size distributions, *J. Geophys. Res.*, 111, D07,207. [2.2.2](#), [3.3.1](#), [4.4](#), [5.2](#)
- Seinfeld, J. H., and S. N. Pandis (2006), *Atmospheric Chemistry and Physics: From Air Pollution to Climate Change, 2nd Edition*, 1232 pp., John Wiley and Sons, Inc., Hoboken, New Jersey. [2.2.2](#)
- Shannon, C. E. (1948), A mathematical theory of communication, *Bell System Technical Journal*, 27(3), 379–423. [3.2.2](#)
- Shaw, G. E. (1979), Inversion of optical scattering and spectral extinction measurements to recover aerosol size spectra, *Applied Optics*, 18(7), 988–993. [1.1.1](#)
- Smirnov, A., B. N. Holben, T. F. Eck, O. Dubovik, and I. Slutsker (2000), Cloud-screening and quality control algorithms for the aeronet database, *Remote Sensing of Environment*, 73(3), 337–349. [1.1.2](#)
- Spurr, R. (2006), Vlidort: A linearized pseudo-spherical vector discrete ordinate radiative transfer code for forward model and retrieval studies in multilayer multiple scattering media, *Journal of Quantitative Spectroscopy and Radiative Transfer*, 102, 316–342. [2.2.1](#), [2.2.4](#), [3.3](#)
- Spurr, R., and M. Christi (2014), On the generation of atmospheric property jacobians from the (v)lidort linearized radiative transfer models, *Journal of Quantitative Spectroscopy and Radiative Transfer*, 142(0), 109–115. [C](#)



- Spurr, R., J. Wang, J. Zeng, and M. I. Mishchenko (2012), Linearized t-matrix and mie scattering computations, *Journal of Quantitative Spectroscopy and Radiative Transfer*, 113(6), 425–439. [2.2.2](#), [3.3](#)
- Spurr, R. J. D. (2004), A new approach to the retrieval of surface properties from earthshine measurements, *Journal of Quantitative Spectroscopy and Radiative Transfer*, 83(1), 15–46. [2.2.3](#), [3.3](#)
- Tanaka, M., T. Nakajima, and T. Takamura (1982), Simultaneous determination of complex refractive index and size distribution of airborne and water-suspended particles from light scattering measurements, *Meteorological Society of Japan Journal*, 60, 1259–1272. [1.1.1](#)
- Tanaka, M., T. Takamura, and T. Nakajima (1983), Refractive index and size distribution of aerosols as estimated from light scattering measurements, *Journal of Climate and Applied Meteorology*, 22(7), 1253–1261. [1.1.1](#)
- Twomey, S. (1963), On the numerical solution of fredholm integral equations of the first kind by the inversion of the linear system produced by quadrature, *J. ACM*, 10(1), 97–101. [1.1.1](#), [3.3.2](#)
- Twomey, S. (1977), *Introduction to the Mathematics of Inversion in Remote Sensing and Indirect Measurements*, 243 pp., Dover Publications, Inc., Mineola, NY, USA. [3.3.2](#)
- Twomey, S., and H. B. Howell (1967), Some aspects of the optical estimation of microstructure in fog and cloud, *Applied Optics*, 6(12), 2125–2131. [1.1.1](#)
- van de Hulst, H. C. (1981), *Light Scattering by Small Particles (Dover edition)*, Dover Publications, Mineola, New York. [4.3.1](#), [4.3.1](#)
- Vermeulen, A., C. Devaux, and M. Herman (2000), Retrieval of the scattering and microphysical properties of aerosols from ground-based optical measurements including polarization. i. method, *Appl. Opt.*, 39(33), 6207–6220. [4.1](#)
- Vijay, N., and J. W. Hovenier (2012), Polarized light reflected and transmitted by thick rayleigh scattering atmospheres, *The Astrophysical Journal*, 748(1), 28. [2.3](#)
- Wagner, R., T. Ajtai, K. Kandler, K. Lieke, C. Linke, T. Müller, M. Schnaiter, and M. Vragel (2012), Complex refractive indices of saharan dust samples at visible and near uv wavelengths: a laboratory study, *Atmospheric Chemistry and Physics*, 12(5), 2491–2512. [4.2.1](#)



- Wang, J., and S. T. Martin (2007), Satellite characterization of urban aerosols: Importance of including hygroscopicity and mixing state in the retrieval algorithms, *Journal of Geophysical Research: Atmospheres*, 112(D17), D17,203. [5.4](#)
- Wang, J., X. Xu, R. Spurr, Y. Wang, and E. Drury (2010), Improved algorithm for modis satellite retrievals of aerosol optical thickness over land in dusty atmosphere: Implications for air quality monitoring in china, *Remote Sensing of Environment*, 114(11), 2575–2583, doi: DOI: 10.1016/j.rse.2010.05.034. [1.1.3](#), [3.3.2](#)
- Wang, J., X. Xu, D. K. Henze, J. Zeng, Q. Ji, S.-C. Tsay, and J. Huang (2012), Top-down estimate of dust emissions through integration of modis and misr aerosol retrievals with the geos-chem adjoint model, *Geophys. Res. Lett.*, 39(8), L08,802. [3.3](#)
- Wang, J., X. Xu, S. Ding, J. Zeng, R. Spurr, X. Liu, K. Chance, and M. Mishchenko (2014), A numerical testbed for remote sensing of aerosols, and its demonstration for evaluating retrieval synergy from a geostationary satellite constellation of geo-cape and goes-r, *Journal of Quantitative Spectroscopy and Radiative Transfer*, 146(0), 510–528. ([document](#)), [1](#), [2.2](#), [2.2](#), [2.3](#), [2.4](#), [2.5](#), [2.6](#)
- Wanner, W., X. Li, and A. H. Strahler (1995), On the derivation of kernels for kernel-driven models of bidirectional reflectance, *Journal of Geophysical Research: Atmospheres*, 100(D10), 21,077–21,089. [2.2.3](#), [2.2.3](#)
- Waquet, F., P. Goloub, J. L. Deuzé, J. F. Léon, F. Auriol, C. Verwaerde, J. Y. Balois, and P. François (2007), Aerosol retrieval over land using a multiband polarimeter and comparison with path radiance method, *Journal of Geophysical Research*, 112(D11). [2.2.3](#)
- Waquet, F., B. Cairns, K. Knobelspiesse, J. Chowdhary, L. D. Travis, B. Schmid, and M. I. Mishchenko (2009), Polarimetric remote sensing of aerosols over land, *J. Geophys. Res.*, 114(D1), D01,206. [1.1.3](#), [2.2.2](#), [3.3.1](#)
- Wendisch, M., and W. Von Hoyningen-Huene (1994), Possibility of refractive index determination of atmospheric aerosol particles by ground-based solar extinction and scattering measurements, *Atmospheric Environment*, 28(5), 785–792. [1.1.1](#)
- Xu, X., J. Wang, D. K. Henze, W. Qu, and M. Kopacz (2013), Constraints on aerosol sources using geos-chem adjoint and modis radiances, and evaluation with multisensor (omi, misr) data, *Journal of Geophysical Research: Atmospheres*, 118(12), 6396–6413. [3.3](#)

- Yamamoto, G., and M. Tanaka (1969), Determination of aerosol size distribution from spectral attenuation measurements, *Applied Optics*, 8(2), 447–453. [1.1.1](#)
- Yamasoe, M. A., Y. J. Kaufman, O. Dubovik, L. A. Remer, B. N. Holben, and P. Artaxo (1998), Retrieval of the real part of the refractive index of smoke particles from sun/sky measurements during scar-b, *Journal of Geophysical Research: Atmospheres*, 103(D24), 31,893–31,902. [1.1.1](#)
- Yang, Z., J. Wang, C. Ichoku, E. Hyer, and J. Zeng (2013), Mesoscale modeling and satellite observation of transport and mixing of smoke and dust particles over northern sub-saharan african region, *Journal of Geophysical Research: Atmospheres*, 118(21), 12,139–12,157. [1.1.3](#)
- Zeng, J., Q. Han, and J. Wang (2008), High-spectral resolution simulation of polarization of skylight: Sensitivity to aerosol vertical profile, *Geophys. Res. Lett.*, 35(20), L20,801. [4.1](#)
- Zhu, C., R. H. Byrd, P. Lu, and J. Nocedal (1994), L-bfgs-b: a limited memory fortran code for solving bound constrained optimization problems, *Technique report*, Northwestern University. [3.3.3](#)
- Ångström, A. (1929), On the atmospheric transmission of sun radiation and on dust in the air, *Geografiska Annaler*, 11, 156–166. [1.1.1](#)